The University of Groningen
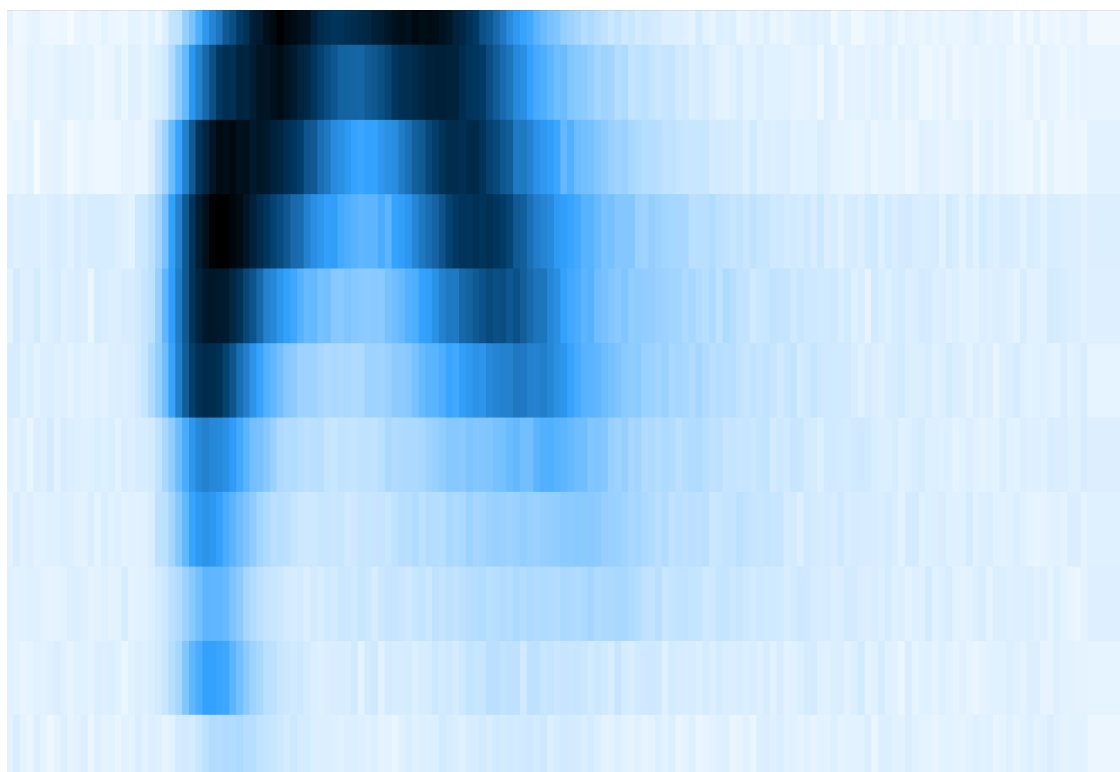
Slow molecular beams from a cryogenic buffer gas source

Author:
Rutger Hof

Supervisor:
Prof. Dr. Steven Hoekstra

November 19, 2019

university of groningen

faculty of science
and engineering

van swinderen institute for
particle physics and gravity

Abstract

The Standard Model (SM) of particle physics, while highly successful in most areas of fundamental physics, at this point in time fails to explain certain observed phenomena like the existence of dark matter and the matter-antimatter asymmetry. Extensions to the SM attempt to remedy these shortcomings, and these extensions predict different values for fundamental quantities like the electric dipole moment of the electron (eEDM). The NL-eEDM collaboration aims to measure the eEDM with a precision which improves on the most recent measurement of this quantity by an order of magnitude, setting more stringent limits on extensions to the SM in the process. The proposed experiment requires diatomic molecules (BaF), and in order to minimize the associated statistical uncertainty the (forward) velocity of these molecules should be minimized while at the same time maximizing the number of molecules which reach the interaction zone after a deceleration and laser cooling stage. This work describes the source built for this purpose, which is known as a cryogenic buffer gas source. The expected behavior of the molecular beam in the typical operating range of the relevant experimental parameters is discussed, as well as some technical details pertaining to the source and the different detection methods employed. Recommendations are made in order to match the (phase-space) output of the source to the acceptance of the decelerator. The number of molecules extracted from the source is determined and compared to the requirements of the planned eEDM experiment, and an estimate is given of the loss of molecules due to the distance between the source and the decelerator. The behavior of the forward velocity and translational temperature of the molecular beam and the amount of molecular signal are described qualitatively as a function of the main experimental parameters, which are: buffer gas flow rate, cell temperature, and ablation laser energy. Certain combinations of these parameters reveal a double peak structure in the time-of-flight (TOF) profiles, and the origin of this phenomenon is described. Finally, the interpretation of these TOF profiles is discussed in more detail, since the width of the molecular pulse significantly distorts their shape.

Contents

Chapter 1

Introduction

1.1 General overview

The Standard Model (SM) of particle physics has stood the test of time for several decades now. From the discovery of the top quark in 1995 [1, 2] and the tau neutrino in 2000 [3], to the more recent discovery of the Higgs boson in 2012 [4, 5], all the components predicted by this model have thus far been confirmed. At the Large Hadron Collider (LHC), more of these predictions continue to be tested, while also shedding more light on the workings of the by-now confirmed participants such as the Higgs boson. As the LHC shuts down for another round of maintenance and upgrades, proposals are taking shape to build even larger particle accelerators. The Future Circular Collider (FCC) [6, 7] is planned to have a circumference of about 100 km (compared to the LHC's 27 km) and run at a collision energy of 100 TeV (compared to the LHC's 14 TeV).

While it is arguably the most successful theory in particle physics to date, the SM is not without its flaws [8]. First, the theory does not include gravity, one of the four fundamental interactions of nature. Its mathematical framework is quantum field theory, and for decades attempts have been made to unite it with Einstein's general relativity, none of which have been successful or provided testable hypotheses so far. In addition, the existence of dark matter, the matter-antimatter asymmetry, neutrino masses, and neutrino oscillations are left unexplained in the SM.

Extensions to the SM like supersymmetry might provide solutions to these problems. Supersymmetry in particular predicts additional particles [9] at rather high energies (on the TeV scale), beyond what can currently be probed using for example the LHC. Upgrades to existing particle colliders and the proposed construction of new ones could allow us to discover those supersymmetric partners at the high energy frontier, should they exist.

There is another way in which these extensions can manifest themselves, namely in the field of low-energy precision measurements [10]. The predicted values of properties such as the muon anomalous magnetic moment [11] or the electron electric dipole moment [12] (electron EDM or eEDM, denoted by d_e) differ by orders of magnitude between the SM and its various extensions. The eEDM in particular is a possible source of CP violation [13], which in turn is related to the aforementioned problems with the SM (relating to the matter-antimatter asymmetry in particular). To be more exact, a nonzero eEDM would violate

time-reversal invariance, since it would suggest an aspherical charge distribution along the electron's spin axis. Following the CPT theorem [14, 15], T-violation would be equivalent to CP violation. The SM predicts an eEDM of $d_e \leq 10^{-38}$ e·cm [16], which is currently far out of reach for experiments, while within the framework of some extensions it can be $\mathcal{O}(10^{-28})$ e·cm [17], as illustrated in figure 1.1. Due to this sensitivity of the value of the eEDM to physics beyond the SM, its measurement is an attractive alternative (both complementary to and competitive with) to the high energy experiments that probe the same kind of physics. The most recent and stringent measurement of the eEDM was published in Nature in October 2018 [18]. The ACME collaboration (involving Harvard University and Yale University) found an upper limit of $|d_e| < 1.1 \times 10^{-29}$ e·cm.
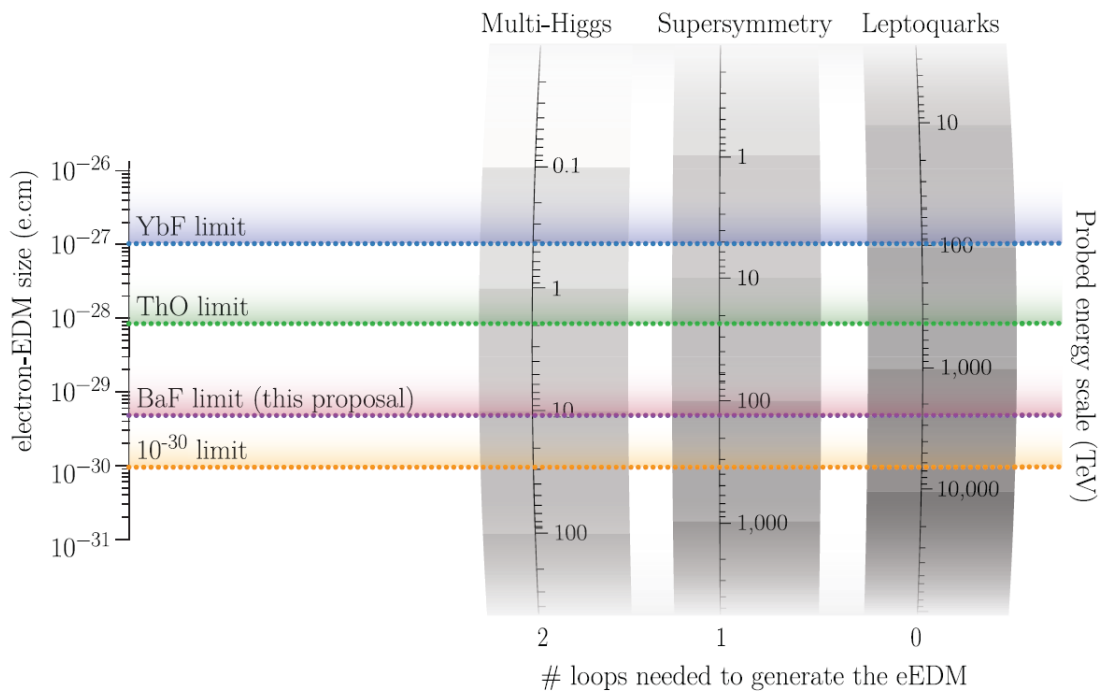
Figure 1.1: Overview of current and expected limits on the eEDM and how they relate to SM extensions. On the left, the eEDM constraint is depicted. On the right, the energy scale associated with a given limit is shown. Three extensions of the SM are shown in the figure, all with their own characteristic energy scale and the number of loops (a concept from quantum field theory) required to generate an eEDM of the magnitude shown on the left. Figure taken from [19].

The NL-eEDM collaboration (a collaboration between the University of Groningen, Vrije Universiteit Amsterdam, and Nikhef) aims to improve on the previous experiments and reach a sensitivity of 5×10^{-30} e·cm [19]. Part of the experimental setup that is currently being built is a cryogenic buffer gas source, which will provide the diatomic molecules used in the experiment.

This source will be the main topic of this thesis. Throughout this work, we will use terms like "the source", "cryogenic source", and "cryogenic buffer gas beam source" rather interchangeably. Unless explicitly stated otherwise, these terms all refer to the concept of the cryogenic buffer gas beam source. We will first discuss some of the components of the planned eEDM measurement in a fairly general sense, and then conclude this introduction with a status overview and an outline of this thesis, along with the main research questions which will be addressed. The interested reader is encouraged to dive into the relevant references if they wish to learn more about any particular part, but an in-depth understanding of them is not required for the rest of this thesis. Rather, this introductory chapter serves to set the scene and sketch the context within which the cryogenic buffer gas source will operate. Some familiarity with atomic and molecular physics is required. The appropriate background knowledge can be found for example in reference [20].

1.2   What does it take to measure an eEDM?

1.2.1   Principles of an eEDM measurement and molecule of choice

The general idea of measuring an eEDM [12] is to look at spin precession inside a very well-defined electric field. One can use diatomic molecules [21] (for example: BaF [19], YbF [22], or ThO [18]) as test subjects. These molecules can greatly enhance the effect of an eEDM [23], since their single valance electron is exposed to what is often called the effective electric field (E_{eff}), which in turn results in a (linear) Stark shift. This energy shift can be described by $U = -\vec{d_e} \cdot \vec{E}_{\text{eff}}$, where $\vec{d_e} = \frac{\hbar}{2}d_e\vec{S}$. Here $\vec{S}$ refers to the spin of the electron and d_e is the eEDM. The effective electric field, however, is not a property that can be measured directly, but instead relies on theoretical calculations using for example the relativistic coupled cluster approach. One can exploit the different Stark shifts associated with the hyperfine substates of the molecule of choice by putting it into a superposition of these substates. This will in turn result in an accumulated phase as the molecules travel through an applied external electric field. This phase can finally be measured by comparing the laser-induced fluorescence (LIF) signal from the molecules for parallel and anti-parallel orientations of the applied electric (and magnetic) fields. The observed phase difference ϕ is directly related to the value of the eEDM by [19]:

$$\phi = d_e|P|E_{\text{eff}}\frac{\tau}{\hbar} \tag{1.1}$$

Where τ is the (coherent) interaction time spent by the molecule in the interaction zone (the region where an external electric field is applied), and P is the polarizability of the molecule. This expression of the phase in turn translates into the statistical uncertainty that can be achieved with this type of eEDM measurement [19]:

$$\sigma_d = \frac{\hbar}{e}\frac{1}{2|P|E_{\text{eff}}\tau\sqrt{\dot{N}T}} \tag{1.2}$$

Where the new variables are $\dot{N}$, the rate of detected molecules (dN/dt) and T, the total measurement time. For the NL-eEDM experiment, this statistical uncertainty is estimated to be 5×10^{-28} e·cm, based on a measurement of 24 hours at a repetition rate of 10 Hz and the detection of 7×10^5 molecules per shot. To understand where these estimates come from and get a more complete picture of the final experiment, we will now briefly go over its various components. A schematic overview of the complete setup is depicted in figure 1.2.
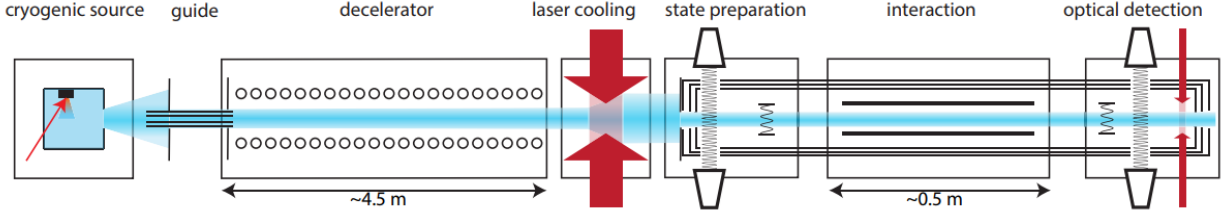
Figure 1.2: Schematic overview of the proposed experiment. A molecular beam is created by a cryogenic source and subsequently slowed down by a traveling wave Stark decelerator. Laser cooling is then employed to reduce the transverse velocity of the beam. The actual eEDM measurement takes place in a 0.5 m long interaction zone where the molecules interact with very well-defined electric and magnetic fields. Finally, the accumulated phase shift due to the eEDM is observed using Ramsey interferometry. Figure taken from [19].

1.2.2 Cryogenic source

A measurement cycle begins with the production of a beam of BaF molecules in a cryogenic buffer gas source. In a cold (10-20 K) cell, a target is ablated. Depending on the target and the predominant ablation products, SF_6 gas flows through as well, which then reacts with these products to form the molecular species of interest. The target is generally a precursor of this species of interest (for example a compressed and scintered pill of 90% SrF_2, and 10% B for stability [24] in order to create SrF molecules). Meanwhile, a buffer gas (typically helium, neon, or some other inert gas) is continuously lead through the cell at a much higher density and flow rate. This flow rate (given in SCCM: Standard Cubic Centimeters per Minute) can be tuned and, generally speaking, higher flow rates will result in a higher forward velocity as the beam exits the cell. This effect of flow rates on the molecular beam will be discussed in more detail in the relevant sections of this thesis. The operating principle of a cryogenic buffer gas source is that the molecules of interest (BaF for the proposed eEDM experiment) will transfer some of their momentum to the buffer gas molecules as they collide and propagate towards the exit. As a result, a molecular beam originating from a cryogenic source will have a much lower transverse velocity ($\sim$180 m/s) than for example a source based on supersonic expansion [25] ($\sim$300 m/s and above), which was the method previously employed by the VSI (Van Swinderen Institute of the University of Groningen) group to produce the molecules used in their Stark decelerator [26]. This difference is depicted in figure 1.3, along with the fact that a buffer gas source will produce a much wider velocity distribution. The lower initial velocity of the molecular beam is desirable for the eEDM experiment, since it would increase the time τ spent by the molecules in the interaction zone, and the statistical uncertainty scales linearly with τ.

The goal is to create a molecular beam where the amount of molecules which can be accepted by the decelerator, the next component in the experimental sequence, is maximal, while also keeping the forward velocity as low as possible due to its effect on the statistical uncertainty. The source is estimated to produce around 10^{13} molecules per pulse inside the cell, which, assuming an efficiency of extracting the molecules from the cold cell of 5×10^{-3}, results in 5×10^{10} molecules per pulse. In order to match the phase-space distribution of the beam to the acceptance of the decelerator, an electrostatic guide will connect the two
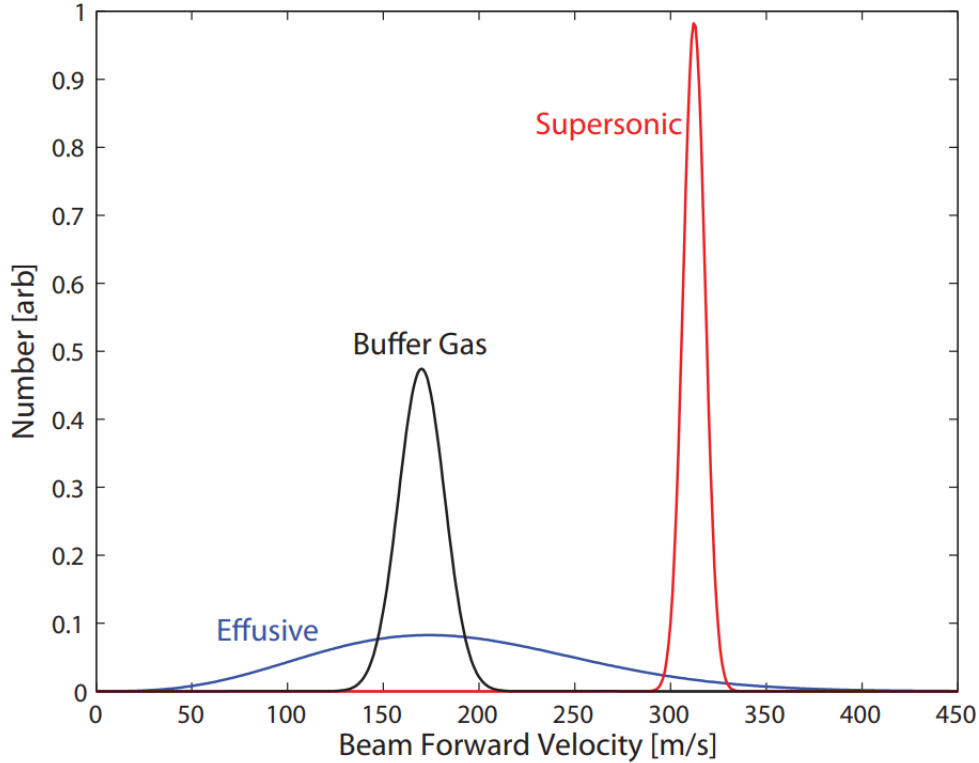
Figure 1.3: The different velocity distributions resulting from various production methods, most importantly the supersonic and buffer gas methods. Figure taken from [27].

components. The resulting beam is estimated to have a forward velocity of 180±50 m/s and a transverse velocity spread of ±30 m/s.

1.2.3   Stark Decelerator

After producing a molecular beam with a forward velocity of about 180 m/s, a Stark decelerator will reduce this forward velocity to about 30 m/s. As the name suggests, the decelerator utilizes the Stark effect; the electric dipole moment of the (diatomic) molecules will interact with an applied electric field. This interaction can be described by adding a term to the Hamiltonian of the system of the form [20]:

$$H_s = -\vec{\mu} \cdot \vec{E} \tag{1.3}$$

Where $\vec{\mu}$ is the electric dipole moment of the molecule and $\vec{E}$ the applied electric field. This perturbation results in a shift W of this molecule's energy levels, which will depend on the strength of the field. Placing a molecule with an electric dipole moment (like the diatomic molecules SrF and BaF) in an inhomogeneous electric field will thus result in a force $\vec{F} = -\nabla W$. It is precisely this force that decelerates the molecular beam from 180 m/s down to 30 m/s. The decelerator consists of a set of rings with a diameter of 4 mm. These electrodes are mounted on eight rods that are 0.5 m in length. The rods are placed

in an alternating octagonal pattern, such that every ninth subsequent electrode is attached to the same rod. By applying a sinusoidal voltage to these rods, every subsequent one 45 degrees out of phase with its neighbor, comoving potential wells propagate along the length of the decelerator, taking the molecules with them. By reducing the frequency of the applied voltage, the velocity of these comoving wells is reduced and the molecules are decelerated. The Stark decelerator at the VSI is 4.5 m long (nine of these modules) and has been used in the past to slow down SrF molecules. The apparatus has shown great promise by reducing the initial kinetic energy of a supersonic SrF beam by 85% [28]. More detailed descriptions of the decelerator and its characterization over the past years can be found in references [26] and [29].

The number of molecules that the decelerator can actually decelerate depends on both the spatial distribution and the velocity distribution of the incoming beam. The spatial acceptance is limited by the finite size of the electrodes, which have a diameter of 4 mm. As a result, only the molecules within ± 2 mm from the center of the electrodes will be accepted.

The accepted velocities depend on the applied voltage and the resulting depth of the moving potentials, as well as the Stark shift of the molecules in any particular state. These states need to be carefully chosen to be appropriate for the next segment: laser cooling. All things considered, when the molecular beam reaches the decelerator only the molecules within ± 2 mm from the center of the electrodes that have a transverse velocity up to ± 5 m/s [19] with respect to this center can actually be slowed down by the apparatus. Meanwhile, their forward velocity must also be within ± 8.5 m/s [19] from the set velocity of the applied electric potential. Based on the estimated output of the cryogenic source and the decelerator's acceptance, a fraction of 4×10^{-4} can be decelerated, resulting in a beam containing 2×10^6 molecules per pulse exiting the decelerator [19].

1.2.4 Laser cooling

The molecular beam exiting the Stark decelerator is estimated to have a transverse velocity spread of ± 5 m/s and a forward velocity of 30 ± 6 m/s. As this beam travels through the 0.5 m long interaction zone it diverges. In order to minimize losses due to this divergence, laser cooling will be used to reduce the transverse velocity component of the molecules even further.

The techniques of laser cooling have only recently been adapted from the realm of atoms to that of molecules [30]. Their more complex structure leads to the leaking of molecules into dark states where they can no longer be cooled. The possibility of laser cooling BaF has been investigated using relativistic coupled cluster calculations [23], a very powerful quantum (computational) chemistry technique. These calculations show fairly diagonal Franck-Condon factors, minimizing losses to dark states. Additionally, the main cooling and repumping transition wavelengths (order of 800 nm) associated with the lowest vibrational levels in the ground state ($X^2\Sigma_{1/2}$) and first excited state ($A^2\Pi_{1/2}$) are easily accessible using diode lasers and in the optical part of the spectrum, which is convenient when building an experimental setup.

At the end of the laser cooling section the molecules are transferred to the EDM measurement state, a superposition of the $m_F = 1$ and $m_F = -1$ hyperfine sublevels of the $F = 1$ state. The efficiency of the cooling is estimated to be 0.8 and the efficiency of the state
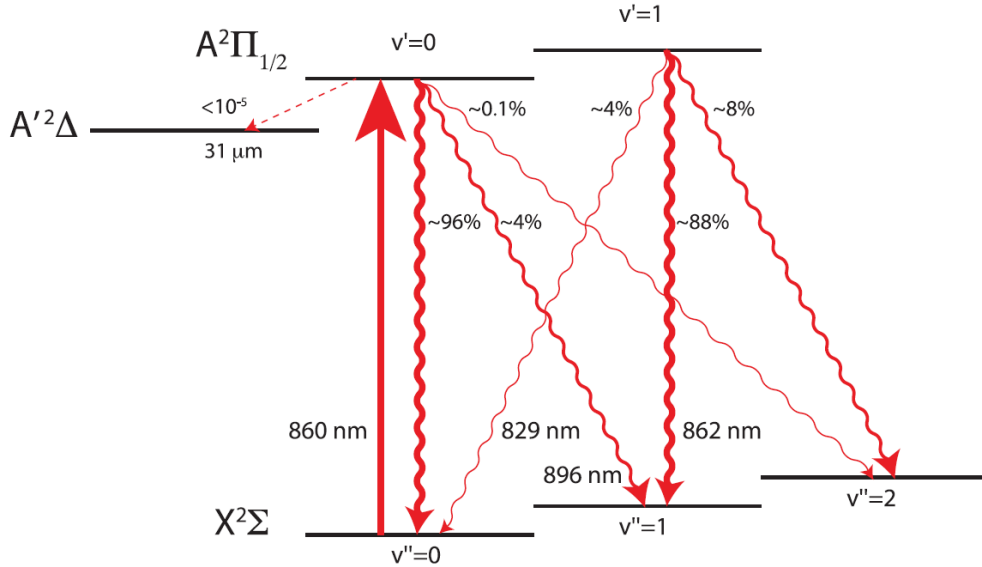
Figure 1.4: The relevant energy levels of BaF for the eEDM experiment. Due to the highly diagonal Franck-Condon factors associated with these transitions only two repump lasers (to repump molecules from $v" = 1$ and $v" = 2$) will be required. Figure taken from [19].

preparation is estimated to be 0.7, resulting in 9×10^5 molecules per shot with a reduced transverse velocity of ± 0.2 m/s [19].

1.2.5 Interaction zone

Finally, the molecular beam will enter the interaction zone, where the aforementioned phase accumulates. This zone is 0.5 m long and magnetically shielded in order to control the magnetic field inside down to the fT level. Using μ-metal [31] the fields can be suppressed down to 50 pT. Probes both in- and outside the interaction zone will monitor the field strength and a feedback system will correct for sub-second changes in the magnetic field.

Inside the interaction zone, an electric field of order 10 kV/cm is generated using special coated glass plates. This coating allows the plates to operate in a vacuum with high voltages, all while being transparent. As part of checking for systematic effects, the electric field is regularly reversed on a timescale much larger than the coherence time.

At the end of the interaction zone, the superposition state is collapsed back onto the first excited rotational level and detected using fluorescence. Every molecule is estimated to scatter about 10^3 photons, which are then collected using a lens system with an expected efficiency of 1% and imaged onto a (cooled) EMCCD camera which has a quantum efficiency of 50% at the detection wavelength of 860 nm [19]. The net effect of this chain is that, on average, 5 photons will be detected per molecule, leading to a detection efficiency close to unity. Taking into account a transmission and state transfer efficiency of 0.8, the total number of detected molecules per shot is estimated to be 7×10^5 [19].

1.3 Status overview and thesis outline

The many parts required for the eventual eEDM measurement are currently being designed (laser cooling and interaction zone), built (interaction zone), tested (cryogenic source), and optimized (decelerator and cryogenic source). Connections between the different components are being planned out while the elaborate data acquisition system which is necessary for the first tests of the completed setup is slowly taking shape. The NL-eEDM collaboration is actually building two cryogenic sources, one of which has been in operation in Groningen since September of 2018, while the other is still under construction in Amsterdam. While the operational source is being characterized and coupled to the Stark decelerator, the Amsterdam team will implement improvements on the existing design. In the end, the original source at the VSI will be replaced with the Amsterdam source. For clarity: the Groningen source is the subject of this thesis, and the molecular beam it currently produces consists of SrF molecules. For further information about eEDM measurements or any of the individual components, the reader is encouraged to consult the references.

Next, we will go over the necessary theory behind buffer gas cooling and the measurements required to characterize a molecular beam. After discussing the cryogenic source which was built and tested at the VSI in Groningen we will move on to the characterization of this beam. In the end, we will relate the measured properties to the demands set by the proposed eEDM measurement. Any room for improvement in both design and optimization found along the way will be mentioned, since the source in Amsterdam can then accommodate for this. Recommendations will be made in terms of further characterization of the source and other interesting avenues which could be explored in future research efforts concerning cryogenic buffer gas sources.

The central questions which this thesis aims to answer either quantitatively or qualitatively are:

- What can the theory behind buffer gas cooling say about the molecular beam emerging from the source, given the range of experimental parameters at our disposal and the demands of the NL-eEDM project?

- How can the losses from coupling the source to the decelerator be minimized?

- How many molecules does the source produce per shot, and how significant is the divergence of the beam by the time it reaches the decelerator?

- What is the effect of experimental parameters like the cell temperature, buffer gas flow rate, and ablation laser energy on the forward velocity and translational temperature of the molecular beam?

- Can the emergence of a double peak structure under certain experimental conditions be understood and perhaps even exploited?

- How should one interpret the time-of-flight (TOF) profiles from a cryogenic source when the arrival times are comparable to the width (in arrival time) of the molecular pulse?

Chapter 2

Theory

2.1 Principles behind buffer gas cooling

Within the greater context of an electron EDM measurement, the goal of the source, whatever form it may take, should be clear from the previous chapter. In order to minimize the statistical uncertainty (see equation 1.2), the source should provide as many molecules as possible (and minimize losses along the way), while minimizing the initial forward velocity, resulting in longer interaction times as the beam travels through the interaction zone.

A cryogenic buffer gas beam source can address these needs. These types of sources have a rather low forward velocity output compared to other methods of production, like the previously used and well-established method of supersonic expansion [32]. In addition, the beams produced in this way tend to have a considerably higher brightness [33].

In this theory section, we will briefly explore the working principles of the buffer gas source, which are summarized in figure 2.1. Most of the topics discussed here are also described in more detail in reference [27], which is an excellent review of the topic at hand that the reader is encouraged to examine in more detail if the explanations given in this work are insufficient in any way.

The molecular species of interest is produced in a cell, typically with dimensions of a few centimeters. This cell is often subject to high vacuum (9.8×10^{-9} mbar in our source) and at temperatures below 30 K down to about 10 K, depending on the melting point of the buffer gas used. Inside the cell, a target containing some precursor of the species of interest is ablated in order to produce the desired molecules, which are either direct ablation products or formed by reactions between the ablation products and an extra gas which is lead into the cell. Meanwhile, the inert buffer gas continuously flows through the cell at such a rate that the number density inside the cell is low enough to prevent the formation of clusters but still high enough in order to provide enough collisions for the species of interest to be cooled. The molecules, along with the buffer gas, then exit the cell into a high vacuum region, typically through a few-millimeter sized hole, resulting in a molecular beam. The exact shape of the exit has some influence on the outgoing beam, which is a topic we will briefly touch on later.

The species of interest dissipates a significant part of its initial energy through elastic collisions with the cold buffer gas molecules. Because this mechanism is purely mechanical in nature, and thus independent of the oftentimes complex internal energy structure of

molecules, it can be applied to basically any molecular species.
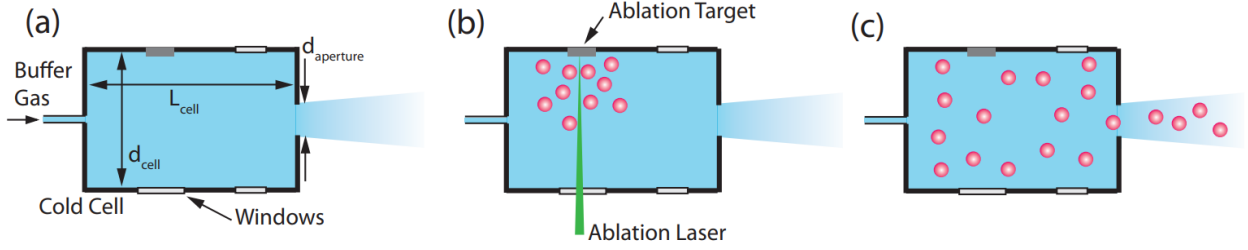
Figure 2.1: Schematic overview of the production of a molecular beam inside a cryogenic buffer gas source. (a) The cold buffer gas enters the cell with length L_{cell} and diameter d_{cell}, exiting the cell through an aperture of diameter $d_{aperture}$. The shaded region indicates the buffer gas density, which is high inside the cell and decreases as the gas exits the cell. (b) Laser ablation of a precursor target leads to the production of the species of interest. (c) The species thermalizes to the buffer gas. A molecular beam is formed and exits the cell through the aperture, along with the buffer gas. Figure adapted from [27].

2.1.1 Flow regimes

Inside the cell, gas flow determines the general behavior of the molecular beam. For this reason, we will briefly review some basic concepts concerning gas flow, like the different flow regimes and the Reynolds number, which is a quantity used to characterize gas flow.

The Reynolds number is simply the ratio of inertial to viscous forces, which can be expressed as [27]:

$$Re = \frac{F_{\text{inertial}}}{F_{\text{viscous}}} = \frac{\rho w^2 d^2}{\mu w d} = \frac{\rho w d}{\mu} \tag{2.1}$$

Where ρ is the density, w the flow velocity, d the characteristic length (in the case of the cell this is $d_{aperture}$), and μ the viscosity.

This quantity can be related to other quantities, like the Mach number $Ma = w/c$ and Knudsen number $Kn = \lambda/d$ through [27]:

$$Ma \approx \frac{1}{2}KnRe \tag{2.2}$$

Where λ is the mean free path and c the speed of sound in the gas given by [27]:

$$c = \sqrt{\frac{\gamma k_B T}{m}} \tag{2.3}$$

Given that the gas has atomic mass m and specific heat γ. The mean free path in turn is given by [27]:

$$\lambda = \frac{1}{\sqrt{2}n\sigma} \tag{2.4}$$

Where n is the number density and σ the atomic cross section for elastic collisions. Typical values for these parameters will be derived and stated in the next section.

At the cell exit, the gas molecules will travel at the mean thermal velocity [27]:

$$\bar{v} = \sqrt{\frac{8k_B T}{\pi m}} \tag{2.5}$$

The source described in this thesis uses neon as its buffer gas, and operates at temperatures ranging from 14 to 28 K, which translates into mean thermal velocities ranging from 121 m/s to 171 m/s. Since for a monatomic gas (the buffer gas generally used in a cryogenic source) $\gamma = \frac{5}{3}$, one finds that $\bar{v} \approx c_{monatomic}$, and as a result of equation 2.2 we find that $KnRe \approx 2$. This leads to an expression for the Reynolds number:

$$Re \approx 2Kn^{-1} = \frac{2d_{\mathrm{aperture}}}{\lambda} \tag{2.6}$$

There are three distinct flow regimes that can be characterized by their Reynolds numbers [27]:

- $Re < 1$: Effusive regime. There are almost no collisions near the exit of the cell. The resulting beam is simply a sampling of the thermal distribution inside the cell, largely unchanged. Since buffer gas sources are generally employed to cool down the initial molecular beam, the effusive regime is not immediately relevant to this topic, and by extension this thesis.

- $1 < Re < 100$: Intermediate or partially hydrodynamic regime. The typical operating regime for a buffer gas beam source. A significant amount of collisions take place and the properties of the initial beam are changed in a substantial way.

- $Re > 100$: Supersonic or fully hydrodynamic regime. Due to a large number of collisions, the buffer gas behaves more and more fluid-like for higher Reynolds numbers. In this regime, the beam will look similar to those formed using supersonic expansion. In this case, one cannot apply simple gas kinetics to describe the beam, but must resort to the more complicated dynamics of incompressible fluids.

2.1.2 Flow through the cell, thermalization, diffusion, and extraction

We now move on to a general description of the physical parameters involved in buffer gas cooled molecular beams. The resulting expressions won't be exact, and there will be differences depending on the exact cell geometry, temperature of the cell, and ablation process, among other things. This section is meant to serve as a tool in developing an intuitive understanding of the working principles, and the descriptions will in general be functional within an order of unity.

The cell is kept at a temperature T_b, and has characteristic length L_{cell} and diameter d_{cell} of order a few centimeters, resulting in a volume of $V_{\mathrm{cell}} \approx L_{\mathrm{cell}} d^2_{\mathrm{cell}}$. The buffer gas of mass m_b is lead into the cell and leaves the cell through an aperture of diameter d_{aperture}, typically a few millimeters in size. Using a mass flow controller, the buffer gas flow rate $f_{0,b}$ can be set. These flow rates are typically measured in SCCM, standard cubic centimeter per

minute, which translates into roughly 4.5×10^{17} buffer gas atoms per second. In our setup, the flow rates range from 1 to 40 SCCM. The number density, at steady state, is then given by [27]:

$$n_{0,b} = \frac{4 f_{0,b}}{A_{\text{aperture}} \bar{v}_{0,b}} \tag{2.7}$$

Where A_{aperture} is the aperture area and $\bar{v}_{0,b}$ the mean thermal velocity of the buffer gas inside the cell as given by equation 2.5. In our source, $d_{\text{aperture}} = 4.5$ mm, the flow rates range from 1 SCCM to 40 SCCM, and the mean thermal velocity ranges from 121 m/s to 171 m/s. As a result, the number density will be roughly in the range of $1.7 \cdot 10^{15}$ cm^{-3} to $9.3 \cdot 10^{16}$ cm^{-3} From equations 2.4, 2.6, and 2.7 a relation between the flow rate and the Reynolds number is then established:

$$Re \approx \frac{2 d_{\text{aperture}}}{\lambda} = 2\sqrt{2} d_{\text{aperture}} \sigma n_{0,b} = \frac{8\sqrt{2} d_{\text{aperture}} \sigma f_{0,b}}{A_{\text{aperture}} \bar{v}_{0,b}} \tag{2.8}$$

This expression can be used to relate the different flow regimes and their typical behavior to the molecular beams formed using certain flow rates. The collision cross section σ tends to be $\approx 10^{-14}$ cm^2 [27, 34]. This leads to Reynolds numbers ranging roughly from 8 to 475.

Ideally, the species of interest has cooled down to the cell temperature by the time it reaches the aperture. The number of collisions needed for this to be the case can be estimated if we assume the buffer gas atoms to be hard spheres. The loss in kinetic energy per collision can then be expressed in terms of the temperature before and after the collision [27]:

$$\Delta T = -(T - T_b)\kappa^{-1} \tag{2.9}$$

Where $\kappa = \frac{(m_b + m_s)^2}{2 m_b m_s}$, referring to the masses of the buffer gas (b) and the species of interest (s). After N collisions, the temperature of the species is then:

$$T(N) = T(N-1) - (T - T_b)\kappa^{-1} \tag{2.10}$$

This can in turn be treated as a differential equation if we assume N to be large compared to a ΔT which is rather small:

$$\frac{dT(N)}{dN} = -\left(T(N) - T_b\right)\kappa^{-1} \tag{2.11}$$

From which one can extract the following expression relating the temperature ratios to the number of collisions:

$$\frac{T(N)}{T_b} = 1 + \left(\frac{T(0)}{T_b} - 1\right) e^{-N\kappa^{-1}} \approx 1 + \frac{T(0)}{T_b} e^{-N\kappa^{-1}} \tag{2.12}$$

This relation between the number of collisions and the temperature of the species is shown in figure 2.2, while figure 2.3 shows this relation on a logarithmic scale . Using relevant values, like $m_s = m_{SrF} = 87.62 + 18.9984$ amu and $m_b = m_{ne} = 20.1797$ amu [20] and temperatures of $T_b = 16$ and $T(0) \approx 10^4$ K [35] the species of interest asymptotically approaches the buffer gas temperature (within one percent) after about 42 collisions. In fact,

15
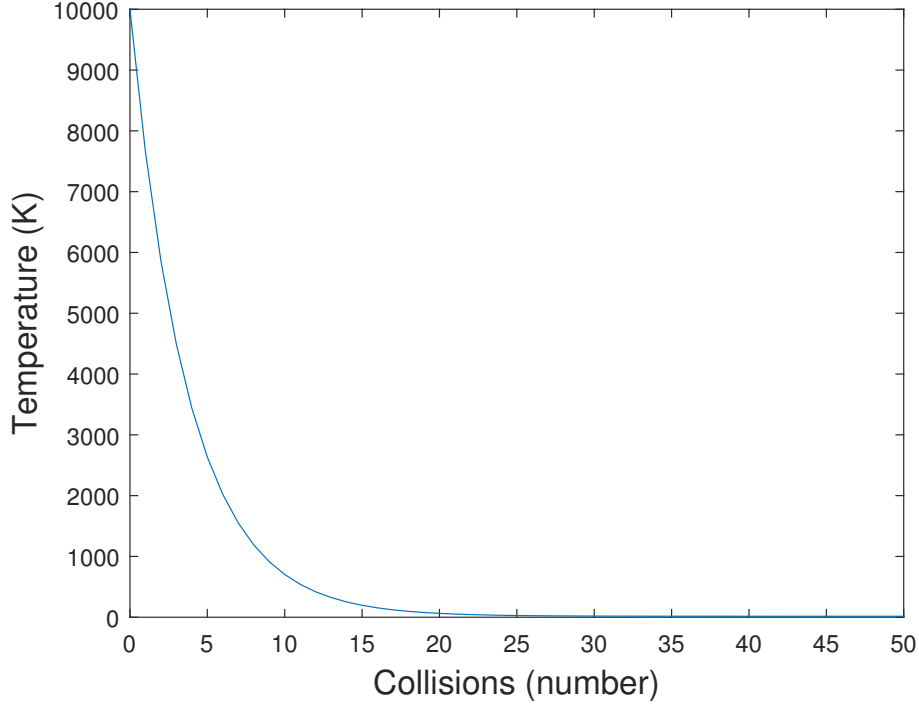
Figure 2.2: The effect of collisions on the temperature of the species of interest. The buffer gas is neon and $T_b = 16$ K, while the initial temperature of the species of interest is taken to be $T(0) = 10000$ K. After about 42 collisions the species temperature approaches the buffer gas temperature.

given a buffer gas temperature T_b and an initial species temperature $T(0)$, from equation 2.12 it follows that the species temperature will be within a fraction α of the buffer gas temperature after N_{thermal} collisions:

$$N_{\text{thermal}} = \kappa \ln \left(\frac{T(0) - T_b}{\alpha T_b} \right) \tag{2.13}$$

The species of interest has its own mean free path inside the cell, given by [27]:

$$\lambda_s = \frac{(n_{0,b}\sigma_{b-s})^{-1}}{\sqrt{1 + m_s/m_b}} \approx \frac{A_{\text{aperture}}\bar{v}_{0,b}}{4 f_{0,b}\sigma_{b-s}\sqrt{m_s/m_b}} \tag{2.14}$$

Where the number density $n_{0,b}$ comes from equation 2.7 and σ_{b-s} is the cross section for collisions between buffer gas atoms and species molecules, which tends to be of order 10^{-14} cm^2 [27,34]. The resulting mean free path expected for our source ranges from 0.043 mm to 2.4 mm. Combining the estimated mean free path and the number of collisions required for thermalization, the typical thermalization length is:

$$L_{\text{thermal}} = N_{\text{thermal}} \times \lambda_s = \kappa \ln \left(\frac{T(0) - T_b}{\alpha T_b} \right) \frac{A_{\text{aperture}}\bar{v}_{0,b}}{4 f_{0,b}\sigma_{b-s}\sqrt{1 + m_s/m_b}} \tag{2.15}$$

16
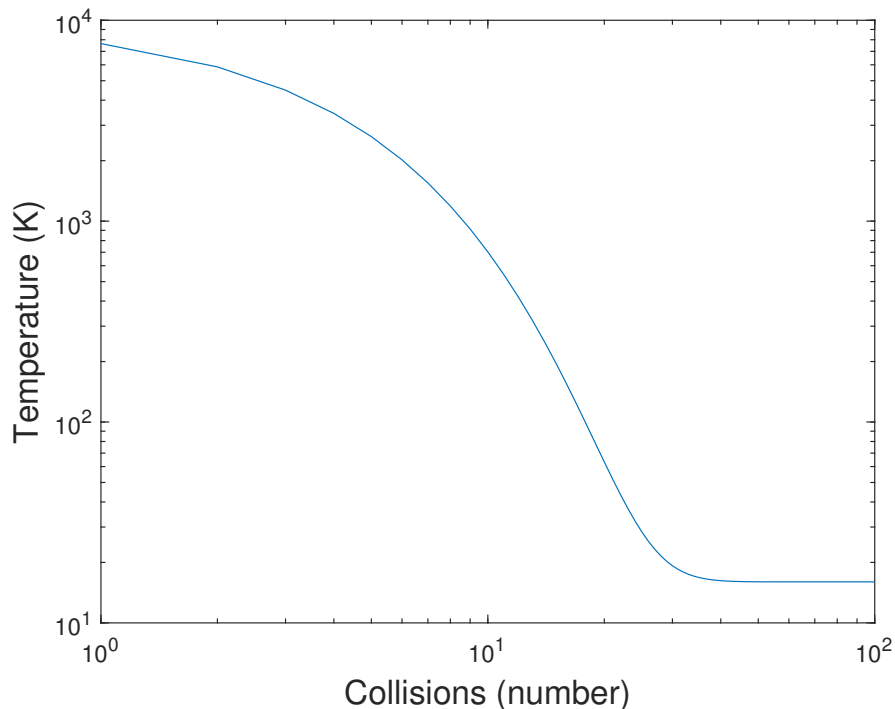
Figure 2.3: The effect of collisions on the temperature of the species of interest, on a logarithmic scale. The buffer gas is neon and $T_b = 16$ K, while the initial temperature of the species of interest is taken to be $T(0) = 10000$ K. After about 42 collisions the difference between the temperature of the species and the buffer gas is less than 1% of T_b.

Which is typically about 1 cm [27], but as equation 2.15 shows, it is highly dependent on the specifics of the experiment in question. While some of those parameters, such as the mass of the buffer gas and target species and their collision cross section, are more or less set in stone, the other parameters can be altered somewhat. Clearly, the size of the aperture is of some influence (larger diameter means longer thermalization length), as well as the buffer gas flow rate (a higher flow rate results in a shorter thermalization length). We also have control over the buffer gas temperature, and by extension also the mean thermal velocity, within a certain well-defined range. The least well-known parameter in equation 2.15 is the initial temperature of the species of interest, $T(0)$. This is hard to pin down in a robust way, since one cannot simply probe the temperature of the ablation products after ablation. Since the amount of space inside the cell is rather limited and the necessary thermal shielding blocks any clear visual path towards the ablation spot, this can also not be investigated using for example a camera. While the exact relation is unclear, this temperature should obviously depend on the ablation laser power, spot size, and the duration of the ablation laser pulse. A higher ablation power should result in a higher temperature of the ablation products, which in turn increases the thermalization length. Once this thermalization length exceeds the distance from the ablation spot to the cell exit, there will not be enough collisions in order for the species of interest to properly thermalize to the buffer gas. We will revisit this when we discuss the results of the characterization measurements.

In order to extract the species of interest from the cell, one has to prevent the species from diffusing to the walls of the cell, since there it will simply freeze and the molecules are effectively lost. The diffusion constant, which characterizes this process, can in the case of the species diffusing into the buffer gas be described by [27]:

$$D = \frac{3}{16(n_{0,s} + n_{0,b})\sigma_{b-s}}\sqrt{\frac{2\pi k_B T_0}{\mu}} \approx \frac{3}{16 n_{o,b}\sigma_{b-s}}\sqrt{\frac{2\pi k_B T_0}{\mu}} = \frac{3\pi \bar{v}_{0,b}}{32 n_{0,b}\sigma_{b-s}} \quad (2.16)$$

Where in the approximation we assume $n_{0,b} \gg n_{0,s}$ and $m_s \gg m_b$, μ is the reduced mass $m_s m_b/(m_s + m_b)$, and $\bar{v}_{0,b}$ comes from equation 2.5. The diffusion time τ_{diff} will be used to describe this process, and here we define it as the time where the mean squared displacement is equal to A_{cell}. This mean squared displacement at a time t is [27]:

$$\langle \Delta x^2 \rangle(t) = 6Dt = \frac{9\pi \bar{v}_{0,b}}{16 n_{0,b}\sigma_{b-s}}t = A_{\text{cell}} \quad (2.17)$$

The resulting diffusion time is:

$$\tau_{\text{diff}} = \frac{16 A_{\text{cell}} n_{0,b}\sigma_{b-s}}{9\pi \bar{v}_{0,b}} \quad (2.18)$$

Which, using typical values for our source, should be between 0.04 and 3 ms.

This diffusion time is only relevant if we can find a similar timescale during which the species of interest flows out of the cell to create a beam. This timescale is the extraction or "pumpout" time. The buffer gas exits the cell at a rate given by [27]:

$$\dot{N}_b = \frac{1}{4V_{\text{cell}}} N_b \bar{v}_{0,b} A_{\text{aperture}} \quad (2.19)$$

Where N_b is the total number of buffer gas atoms inside the cell and $\dot{N}_b$ the rate at which they flow out of it. The solution to this differential equation is an exponential function, with a characteristic timescale of:

$$\tau_{\text{pump}} = \frac{4V_{\text{cell}}}{A_{\text{aperture}} \bar{v}_{0,b}} \quad (2.20)$$

Which in our source should be between 0.5 and 0.8 ms.

We can now combine the diffusion and pumpout time into a dimensionless quantity:

$$\gamma_{\text{cell}} = \frac{\tau_{\text{diff}}}{\tau_{\text{pump}}} \approx \frac{4\sigma_{b-s} n_{0,b} A_{\text{aperture}}}{9\pi L_{\text{cell}}} \approx \frac{\sigma_{b-s} f_{0,b}}{L_{\text{cell}} \bar{v}_{0,b}} \quad (2.21)$$

Where in the approximation we drop the numerical prefactor (of order unity) since this is simply an estimate, not meant to be exact or universal, and used equation 2.7. Using typical values for our source, this should be between 0.08 and 5.

In the case where $\gamma_{\text{cell}} \ll 1$, diffusion of the species of interest to the walls takes place at a significantly shorter timescale compared to extraction, and most of the molecules will be lost since they will freeze on the cell walls. The output molecular flux in this case will be rather low, along with the extraction efficiency (the fraction of molecules created in the cell that

make it out). This efficiency can be increased by using a higher buffer gas flow rate. The exact relation between γ_{cell} and the extraction efficiency is not completely understood but experiments have shown it to be approximately linear, exponential, or even cubic depending on the species [27].

When $\gamma_{\text{cell}} \gg 1$ the effect is called "hydrodynamic enhancement" or "hydrodynamic entrainment". Since most molecules are extracted from the cell before they diffuse to the wall, the result is a beam of increased brightness and a high output flux. The velocity distribution of the beam will also differ considerably from what was present inside the cell compared to the $\gamma_{\text{cell}} \ll 1$ case.

One should keep in mind however that, while equation 2.21 is very instructive in estimating extraction efficiency, it is only an approximation. From the expression, no explicit dependence on aperture diameter is present, while the extraction efficiency has been shown to depend on this parameter [36], where increasing the aperture size showed an increase in efficiency until the efficiency saturated at a certain aperture size.

2.2 Properties of the emerging beam

Now that we have developed an understanding of the processes occurring inside a buffer gas source, we will briefly discuss how they govern the properties of the emerging molecular beam. The focus will be on both the transverse and longitudinal velocities and their spreads, as well as the angular spread. These are the most relevant properties for our purpose of focusing as many molecules as possible within a low forward velocity range and minimizing losses due to the divergence of the beam.

2.2.1 Forward velocity

In the previous section we have introduced the different flow regimes and their associated Reynolds numbers. The buffer gas flow will largely dictate the forward velocity of the molecular beam exiting the cell, so this velocity will be related to the Reynolds number. Generally, there will be three regimes in which this behavior will differ: the effusive, intermediate, and supersonic regime.

In the effusive regime, there will essentially be no collisions near the cell exit. From the velocity distribution inside the cell, a mean forward velocity can be extracted [27]:

$$\bar{v}_{\parallel\text{eff}} = \frac{3\pi}{8}\bar{v}_{0,s} \approx 1.2\bar{v}_{0,s} \tag{2.22}$$

For when $Re < 1$. The subscript s denotes the species of interest. This expression is clearly not dependent on the Reynolds number itself, and so gives us a lower limit on the forward velocity one can achieve using a buffer gas source.

In the supersonic regime, many collisions occur near the cell exit and as a result the molecular beam will be boosted in the forward direction somewhat. Assuming that we have a rather small number of molecules (of the species of interest) compared to the number of buffer gas atoms, enough collisions will take place as the species travels towards the aperture that it will be in (near) thermal equilibrium with the buffer gas. As a result, the properties
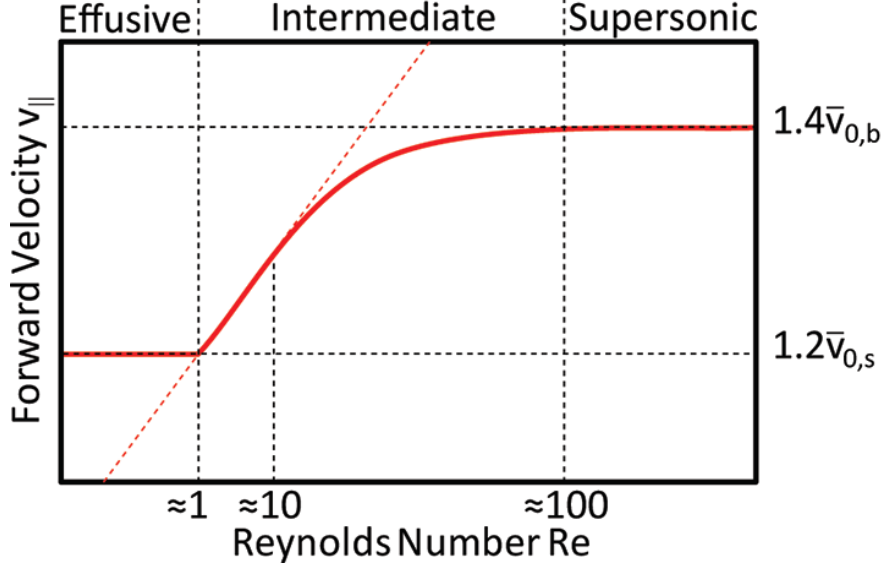
Figure 2.4: Dependence of the forward velocity of the molecular beam on the Reynolds number. In our source, velocities are expected to range from 63 m/s ($1.2\bar{v}_{0,s}$ for a species temperature of 14 K) to 240 m/s ($1.4\bar{v}_{0,b}$ for a buffer gas temperature of 28 K). See the full text for the reasoning in each flow regime. Figure from [27].

of both species will be rather similar, and for the sake of approximation we will assume them to be the same in the following analysis. In the supersonic regime, the molecules will be boosted in the forward direction due to the large number of collisions near the cell exit, leading to [27]:

$$v_{\parallel ss} = \sqrt{\frac{5\pi}{8}}\bar{v}_{0,b} \approx 1.4\bar{v}_{0,b} \tag{2.23}$$

For when $Re > 100$. This serves as an upper limit on the forward velocity of the molecular beam, which is directly related to the temperature of the buffer gas.

In the intermediate regime, the forward velocity depends on the Reynolds number. The heavy species of interest collides with the buffer gas species, which has a much lower average velocity, also resulting in a boost in the forward direction, albeit less drastic compared to the supersonic regime. Near the cell exit, the species of interest takes part in about $Re/2$ collisions [27], and every collision results in a momentum boost in the forward direction of $m_b v_b$, so the total boost is about $\frac{v_b m_b}{2m_s}Re$. In the lower Reynolds number region, for about $1 < Re < 10$, the buffer gas forward velocity can be approximated as the mean forward velocity of an effusive beam, so $v_b \approx 1.2\bar{v}_{0,b}$. Combining these assumptions, we find that:

$$v_{\parallel \text{intermediate1}} =\approx 1.2\bar{v}_{0,s} + 0.6\bar{v}_{0,b}Re\frac{m_b}{m_s} \tag{2.24}$$

In the $1 < Re < 10$ regime, which is linear in Re. Thus one would expect the forward velocity of the beam to increase linearly with the buffer gas flow rate in this regime.

From the discussion concerning the forward velocity in the supersonic regime, we expect this velocity to saturate towards $1.4\bar{v}_{0,b}$ as the Reynolds number increases. In connecting the linear regime to this saturation plateau, one can use the "sudden freeze" model [36]. The

20

idea is to consider the species of interest to be in thermal equilibrium with the buffer gas until they reach a certain point along the beam where there are no more collisions due to a dramatic decrease in buffer gas density, such that the properties of the beam are no longer altered by these collisions. The resulting forward velocity of the beam as a function of the Reynolds number is [27]:

$$v_{\|\text{intermediate2}} = 1.4\bar{v}_{0,b}\sqrt{1 - 4Re^{-4/5}} \tag{2.25}$$

In the $10 < Re < 100$ regime. The transition starts around $Re \approx 10$, which is based on an experiment where Hutzler et al [27] investigated at which flow rates collisions occur at distances larger than the diameter of the cell exit.

The combined dependence on Reynolds number in the different regimes is illustrated in figure 2.4. The velocity of the beam can vary between $1.2\bar{v}_{0,s}$ and $1.4\bar{v}_{0,b}$, first increasing linearly with the Reynolds number until it eventually saturates towards $1.4\bar{v}_{0,b}$. As mentioned in the previous sections, the source is typically operated at a temperature ranging from 14 to 28 K. Assuming proper thermalization of the species of interest, the mean thermal velocities are given by equation 2.5, and the resulting molecular beam should have a velocity ranging from 63 m/s ($1.2\bar{v}_{0,s}$ for a species temperature of 14 K) to 240 m/s ($1.4\bar{v}_{0,b}$ for a buffer gas temperature of 28 K).

2.2.2   Spread in velocity and angle

When discussing the velocity spread, we will be talking about the full width at half maximum (FWHM) of the velocity distribution of the molecular beam. In the effusive regime, this distribution will be thermal in nature, namely a Maxwell-Boltzmann distribution. The corresponding FWHM for this distribution is [27]:

$$\Delta v_{\|} = \sqrt{\frac{8\ln 2 k_b T_0}{m_s}} = \sqrt{\pi \ln 2}\bar{v}_{0,s} \approx 1.5\bar{v}_{0,s} \tag{2.26}$$

This takes on values between 79 ms and 112 m/s, corresponding to a thermalized species at 14 and 28 K respectively. This spread is directly related to the temperature of the beam and thus tied to the quality of the thermalization process inside the cell and the previous discussion on thermalization length. The same line of reasoning applies to the transverse velocity spread, so:

$$\Delta v_{\perp} \approx 1.5\bar{v}_{0,s} \tag{2.27}$$

Similar to the previous discussion on the forward velocity, the transverse velocity spread takes on a slightly different form for low Reynolds numbers in the intermediate regime [27]:

$$\Delta v_{\perp} \approx 1.5\bar{v}_{0,s} + \frac{Re}{2}\frac{m_b}{m_s}\frac{d_{\text{cell}}^2}{d_{\text{aperture}}^2}\bar{v}_{0,b} \tag{2.28}$$

While this describes the velocity spread as the beam exits the cell, it is far more instructive to consider these spreads away from the aperture, most importantly at a distance from the cell where the source meets the decelerator in the planned eEDM experiment. This situation is rather complex though since one has to deal with both the dynamics leading to the spreads

we have just arrived on, as well as the dynamics of the expansion of the molecular beam as it exits the cell and enters the high vacuum area around it. It has been shown [36] that in this case, the transverse velocity spread first increases linearly and then saturates around $Re \approx 100$. The behavior in fact seems quite similar to the relation seen in figure 2.4, but the transitions from one type of behavior to the next do not necessarily coincide.
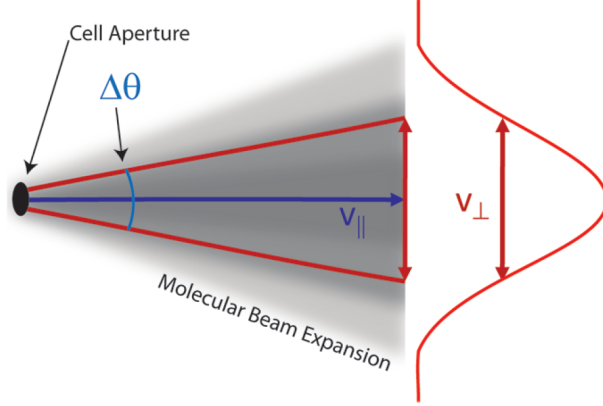
Figure 2.5: Figure from [27] depicting the relation between the angular spread and the velocity spreads of a molecular beam.

The angular velocity spread follows from geometric considerations in combination with the forward velocity and transverse velocity spread. As figure 2.5 illustrates, this angular spread is:

$$\Delta \theta = 2 \arctan \left(\frac{\Delta v_\perp / 2}{v_\parallel} \right) \tag{2.29}$$

For an effusive beam, the number density originating from an (infinitesimal) aperture area can be described by [27]:

$$n(R, \theta) = \frac{n_0 \cos(\theta)}{4 \pi R^2} dA \tag{2.30}$$

The angular spread (FWHM) $\Delta \theta$ can be found by solving $n(R, \theta/2) = \frac{1}{2} n(R, 0)$, giving:

$$\Delta \theta = \frac{2\pi}{3} \approx 120° \tag{2.31}$$

As described in the previous section, the forward velocity will increase linearly with the Reynolds number in the $1 < Re < 10$ range, while the transverse spread will essentially stay constant by equation 2.27. The result from equation 2.29 is that as the Reynolds number increases, the divergence of the beam will decrease. This decrease continues until the species of interest will have a forward velocity equal to the buffer gas forward velocity $\bar{v}_{0,b}$. Assuming that $m_s > m_b$ and using equation 2.5 the angular spread then approaches:

$$\Delta \theta \approx 2 \sqrt{\frac{m_b}{m_s}} \tag{2.32}$$

Combining these regimes, $\Delta\theta$ should, for increasing Reynolds numbers, roughly decrease linearly from about 120° in the effusive regime to about $2\sqrt{\frac{m_b}{m_s}}$ as one approaches the supersonic regime. In our source, where neon is the buffer gas and SrF the species of interest, this divergence approaches 50° for increasing Reynolds numbers.

2.3 Phase-space matching

As we have seen, there are many parameters relating to the source that can affect the properties of the molecular beam. These parameters will determine for example the velocity profile and temperature of the outgoing beam, and as a result one has at least some control over these properties. It is however not beyond the realm of possibility that even by tweaking those parameters there is still a significant loss of molecules from their production to the moment they enter the decelerator. There are some options to extend these capabilities though. This process of mapping the emittance of one experimental element to the acceptance of the next is sometimes referred to as phase-space matching. In general, a given phase-space distribution will evolve over time similar to figure 2.6. A distribution centered around a certain spatial coordinate will start to rotate and spread out. Only the molecules which are within the acceptance parameters of the decelerator can effectively be decelerated. It should be clear from figure 2.6 that, as the molecular beam travels from the source towards the decelerator, the distribution of molecules will thin out, and the number of molecules within this acceptance will decrease at time goes on. However, figure 2.6 only shows the phase-space of one spatial dimension, while there are of course three. Due to the symmetry of the decelerator though, the two transverse directions relative to the longitudinal direction (through the decelerator) are rather similar, and in the following general discussion on phase-space matching it is sufficient to separate the manner into the longitudinal and transverse phase-space and their respective acceptances.

The transverse velocity spread in particular leads to a significant amount of losses. To understand this, consider the spatial acceptance ($\pm\,2\,\mathrm{mm}$) of the decelerator in the transverse direction, given by the diameter (4 mm) of its electrodes. The distance between the source and the decelerator, as currently designed, is 360 mm. Similar to figure 2.5, this means that only those molecules with a transverse velocity equal to a fraction 2/360=1/180 of the mean forward velocity will actually make it within the rings of the decelerator. Assuming a rough estimate of 180 m/s for the forward velocity, this means that only the molecules with a transverse velocity of $\pm\,1\,\mathrm{m/s}$ can be decelerated. This is purely due to the distance between the source and the decelerator. The decelerator itself however has a transverse acceptance of 3 m/s [19] due to the applied voltages and the molecular structure of BaF. The result is an underfilling of the transverse acceptance of the decelerator, since the molecules with a transverse velocity larger than 1 m/s but smaller than 3 m/s will simply not be within the aforementioned $\pm\,2\,\mathrm{mm}$ by the time the beam reaches the decelerator. If, instead of 360 mm, the distance between the source and the decelerator could be 120 mm, these two acceptances would match and losses would be minimized. This distance can not be decreased indefinitely, for various reasons. Most obviously, mechanical reasons, meaning that there has to be enough space to bolt the two parts together in a way which does not break easily. Secondly, a valve needs to be installed in between the two components, since it would allow
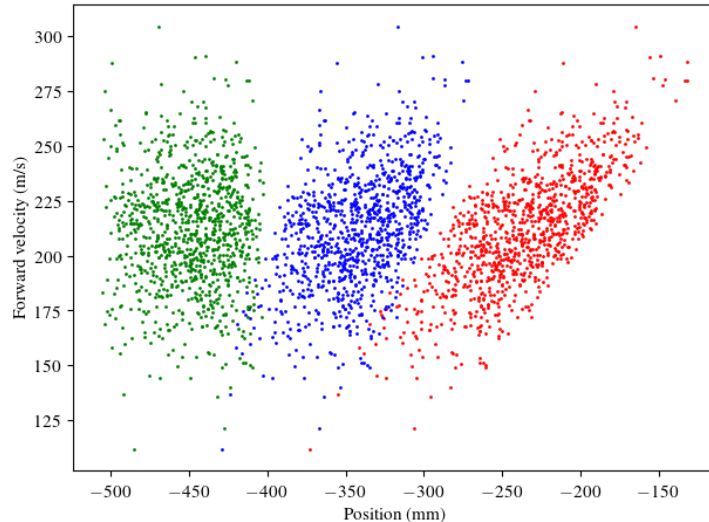
Figure 2.6: Simulated phase-space evolution of 1000 molecules with a center velocity of 210 m/s at three times in the longitudinal (forward) direction. The three colored distributions represent the distribution of the molecules at $t = 0$, $t = 0.5$ ms, and $t = 1$ ms respectively. Position is relative to the start of the decelerator, and the distribution at t=0 is similar to the expected output of a cryogenic source. Figure from [37].

us to separate the two high-vacuum areas if any maintenance is required on either side. The current design, where this distance is 360 mm, is the shortest possible connection given the desire for a valve. It should be clear from the preceding discussion that any method of phase-space matching should ideally not increase this distance, or otherwise compensate for a longer distance by focusing the molecules within the acceptance of the decelerator. We will briefly discuss a few ways to achieve this, and how relevant they are to our setup.

2.3.1 Electrostatic guide

The proposal mentions the use of electrostatic lenses [38] to concentrate more molecules into the acceptance area of the decelerator. This option is currently being investigated and designed. This guide will inevitably increase the distance between the source and the decelerator, which was designed to be as small as possible in order to prevent losses due to the divergence of the beam over this distance. The design will have to balance the effect of an increased distance with the increased number of molecules that will end up within the acceptance of the decelerator as a result of the guide. Figure 2.7 shows the simulated trajectory for a molecular beam of ND_3 which is focused by such a guide. The principles are described in more detail in reference [38]. We will return to this topic in the outlook section, since the design is still a work in progress.

24
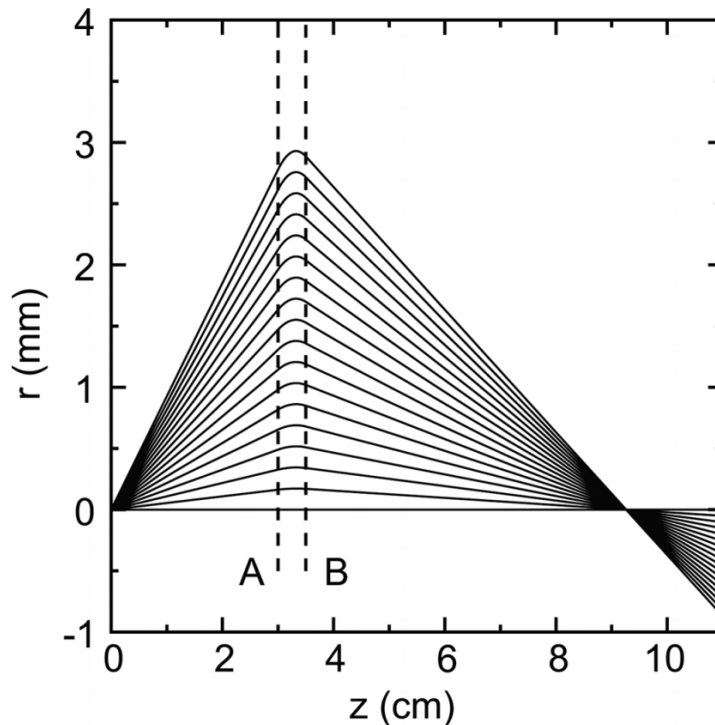
Figure 2.7: Simulated trajectories of selected ND$_3$ molecules if a voltage difference of 10 kV is applied between the adjacent rods that make up a guide. The guide is switched on at point A and off at point B, which results in ideal focusing into a single point. Figure taken from [38].

2.3.2   De Laval nozzle

The final option we will discuss is the use of special cell exits, or nozzles. The exact shape of the cell exit has proven to have some influence over the molecular flux and extraction efficiency of the cell. Moreover, while buffer gas cooling generally results in rather low axial velocity spreads, the transverse spread tends to be rather large. By shaping the cell exit accordingly, one might be able to reduce the transverse velocity spread even more, which would also result in a smaller angular spread at some distance from the cell and improved molecular flux, provided that the extraction efficiency remains the same.

A converging-diverging nozzle, also known as a de Laval nozzle, has recently shown great promise in this area. De Laval nozzles are mainly used in aerospace engineering since they can accelerate hot, highly pressurized gas towards the supersonic regime [39]. The gas is cooled down in the process, as heat energy is converted into kinetic energy. Careful design of the nozzle can ensure that the velocity streamlines remain parallel to the nozzle axis. This would result in a rather uniform flow after the nozzle in terms of velocity, temperature, and density. These properties will remain well-defined for several centimeters or even decimeters after the nozzle. In the world of experimental research, the use of de Laval nozzles is rather limited. The CRESU experiment in France for instance uses them to investigate chemical reactions at low temperatures. [40]. Nozzles have been designed for specific gasses (helium

and neon) and temperatures, as well as mixtures of the gasses [41]. The combination of
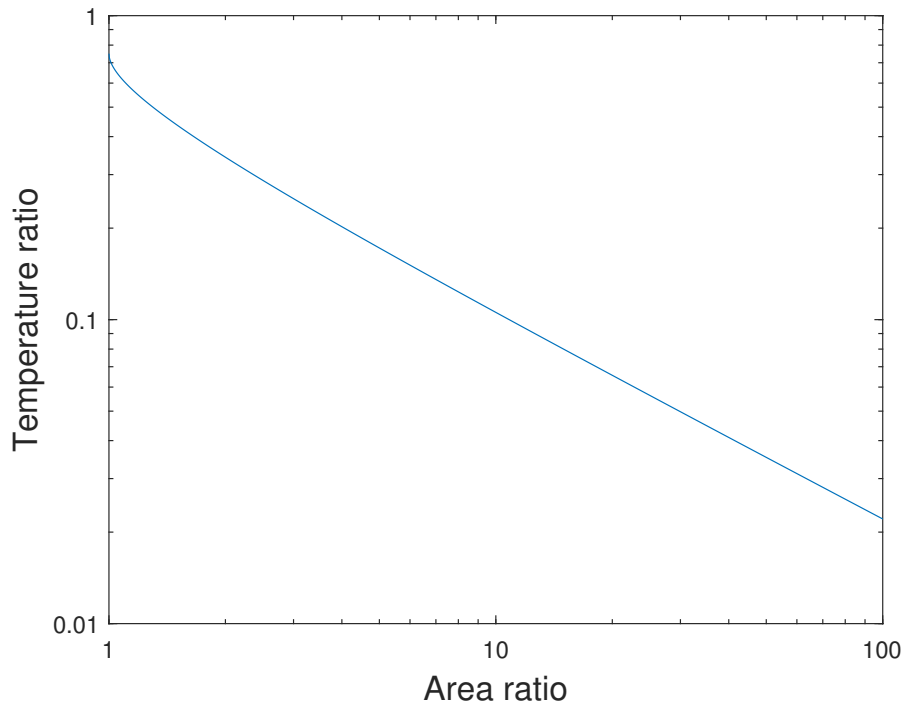
Figure 2.8: The cooling effect of a de Laval nozzle (on a logarithmic scale), assuming a perfect monatomic gas. The temperature ratio refers to that of the incoming versus outgoing molecular beam. The area ratio is that of the throat (most narrow part) versus the nozzle exit. The relation follows from reference [39].

a cryogenic buffer gas source with a de Laval nozzle at the exit has only recently been investigated [42]. Using beams of titanium and ytterbium atoms, a decrease in transverse temperature (factor 3) has been observed using these nozzles while the longitudinal velocities remained relatively unaffected. This effect was especially more pronounced at higher flow rates (over 50 SCCM). The idealized effect of a de Laval nozzle is depicted in figure 2.8. It shows the cooling (temperature ratio) as a function of the ratio of the nozzle's exit to throat (the most narrow part of the nozzle) area.

While the option to add a de Laval nozzle to our cryogenic source has been considered, its effects have not yet been tested in our setup. Discussions within our group have lead to the conclusion that, at least for now, it would be too time-consuming to pursue this option while the expected gains are minimal. This followed from an argument involving Louiville's theorem, similar to what is presented in reference [38]. The result is that, while such a nozzle can change the shape of the six-dimensional volume in phase space which is occupied by the molecules, the volume itself cannot change. A reduction in the transverse velocity spread would then result in either an increase in the axial velocity spread or the angular (spatial) spread. Since the acceptance of the Stark decelerator is finite and well-defined, the total number of molecules within this acceptance is not likely to be increased in a significant way by employing a de Laval nozzle.

Chapter 3

Setup

In this chapter we will describe the cryogenic source built at the VSI in Groningen, which is the subject of this thesis. We will discuss the various components which make up the apparatus in a broad sense, while more detail can be found in reference [43]. The design is similar to what is described in references [27] and [32]. In addition, we will discuss the detection methods and the laser infrastructure required for these detection methods in some detail, as well as the currently employed laser stabilization system. Once the apparatus is sufficiently understood, we will move on to the characterization of the source in chapter 4.

3.1 The source

The source is depicted schematically in figure 3.1, along with its most important components. It consists of a cell (shaped like a cylinder with a radius of 5 mm and a length of 17 mm), which is mounted to the cold stage of a two-stage closed-cycle cryocooler (Sumitomo Heavy Industries RP-082B2S). The temperature of these two stages can be set, and generally the "warm stage" will be at 40 K while the cold stage will be at 4 K. The temperature of the cell is controlled using heating elements (denoted "Heater", green in figure 3.1) and monitored using temperature diodes (red in figure 3.1) which are placed on the different stages. The entire setup is enclosed in a vacuum chamber, which keeps the pressure at around 9.8×10^{-9} mbar. Since the source is kept at such low temperatures and pressures, it takes about a full workday to open the source up and cool it back down again if for example the target has to be replaced or repairs have to take place.

The molecular beam created in the source is detected in two ways. First, about 5 mm after the cell exit, an absorption laser beam crosses the molecular beam. This probe beam is then focused onto a photodiode, and when SrF molecules absorb photons from the probe beam this absorption signal can be seen in the form of a dip in the photodiode voltage over time. This signal is recorded for analysis, and will be used in chapter 4 when we characterize the source. It should be noted that the photodiode used in the absorption measurements has been changed during the course of this research project. Initially, fluctuations in the power of the probe laser resulted in a rather weak absorption signal. The photodiode was later replaced by a differential photodiode (Thorlabs PDB210A/M) in order to take these fluctuations into account. When we discuss the absorption signal in chapter 4, we are looking

27
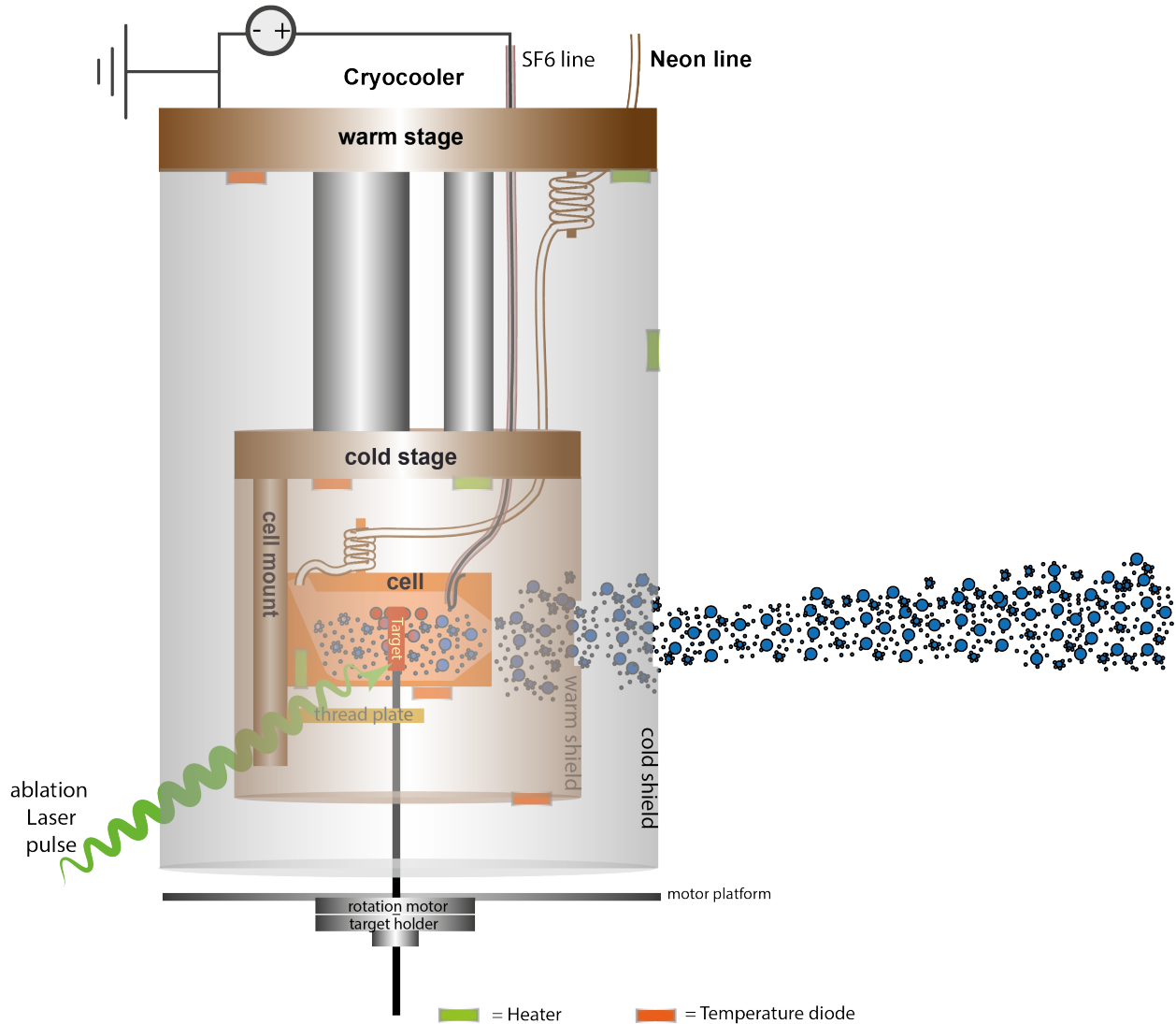
Figure 3.1: Schematic overview of the cryogenic source. The cryocooler and several heating elements (denoted "Heater" in green) allow us to control the temperatures of the different stages, which are monitored using temperature diodes. Gas lines are present to allow neon and SF_6 gas to flow into the cell. A step motor rotates the target so that the ablation laser pulse hits a fresh spot every time. Adapted from [43].

at absorption signals as measured by this differential photodiode. The laser power of the absorption probe was generally in the order of 0.3 mW, with a diameter of 4 mm.

The second detection method is that of laser-induced fluorescence (LIF), which takes place about 30 cm from the cell exit. Laser light which is tuned to the $A^2\Pi_{1/2}$ ($v' = 0$, $J = 1/2$) $\leftarrow X^2\Sigma^+$ ($v = 0$, $N = 1$) transition of SrF at a wavelength of 663 nm [29] is absorbed by the molecules and subsequently re-emitted in all directions. By collecting the emitted photons and counting them using a photomultiplier tube (PMT) over time we can see when the SrF molecules reach the LIF probe beam. When we discus the LIF signal in chapter 3, these counts over time are accumulated over many shots (typically minutes at a

repetition rate of 10 Hz). The emitted photons are collected by a set of mirrors and lenses and focused onto the PMT (Hamamatsu H7422P-40) after they pass a narrow bandpass (20 nm) filter, which is centered around 661 nm to get rid of as much background as possible that does not originate from the 663 nm photons. Typically, the LIF probe beam has a power of about 1.7 mW and a diameter of 4 mm.

Both the absorption and LIF detection use the same laser light, which originates from an extended cavity diode laser (ECDL). This home-built ECDL is stabilized to a wavelength of 663 nm using what is known as a transfer cavity lock. In the following sections we will describe this laser system and this stabilization method in some detail before demonstrating its performance.

3.2 The laser system

The laser system used to produce the detection laser light and stabilize its frequency has been in use for multiple years now. Though some details have changed and the general infrastructure has been improved in the meantime, the working principles remain the same. More detailed descriptions of these systems can be found in references [26], [44], and [45]. Before we move on to the characterization of the source, we will briefly go over the laser system and its most relevant features. Then we will go over the locking procedure, which stabilizes the detection laser to a helium-neon (HeNe) laser. The laser system is schematically depicted in figure 3.2.
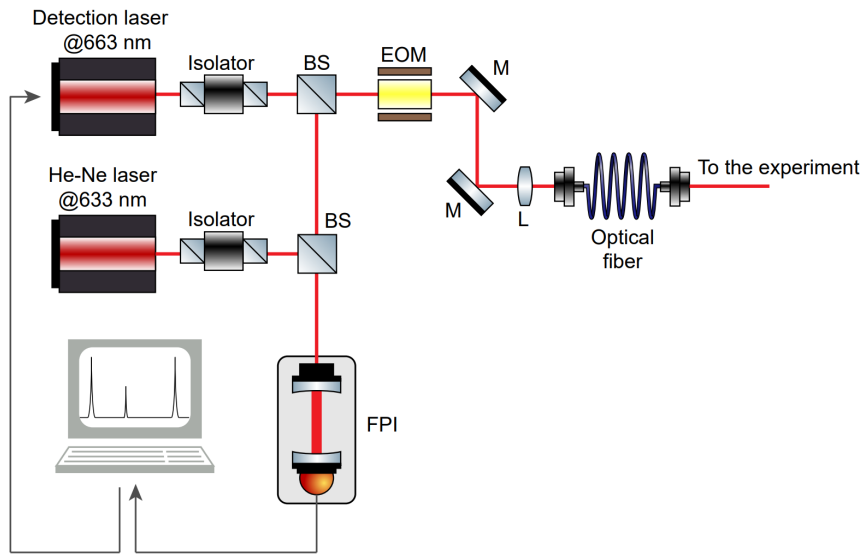
Figure 3.2: Schematic overview of the laser system. Both the detection (663 nm) laser beam and a stabilized HeNe (633 nm) laser beam are lead into a Fabry-Perot cavity (PFI in the figure). Isolators directly in front of the laser beam sources prevent reflections from destabilizing the sources due to optical feedback. The detection laser beam also passes through an electro-optical modulator (EOM) which broadens its frequency in order to address the hyperfine components of the ground state of SrF. Figure taken from [29].

In brief, both the laser beam from the ECDL (detection laser at a wavelength of 663 nm) and an already stable HeNe laser (633 nm) are lead into a Fabry-Perot cavity (FPI in figure 3.2), which is used to stabilize the detection laser using a transfer cavity lock. This locking procedure will be discussed in more detail shortly. Isolators directly in front of the laser beam sources prevent reflections from destabilizing the sources due to optical feedback. The detection laser beam also passes through an electro-optical modulator (EOM) which broadens its frequency in order to address the hyperfine components of the ground state of SrF. Most relevant for the characterization of the source is the stabilization of the laser light, since the detection methods used rely on the fact that the light is tuned to a specific transition in the SrF molecule at 663 nm. It is therefore of the utmost importance that during any measurement the detection laser is locked to this transition wavelength, which is why we will now discuss the concept of a transfer cavity lock in some detail.

3.3   Laser stabilization

The wavelength of the ECDL is stabilized using what is known as a transfer cavity. Such a system essentially transfers the stability of one laser (a stabilized HeNe laser) to a less stable one. This principle has been used to detect SrF molecules after deceleration since the construction of the decelerator [26, 29].

Figure 3.3: The locking program while it is in operation. The top graph shows the signal from the cavity; the two highest peaks correspond to the HeNe laser, while the two smaller peaks correspond to the ECDL. The graph on the lower half of the screen shows the relative position of one of the ECDL peaks over time. The program creates feedback voltages in such a way as to keep this position at the set position, which in this example is 0.24.

To achieve this, laser light originating from both the ECDL and the already stable reference laser (HRS015B from Thorlabs with a stability of ±2 MHz/hour) is coupled into a Fabry-Perot cavity (SA200-5B from Thorlabs). In essence, such a cavity consists of two mirrors placed some distance d apart. By shining light into the cavity, it is confined inside, bouncing back and forth between the mirrors. If one imposes the boundary condition that the transverse components of the electric field vanish at the surface of these mirrors, the result is a standing wave inside this cavity. Since only an integer number of half-wavelengths can fit between the two mirrors, the frequencies of this standing wave are limited to discrete values [45]:

$$f_q = q\frac{c_n}{2d} \tag{3.1}$$

Where c_n is the speed of light in the medium, and q is an integer often referred to as mode. An important quantity of a cavity is its free spectral range (FSR), which is the distance (in the frequency domain) between two subsequent modes, and given (for a confocal cavity) by:

$$FSR = \frac{c_n}{4d} \tag{3.2}$$

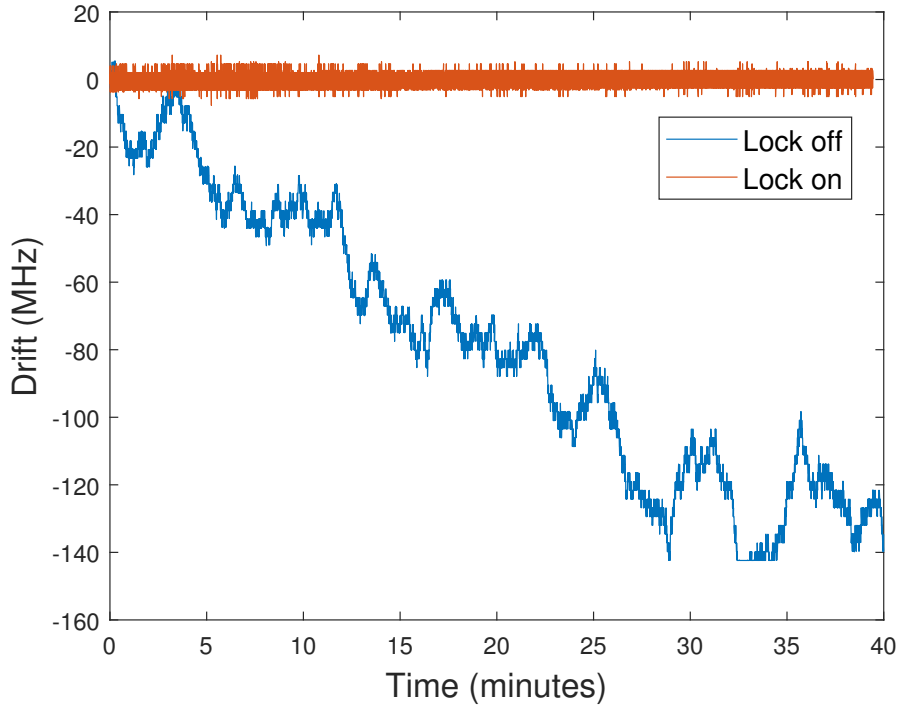For the cavity used in this setup, the FSR was 1.5 GHz.

Figure 3.4: The drift of the ECDL relative to the HeNe laser over time, in MHz. Without stabilization (lock off), the drift is much larger and erratic compared to when the stabilization is engaged (lock on). In the stabilized case, the drift does not exceed 8 MHz and is concentrated in the ± 2 MHz range.

The light enters the cavity through one mirror, the incoupling mirror. After making several round trips inside the cavity, the light can exit through the other mirror, the outcoupling mirror. This light is then detected by a photodiode. Using piezzo elements, the distance between the mirrors can be changed. When this distance is some multiple of the wavelength of the (laser) light that is coupled in, the cavity is resonant to this light and the transmission signal measured on the other side by the photodiode increases. Using an SA201-EC interferometer control box (ICB) from Thorlabs, the piezzo elements are driven and the length of the cavity is scanned. By feeding the trigger signal from the ICB into a data acquisition card (PCI-6023E from National Instruments) together with the signal from the photodiode, the PCI card will sample a specified number of values from the photodiode at the start of each individual scan. The result is a transmission signal by plotting the scanning time against the signal from the photodiode. Using the scanning range and voltage offset of this ICB, it is ensured that at least one spectral range is scanned, in which case two reference peaks will show up in the transmission signal.
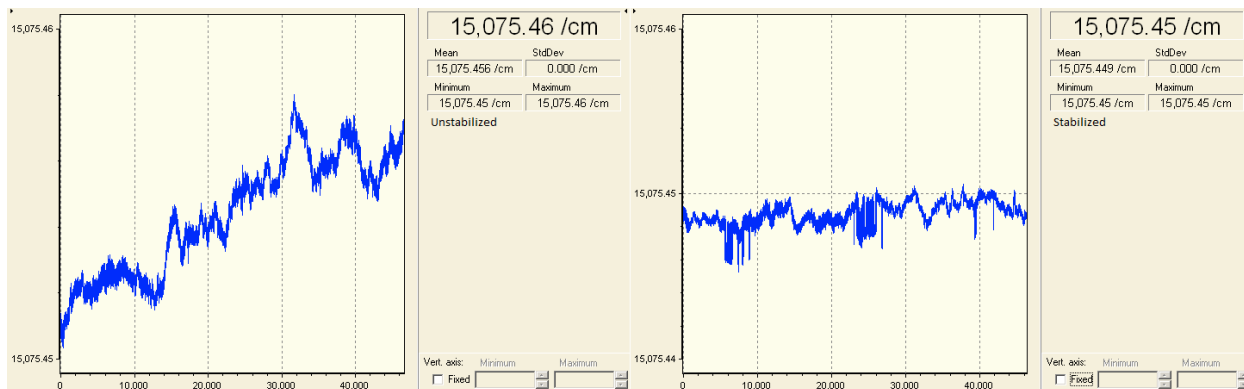
Figure 3.5: Wavelength (in wavenumbers, 1 cm^{-1}= 10^7 nm $\approx 3 \cdot 10^{10}$ Hz) of the ECDL as recorded by a wavelength meter corresponding to the same measurements depicted in figure 3.4. The left (right) half shows the wavenumber when the locking program is off (on). The horizontal axis corresponds to the measurement number, and the total measurement time in both cases is 40 minutes.

Since two laser beams are coupled into the cavity (originating from the ECDL and the HeNe reference laser), the transmission signal will consist of three or four peaks if the cavity and all the incoming laser beams are properly aligned, depending on the relative positions of the peaks of the different lasers and the settings of the ICB. The laser locking program will then have to be told which two peaks originate from the reference laser (HeNe). It recognizes a signal as a peak after it crosses a certain threshold, which can be adjusted in the program. This should be tuned in such a way that no more than four peaks are detected. When transmission peaks approach the edges of the scanning range, they get distorted and might be recognized as multiple peaks or the signal might even drop below this threshold value. Such a situation can be avoided by adjusting the offset voltage on the ICB, which moves the transmission peaks over the scanning range. Over time, the peaks tend to drift towards these edges, which means that over timescales of about 1 hour one will have to adjust this offset in order to keep the program from losing track of the peaks. This could be automated

32

in the future by implementing a feedback signal that adjusts the offset in such a way as to keep the reference peaks at the same place in the scanning range at all times.

When engaged, the program will stabilize the ECDL to the reference laser. This is done using a feedback signal from the program, which serves to keep the relative distance between the peaks of the reference laser and the ECDL the same. The position of these peaks is determined by looking at the derivative of the transmission signal, more specifically at its zero crossing. As a result, it is desirable to have very well-defined, sharp peaks, resulting in clear zero crossings in the derivative. This can be achieved by proper alignment of the cavity and the respective laser beams.

Figure 3.4 shows the drift of the ECDL relative to the HeNe laser over the course of 40 minutes. Without stabilization, this drift is significant and erratic. When the locking program is engaged, the drift is much smaller and centered around zero. In order to convert the relative position as given by the laser locking program into MHz, we use the fact that the FSR of the cavity is 1.5 GHz, which means that a relative difference of 1 corresponds to a frequency difference of 1.5 GHz. The standard deviation (when the locking is engaged) of the relative position then translates into a stability of 1.5 MHz. Figure 3.5 shows the absolute wavelength (in wavenumbers) during the same 40 minute measurement, as measured by a wavelength meter. From both figure 3.3 and 3.5 one can see both how necessary and effective the stabilization is. The patterns in both figures are similar in shape, meaning that the stability achieved from this locking method rivals the accuracy of the wavelength meter.

Chapter 4

Characterizing the beam

We will now discuss some of the properties of the source as found in the past year or so. First, an estimate of the number of SrF molecules detected per pulse will be derived, using both the LIF and absorption detection signal. We will then move on to scans of the main parameters associated with a cryogenic source, namely: the cell temperature, buffer gas flow rate, and ablation energy. The general behavior as these parameters change will be described, and we will somewhat quantify the performance of the source in order to find the optimal range of parameters. Finally, some of the effects observed in the aforementioned scans of the primary parameter space will be considered in more detail. These effects have not yet been reported within the context of a cryogenic source, but have been observed in the past in different experimental contexts. While intriguing in their own right, a complete understanding of these phenomena may not be necessary in order to fulfill the ultimate goal of measuring the eEDM, so we will only go in as much detail as is needed. Recommendations on how to deal with possible complications will be given, along with a general framework to analyze the extent of the effects.

4.1   Estimating the number of molecules

Since we have implemented two distinct detection methods, absorption and LIF, both can be used to estimate the number of SrF molecules produced per pulse. While directly proportional to the signal (voltage for absorption and counts in the case of LIF), the exact number also depends on geometric factors and molecular properties. We will now briefly compare the methods used to extract the number of molecules from these different detection methods. Note that the signal used in both cases has been acquired using a Sr metal target instead of the SrF_2 salt target used in the scans of the neon flow rate, cell temperature, and ablation laser energy which will be discussed afterwards. When the target changes from one section to the next, this will be stated explicitly.

4.1.1 Estimating the number of molecules from the absorption signal

The process of absorption can be described rather generally using the Lambert-Beer law [20]:

$$P = P_0 e^{-n\sigma_{\text{abs}}L} \tag{4.1}$$

Here n denotes the number density of the absorbing species, L the path length the light has to travel through the sample, P_0 the power of the light entering the sample, and P the power of the light exiting it. The optical absorption cross section σ_{abs} combines with L and n such that the product $n\sigma_{\text{abs}}L$ tells us what fraction of the light is absorbed by the sample, or in other words, the probability that a photon is absorbed by a sample particle.

In our setup, the absorption probe laser crosses the molecular beam at a distance of 5 mm from the exit of the cell. The laser light used in both the absorption and LIF detection schemes originate from the same home-built extended cavity diode laser, as described in chapter 3. To reiterate, this laser light is used to drive the $A^2\Pi_{1/2}$ ($v' = 0$, $J = 1/2$) $\leftarrow$ $X^2\Sigma^+$ ($v = 0$, $N = 1$) transition at a wavelength of 663 nm. A typical absorption signal is shown in figure 4.2, which is the signal used in this section to estimate the number of molecules per shot.

Assuming that the molecular beam exiting the cell has a uniform n in its entire volume, equation 4.1 can be rewritten as [34]:

$$N = \frac{A_{\text{beam}}v}{\sigma_{\text{abs}}L} \int \ln\left(\frac{P_0}{P}\right) dt \tag{4.2}$$

P and P_0, or rather their ratio, is simply what is measured, and we integrate this over time.

v is the forward velocity, which can be obtained from the fluorescence signal. The peak arrival time corresponds to this mean velocity, since we know the distance from the source to the detection area (30 cm).

A_{beam} is the cross-sectional area of the molecular beam, can be estimated from the size of the exit aperture. Since we measure the absorption signal close to this exit, the beam can be assumed to not have expanded significantly at this point. The aperture (diameter of 4.5 mm) is however larger than the probe laser beam (diameter of 4 mm), so the probe beam will "miss" part of the molecular beam. We will investigate how large this missed fraction is shortly.

L has been explained before as the path length traveled by the probe beam.

σ_{abs} is the absorption cross section, which can be calculated. Following the discussion in reference [20], it can be written as:

$$\sigma_{\text{abs}}(\omega) = \frac{3\pi^2 c^2}{\omega_0} A_{21} g_H(\omega) \tag{4.3}$$

Here A_{21} is the Einstein coefficient for spontaneous emission, and $g_H(\omega)$ the line shape function:

$$g_H(\omega) = \frac{1}{2\pi} \frac{\Gamma}{(\omega - \omega_0)^2 + \Gamma^2/4} \tag{4.4}$$

Where ω_0 is the resonance frequency and Γ is the natural linewidth of the transition. This expression greatly simplifies if we assume the following:

First, we set $\omega = \omega_0$, since we will be detecting on-resonance. Secondly, we consider the SrF atom to effectively be a two-level system. This simplification is valid enough to give us an order-of-magnitude estimate, since this molecule has highly diagonal Franck-Condon factors [23] and we are probing the $A^2\Pi_{1/2}$ ($v' = 0$, $J = 1/2$) $\leftarrow$ $X^2\Sigma^+$ ($v = 0$, $N = 1$) transition. In this case, decay from the upper to the lower level is the only possible decay, and as a result $A_{21} = \Gamma$ [20]. The simplified expression then becomes:

$$\sigma_{\mathrm{abs}} = \frac{3\pi^2 c^2}{\omega_0}\Gamma\frac{1}{2\pi}\frac{4}{\Gamma} = \frac{3\lambda_0^2}{2\pi} \tag{4.5}$$

Where $\lambda_0 = 2\pi c/\omega_0$ was used to express $\sigma_{\mathrm{abs}}(\omega)$ in terms of the resonance wavelength λ_0.

Before we examine the measured absorption signal, we will now briefly consider the geometry in order to determine how much of the molecular beam will actually be probed.
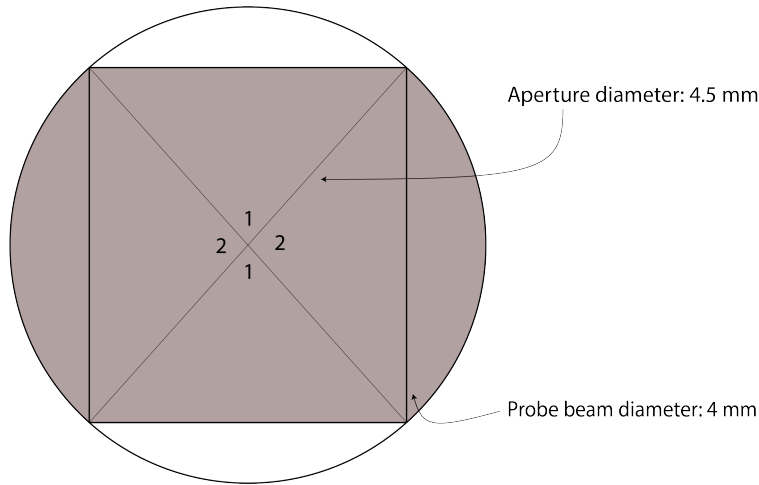
Figure 4.1: A sketch of the overlap (shaded) between the exit aperture and the probe beam.

Given the assumption that the molecular beam will have roughly the same size as the exit aperture d_a, it should have a diameter of 4.5 mm. The resulting total area of the exiting beam is then $\pi(\frac{d_a}{2})^2$. The probe beam has a diameter d_p of 4 mm and crosses the molecular beam perpendicularly. Figure 4.1 shows the outline of both in the same plane. The overlap between both beams essentially consists of two parts: two triangles (denoted 1 in the figure) and two slices of the aperture's total area (denoted 2 in the figure). The area covered by the two triangles (labeled 1) is clearly $2 \times \frac{1}{2}d_p \times \sqrt{(\frac{d_a}{2})^2 - (\frac{d_p}{2})^2} = \frac{1}{2}d_p\sqrt{d_a^2 - d_p^2}$.

The total area of the two slices (labeled 2) can be written as the following integral:

$$2\int_{-\theta_1}^{+\theta_1} \int_0^{\frac{d_a}{2}} r\,dr\,d\theta \tag{4.6}$$

Which is a sum of two integrals in polar coordinates from a radius of zero to the radius $\frac{d_a}{2}$ of the aperture, and from the angle $-\theta_1$ to $+\theta_1$. The angle θ_1 is simply defined by $\sin\theta_1 = \frac{d_p}{d_a}$.

The result is:

$$2\left(\frac{d_a}{2}\right)^2 \sin^{-1}\left(\frac{d_p}{d_a}\right) = \frac{d_a^2}{2}\sin^{-1}\left(\frac{d_p}{d_a}\right) \tag{4.7}$$

Adding the two together, the overlap is:

$$\frac{1}{2}d_p\sqrt{d_a^2 - d_p^2} + \frac{d_a^2}{2}\sin^{-1}\left(\frac{d_p}{d_a}\right) \tag{4.8}$$

Using the aforementioned values of $d_a = 4.5$ mm and $d_p = 4$ mm, the overlap makes up about 96% of the total aperture area. To account for the part of the molecular beam that is missed, the number of molecules as calculated using equation 4.2 needs to be multiplied by a factor 1.05.
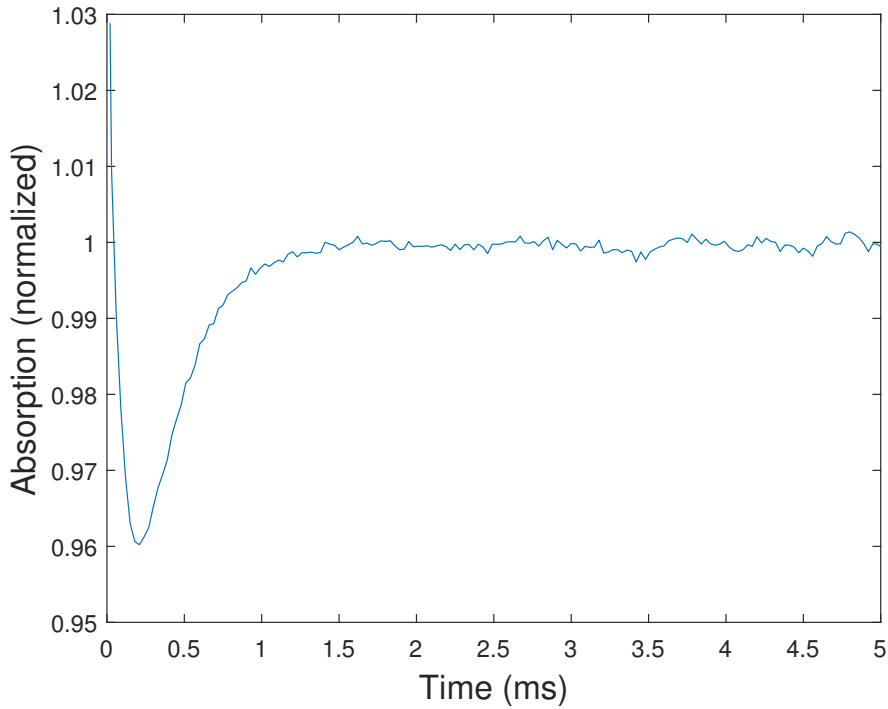
Figure 4.2: A typical absorption profile using a Sr metal target. A flow rate of 9 SCCM, a cell temperature of 17 K, and an ablation energy of 67 mJ per shot were used. The absorption of about 4% translates into an estimated 5.5×10^9 molecules per shot. This profile is the result of averaging the voltage from the photodiode over all 2744 shots during the measurement time. Only the first 5 ms of the 100 ms pulse are shown, since the molecular signal tends to be in this range while the rest of the pulse consists of the background signal. The probe laser had a diameter of 4 mm and a power of 0.3 mW.

Not all molecules which leave the cell will be detected by the probe laser beam though, since some of them might have high enough transverse velocities such that the Doppler shift causes them to no longer be resonant to the laser light. The Doppler shift of a molecule with velocity v and transition frequency ω_0 (wavelength λ_0) will be given by [20]:

$$\delta = \omega_d - \omega_0 = \vec{k}\cdot\vec{v} \tag{4.9}$$

This would mean that a molecule traveling with a velocity of v relative to a laser beam would experience a Doppler shift of:

$$\delta_f = \frac{kv}{2\pi} = \frac{v}{\lambda_0} \tag{4.10}$$

If we assume our detection laser to have a linewidth of 1 MHz [29], this means that only molecules with a transverse velocity of $\lambda_0 \cdot \delta_f = 0.7$ m/s will be detected. Assuming that the transverse velocity is approximately Gaussian and centered around 0 with a spread of ± 30 m/s [19], the fraction of molecules in this ± 0.7 m/s velocity range is about 0.02. To account for the undetected molecules, we multiply by a factor 57. This, combined with the other factors derived in this section and equation 4.2, leads to an estimate of 5.5×10^9 molecules per shot.

The proposal requires that 4×10^9 molecules can be extracted per shot and are in the state used for deceleration [19]. While the estimate arrived at in this section was achieved using SrF instead of the BaF molecules used in the final experiment, it is clear that at least the number of molecules as required for the eEDM experiment can be produced using this source. The extraction efficiency can be roughly derived from γ_{cell} as described by equation 2.21, which shows that $\gamma_{\text{cell}} \propto 1/\bar{v}_{0,b}$. The only factor which changes significantly in the switch from SrF to BaF is the mass of the molecule, and from equation 2.5 it is clear that $\bar{v}_{0,b} \propto \sqrt{1/m}$. It follows that $\gamma_{\text{cell}} \propto \sqrt{m}$. Since BaF is about 47% heavier than SrF, γ_{cell} should be a factor of 1.2 higher after making the switch to BaF. The extraction efficiency of our source under comparable conditions using either BaF or SrF should therefore be at least comparable or move favorable when using BaF. The conditions for this particular absorption signal lead to $\gamma_{\text{cell}} = 0.93$, using SrF. Assuming that the production process inside the cell can produce a comparable number of molecules inside the cell in both cases, the end result is that one can expect the number of extracted BaF molecules per shot which are in the right state to be decelerated to be either comparable to or larger than the estimate stated in this section.

The absorption signal only gives us an estimate for this number just after the cell exit though. From the cell exit to the decelerator, the beam will inevitably diverge due to the finite distance between the two components, as we have discussed in chapter 3 (see the section on phase-space matching). This distance is planned to be roughly equal to the distance between the cell exit and the LIF detection, which is 30 cm. By estimating the number of detected molecules at this distance we can get an idea of how many molecules we might lose due to this divergence.

4.1.2 Estimating the number of molecules from the LIF signal

The laser light from the 663 nm ECDL as described in chapter 3 is also used in the LIF detection of the molecular beam, which takes place 30 cm after the cell exit. This laser beam crosses the molecular beam perpendicularly and is then reflected back by a mirror. Its diameter can be tuned using a beam expander, and is typically around 4 mm in size. Once the laser light exits the fiber and enters the setup, it has a power in the order of 1 mW, which can be varied as well. The fluorescent light emitted by the molecular beam is collected by a set of plano-convex lenses and a mirror. The collected light then passes through a narrow bandpass (bandwidth of 20 nm) filter, which is centered around 661 nm, and is then focused onto a photomultiplier tube (PMT) using a lens and an iris.
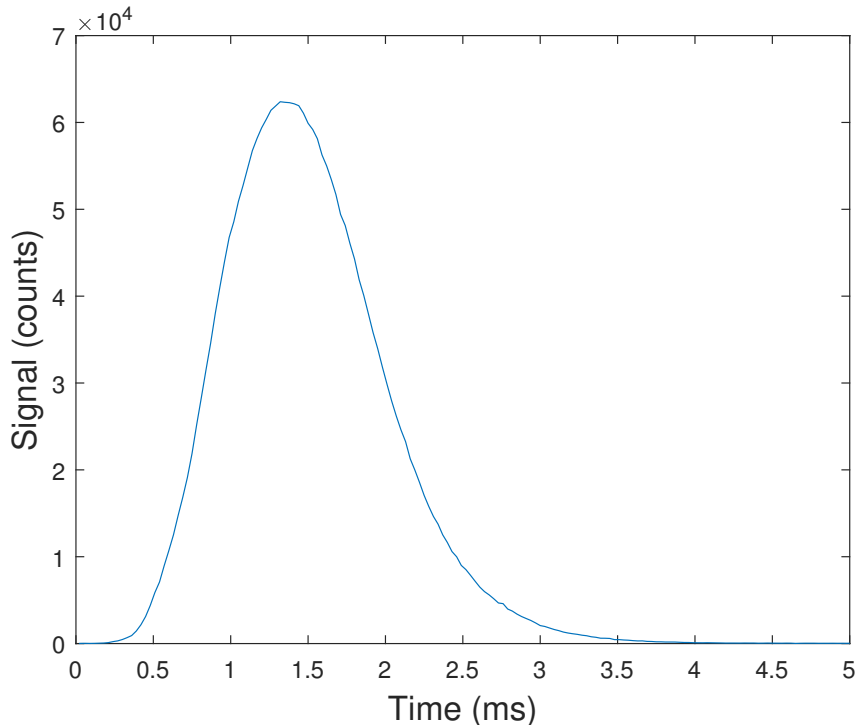
Figure 4.3: Typical LIF signal 30 cm from the cell exit, using the same experimental conditions as figure 4.2, accumulated over 2744 shots. The background counts are in the order of 20 counts, with a standard deviation of about 5. Only the first 5 ms of the 100 ms pulse are shown, since the molecular signal tends to be in this range while the rest of the pulse consists of the background signal. The probe laser beam had a diameter of 4 mm and a power of 1.7 mW.

This lens system collects only a fraction of the total emitted fluorescence volume. This can be expressed in terms of the collected solid angle Ω, compared to the total solid angle, which would be 4π [29]:

$$\Omega = 2 \times 2\pi \left(1 - \frac{d}{\sqrt{r^2 + d^2}} \right) \tag{4.11}$$

Where r is the radius of the lens and d its distance to the molecular beam. In our setup this is 1.1 sr.

In order to convert the number of photon counts into the number of detected molecules, we need to include several correction factors to take into account the efficiency of the optics and the detection process. The aforementioned collected solid angle Ω is one of those factors, as well as the quantum efficiency of the PMT (ϵ_q) at the detection wavelength of 663 nm (specified by the manufacturer to be 0.33), the efficiency of the optics (ϵ_o, estimated to be 0.8), and the correction due to the Doppler shift ($\delta_d = 57$) as found in the previous section.

We will also need to account for the number of photons scattered per molecule (n_{scat}). The detection laser drives the $A^2\Pi_{1/2}$ ($v' = 0$, $J = 1/2$) $\leftarrow X^2\Sigma^+$ ($v = 0$) transition, and once a molecule is excited it can effectively decay back into two kinds of states. First, it can decay to a state which is coupled to the excited state by the detection laser, after which another photon can excite the molecule and the cycle repeats. Alternatively, the molecule decays into a dark state, where the detection laser can no longer excite the molecule and this scattering process stops. From these two possible decay paths it follows that the average number of scattered photons per molecule is given by the geometric series [46]:

$$n_{\mathrm{scat}} = \frac{1}{1-p} \tag{4.12}$$

Where p is the probability that the excited molecule decays back to a state which is coupled to the $A^2\Pi_{1/2}$ ($v' = 0$, $J = 1/2$) state by the detection laser. Using SrF, and the aforementioned transition combined with the laser system as described in chapter 2, $p = 0.9$ [29, 43] and $n_{\mathrm{scat}} = 10$.

A typical LIF signal is shown in figure 4.3, where the same experimental conditions apply as to the absorption signal in figure 4.2. After subtracting the background counts the total number of counts due to SrF molecules can then be calculated. This has to be corrected (multiplied by a factor 1000) for the fact that a neutral density filter has been placed between the probe beam and the detection setup. The number of counts would at times be so high that the PMT would shut off, so a neutral density filter was introduced to reduce the power of the probe laser beam by a factor 1000. The resulting number of molecules is an accumulation over 2744 shots though, so in order to obtain the number of photons detected per shot one must divide by a factor 2744, leading to the number of counts per shot $N_{\mathrm{counts/shot}}$.

All these considerations combine such that the total number of detected molecules per shot is:

$$N = \frac{4\pi\delta_d}{\Omega\epsilon_q\epsilon_o n_{\mathrm{scat}}} N_{\mathrm{counts/shot}} \tag{4.13}$$

Using the aforementioned experimental conditions and correction factors, we have detected 2.3×10^8 molecules per shot at a distance of 30 cm from the cell exit using a probe laser with a diameter of 4 mm. This means a loss of a factor of about 24 occurs in the 30 cm between the absorption and LIF measurements.

4.1.3 Conclusions

We have seen that the source as described in chapter 3 can in fact deliver the amount of molecules per shot as demanded by the NL-eEDM proposal (4×10^9 molecules per shot in the state used for deceleration [19]). Even though the results presented in this section were achieved with SrF, an argument was put forth to argue that this number will either remain comparable or improve when the switch from SrF to BaF is eventually made. Between the absorption and LIF detection there is a loss of a factor of about 24. It makes sense that the number of detected molecules found using LIF is smaller than the number of detected molecules found using absorption, since the former takes place 30 cm after the cell exit while the latter takes place 5 mm after the cell exit. In the meantime, the molecular beam has spread out and the molecules detected by the absorption probe beam do not necessarily make it into the LIF detection region. Moreover, since the LIF probe had a diameter of 4 mm (equal to the diameter of the rings of the decelerator) and takes place at a distance from the cell which is comparable to the planned location of the decelerator, this gives us an estimate of the losses due to this distance if no phase-space matching measures (as discussed at the end of chapter 2) are taken.

4.2 The molecular signal as a function of the main experimental parameters

We will now show how the main parameters of our source influence the molecular beam. To be exact, we will see how the time-of-flight (TOF) profiles as measured by LIF detection change as the cell temperature, neon flow rate, and ablation energy change. The general trend as these parameters are scanned will be described, mostly in terms of the amount of signal (number of counts), and the arrival time (and width) of the central peak. In this section, we will interpret the TOF profile to be roughly related to the forward velocity distribution of the beam through $v = L/t$. Here L denotes the distance between the source of the molecules to the detection zone, which in our case is 312 mm. Later arrival times thus correspond to slower molecules, while their width corresponds to the velocity spread (and by extension their transverse temperature). As an approximation in order to get an idea of the general behavior of the beam, this interpretation is satisfactory. These parameter scans will reveal a previously unreported effect, namely a double peak structure which appears in these TOF profiles under certain conditions, but we will discuss these conditions and the hypothesized origin of this effect in a separate section. In this section, the SrF_2 salt target was used to produce SrF molecules. The main difference between targets is the ablation energy needed to produce a similar amount of molecules. More specifically, the SrF_2 salt target requires higher ablation energies compared to the Sr metal target.

4.2.1 Neon flow rate

Figure 4.4 shows the LIF signal (counts) over time (ms) during a scan of the neon flow rate from 1 to 40 SCCM , using a cell temperature of 28 K and an ablation energy of 191 mJ per shot. From equation 2.8 it follows that the Reynolds number ranges from 8 to 336, and from equation 2.21 it follows that that γ_{cell} ranges from 0.08 to 3. These Reynolds numbers lead to an expected mean forward velocity ranging from 125 to 240 in this flow rate range. If the approximation $v = L/t$ were valid, this translates into an expected arrival time of 2.5 ms to 1.3 ms as the flow rate is increased from 1 SCCM to 40 SCCM.

From the calculated γ_{cell} values, an increase in signal is expected as the flow rate is increased, since γ_{cell} scales linearly with the flow rate and serves as an indication of the extraction efficiency. A higher flow rate means that more molecules reach the cell exit before diffusing to the cell walls. This increase in signal is indeed observed in figure 4.4. After a flow rate of about 30 SCCM the signal seems to saturate though, which likely means that the extraction efficiency reaches its maximum at this point. As the flowrate increases, the signal is focused and becomes narrower, meaning the transverse temperature decreases. From the discussion on thermalization length and mean free path this was expected, since both decrease (linearly) as the flow rate increases, meaning there will be more collisions with the buffer gas inside the cell before extraction which reduce the temperature of the molecular beam. The expected decrease in arrival time of the signal is visible in the same figure. The Reynolds number as derived in chapter 2 scales linearly with the flow rate as well, and similar to the saturation in velocity (for high Reynolds numbers) illustrated in figure 2.4, the arrival time of the signal in figure 4.4 seems to reach a constant value at the highest flow rates. The
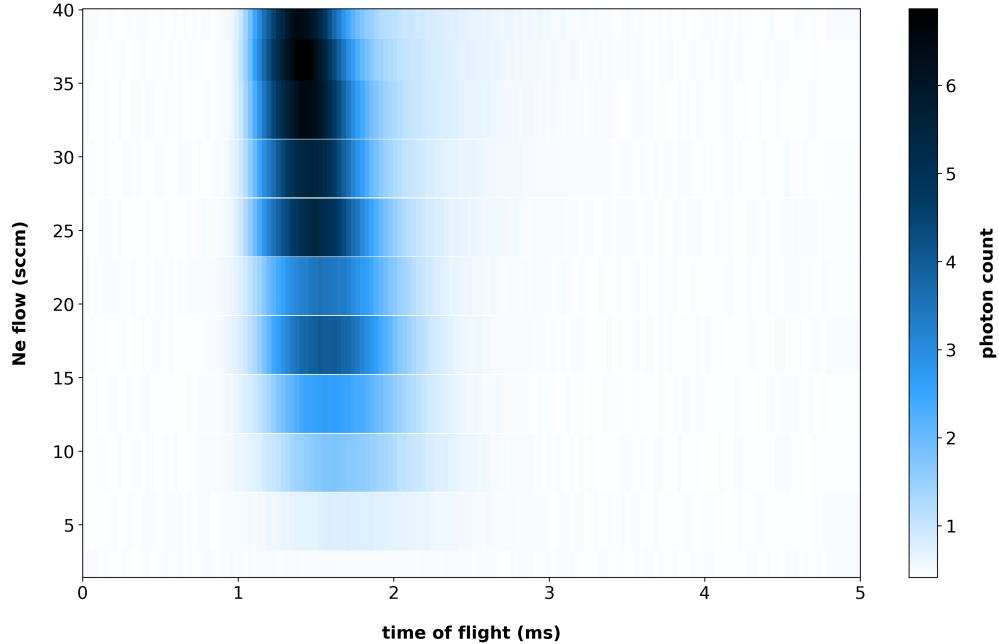
Figure 4.4: A scan of the neon flow rate from 1 SCCM to 40 SCCM, using a cell temperature of 28 K and an ablation energy of 191 mJ per shot. The horizontal axis represents arrival time (ms) while the vertical axis shows the flow rate (SCCM). The color shows the amount of signal (photon counts) for a given timestamp and flow rate. Higher flow rates clearly result in more signal, but also a more narrow central peak at earlier times, meaning a faster beam with a lower translational temperature.

expected arrival times as derived from the Reynolds numbers are almost reproduced by the scan, which starts with a peak arrival time of about 2 ms and decreases towards a value of about 1.4 ms. The discrepancy is the result of the fact that the expression for Re as derived in chapter 2 is only an approximation and the relation between the forward velocity and Reynolds number is likewise only meant as an indication of the general behavior and not exact. In addition, the assumption that $v = L/t$ (while a useful approximation) may not be valid, but this is a separate topic we will discuss towards the end of this chapter.

Figure 4.5 shows an additional scan of the flow rate, again from 1 SCCM to 40 SCCM and using an ablation energy of 191 mJ per shot, but in this case the cell was at a temperature of 22 K. These conditions lead to a Reynolds number ranging from 9 to 380, and γ_{cell} ranging from 0.1 to 3.6. These Reynolds numbers lead to an expected mean forward velocity ranging from 124 m/s to 213 m/s in this flow rate range. If the approximation $v = L/t$ were valid, this translates into an expected arrival time of 2.5 ms to 1.5 ms as the flow rate is increased from 1 SCCM to 40 SCCM. As is clear from figure 4.5, the signal does not follow this trend. After flow rates of about 5 SCCM, the central peak seems to split in two, and both components seem to saturate about some arrival time (1 ms for the fast peak, 2.1 ms for the slow peak) while their width stays relatively constant, while the fast peak seems to be rather narrow (corresponding to a lower temperature) compared to the relatively broad (higher temperature) slow peak. The fast peak seems to contain most of the signal. This double

peak structure has not been reported before in the context of a cryogenic source, making its appearance unexpected.

Next, we will discuss scans of the cell temperature, and under certain conditions a similar structure emerges. We will only briefly discuss its features though, before examining this phenomenon in more detail in a separate section.
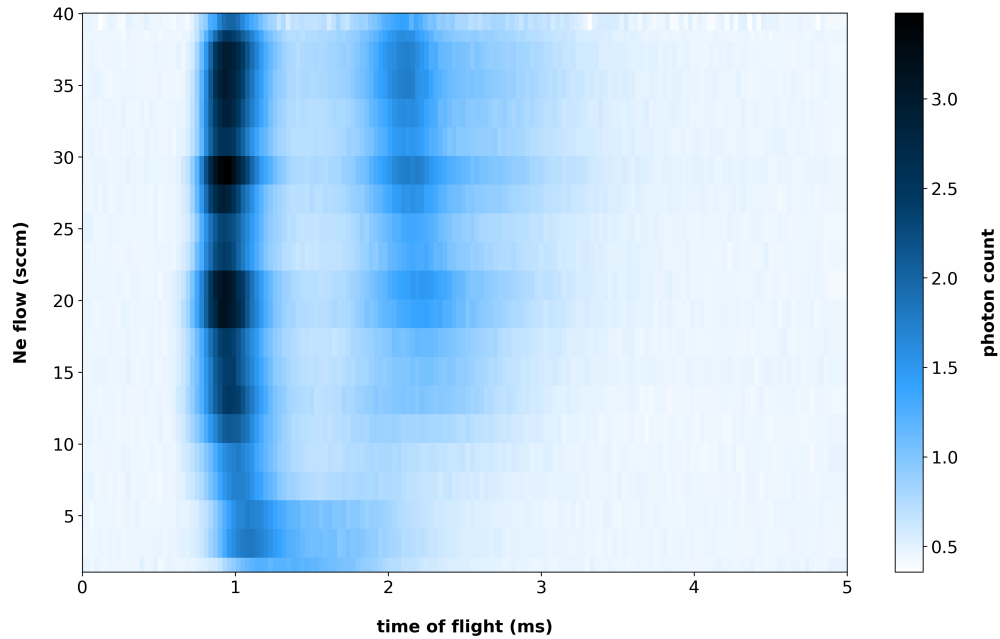
Figure 4.5: A scan of the neon flow rate from 1 SCCM to 40 SCCM, using a cell temperature of 22 K and an ablation energy of 191 mJ per shot. The horizontal axis represents arrival time (ms) while the vertical axis shows the flow rate (SCCM). The color shows the amount of signal (photon counts) for a given timestamp and flow rate. The signal seems to split in two after a neon flow rate of about 5 SCCM, after which a fast and slow peak develop.

4.2.2 Cell temperature

Figure 4.6 shows the LIF signal (counts) over time (ms) during a scan of the cell temperature from 14 to 25 K, using a neon flow rate of 10 SCCM and an ablation energy of 191 mJ per pulse. From equation 2.8 it follows that the Reynolds number ranges from 89 (for a cell temperature of 25 K) to 119 (for a cell temperature of 14 K), and from equation 2.21 it follows that that γ_{cell} ranges from 0.85 (for a cell temperature of 25 K) to 1.14 (for a cell temperature of 14 K). The γ_{cell} values indicate that the extraction from the cell should be fairly efficient, with minimal losses due to the SrF molecules diffusing to the cell walls. These Reynolds numbers lead to an expected mean forward velocity ranging from 169 to 226 m/s in this temperature range. If the approximation $v = L/t$ were valid, this translates into an expected arrival time of 1.8 ms to 1.4 ms as the cell temperature is decreased from 25 K to 14 K.
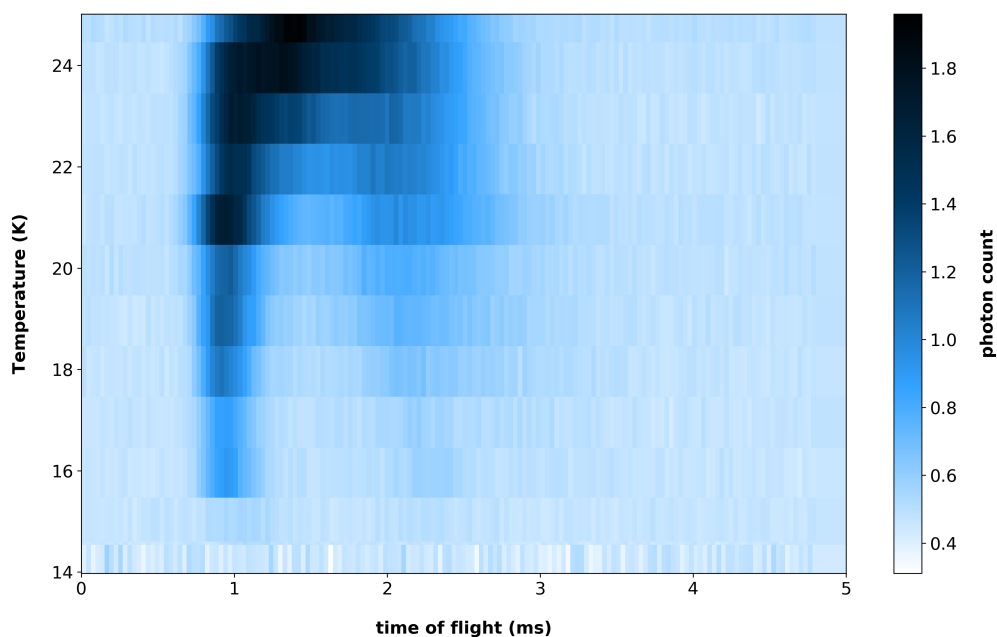
Figure 4.6: A scan of the cell temperature from 14 to 25 K, using a neon flow rate of 10 SCCM and an ablation energy of 191 mJ per shot. The horizontal axis represents arrival time (ms) while the vertical axis shows the flow rate (SCCM). The color shows the amount of signal (photon counts) for a given timestamp and cell temperature. A double peak structure appears at low cell temperatures.

As the cell temperature, and by extension the buffer gas temperature, is lowered, the SrF molecules will need more collisions to thermalize, which might not be possible given the fixed, finite distance from the target to the cell exit. At lower temperatures, the buffer gas and SrF molecules will also simply freeze to the cell walls, and could even obstruct the buffer gas inlet or cell exit, resulting in less signal until one or both are blocked off by frozen material.

As figure 4.6 shows, the double peak structure emerges when scanning the cell temperature as well. Below about 22 K the signal splits into a narrow fast peak and a more broad slow peak. Below about 16 K, there is no signal, likely because either the cell exit or buffer gas inlet are obstructed by frozen material. By heating up the cell, the molecular signal recovered, which supports this hypothesis. Additional scans of the cell temperature using different flow rates show the same double peak structure as the cell temperature is lowered. For higher flow rates, this split occurred at higher cell temperatures. While the fast peak is similar in its development as the cell temperature is decreased, the slow peak generally gets slower for higher flow rates, approaching arrival times as late as 3 ms using a flow rate of 20 SCCM and a cell temperature of 17 K. When using higher flow rates, the signal decreases more quickly as the cell temperature is lowered though, so there is only a very small fraction of molecules at these exceptionally late arrival times. This behavior using different buffer gas flow rates is can be seen in more detail in the appendix. Because of their similarities they are not show here explicitly, but only described qualitatively.

We have now seen this double peak structure appear in scans of both the flow rate and the cell temperature. In the flow rate scans, the splitting did not occur when using a relatively high cell temperature, but by lowering this temperature this structure appeared at higher flow rates. In the scans of the cell temperature, we have seen that the buffer gas flow rate does not prevent the appearance of the double peaks at lower cell temperatures. This seems to suggest that the cell temperature is the main cause, while the flow rate at times might be able to compensate for whatever mechanism drives this splitting. One constant among these scans has been the ablation energy though, so before we dive deeper into these double peaks we will look at a scan of this ablation energy.

4.2.3 Ablation laser energy

In figures 4.7 and 4.8 the signal (counts) as a function of both time and ablation fluence (energy per area) can be seen. During these scans, a neon flow rate of 9 SCCM and a cell temperature of 20 K were used. Using these conditions, it follows from equations 2.8, 2.21, and figure 2.4 that the Reynolds number during this scan is 89, and the expected mean forward velocity is 191 m/s (corresponding to an arrival time of 1.6 ms), with a γ_{cell} of 0.86. The ablation energy has been converted into fluence (J/cm^2), using a beam diameter of 1 mm. We will use the terms fluence and energy rather interchangeably, since both the diameter of the beam (1 mm) and the pulse duration (10 ns) remain the same throughout our discussion.

At high ablation fluences, the number of counts is almost 2 orders of magnitude larger than the lowest measured fluences. Figure 4.8 shows the same scan, but uses a different scaling so these lower fluences are more prominent, but the signals at the lowest fluences are still barely visible. This drastic increase in signal will be addressed in a separate section though.
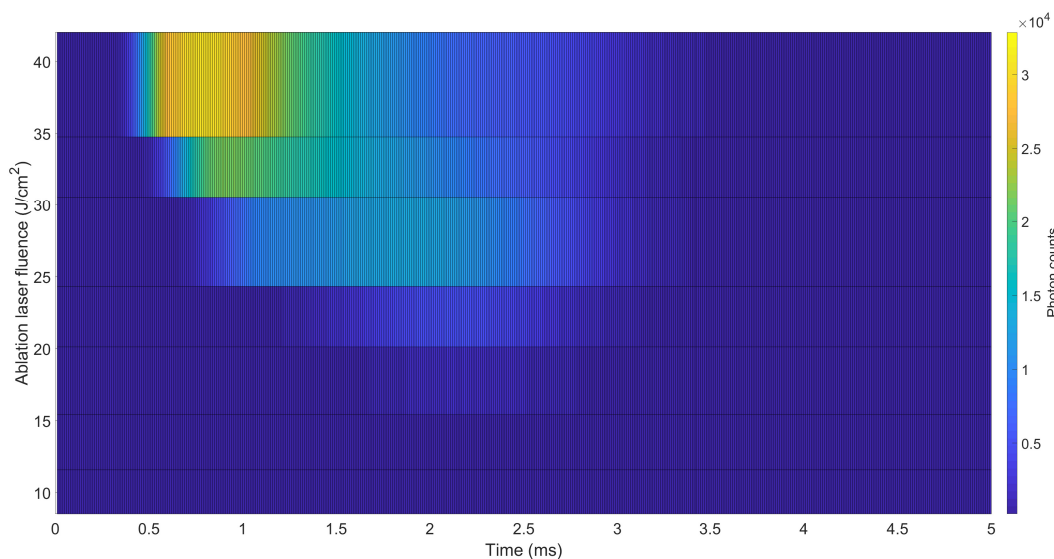
Figure 4.7: A scan of the ablation laser energy, which has been converted into fluence (energy per area, in J/cm^2). A neon flow rate of 9 SCCM and a cell temperature of 20 K were used during the scan. All 8 ablation fluences were measured for 5 minutes. The expected mean forward velocity corresponds to an arrival time of 1.6 ms.

The general trend, as the ablation energy is increased, is that the signal becomes broader and arrives earlier while the total amount of signal also increases. Intuitively, this behavior is as expected. A higher ablation energy likely means that more target material is ablated, resulting in more molecules. A higher ablation energy also results in a higher initial temperature for the species of interest (SrF), which manifests itself in a faster molecular beam due to the higher kinetic energy of the molecules. The higher initial temperature in turn results in a higher translational temperature in the molecular beam, since more collisions are needed

for proper thermalization, but since the flow rate, cell geometry, and cell temperature all remain the same, this might not happen. The higher translational temperature results in a broader velocity distribution, and by extension a broader TOF profile.
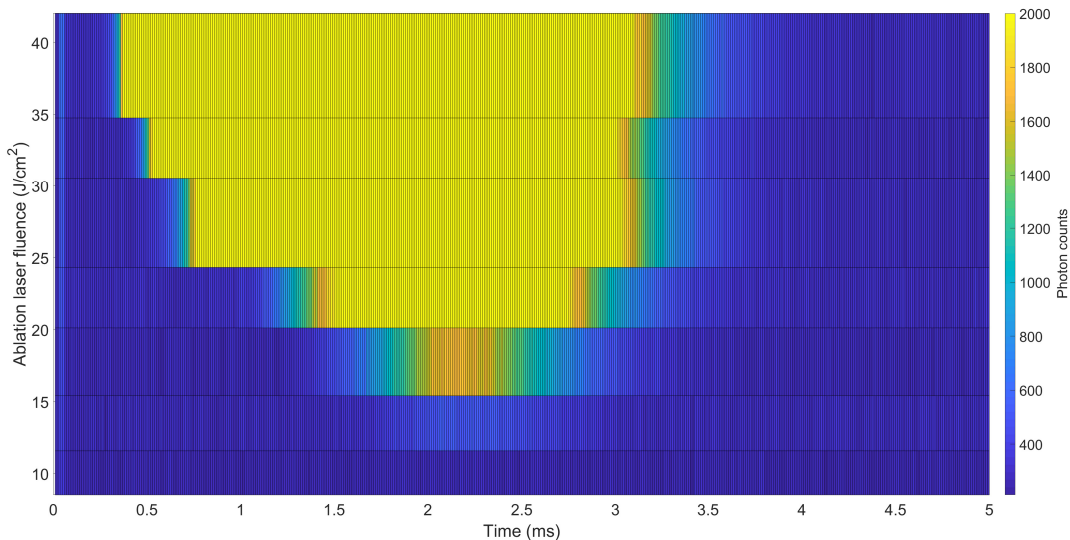
Figure 4.8: A scan of the ablation laser energy, but the scaling of the counts differs from figure 4.7 to show the signal at low laser powers more clearly. Energy has been converted into fluence (energy per area, in J/cm^2). A neon flow rate of 9 SCCM and a cell temperature of 20 K were used during the scan. All 8 ablation fluences were measured for 5 minutes.

Less clear from figures 4.7 and 4.8 is the fact that after a certain ablation energy, the double peak structure as mentioned in the flow rate and cell temperature scans appears. This double peak structure causes the width of the signal to increase drastically for high ablation energies.

To conclude this qualitative discussion, a higher ablation energy generally results in more SrF molecules, but this comes at a cost. The beam will have larger forward velocities and a larger spread, while also introducing the double peak structure mentioned in the previous sections. In the following section we will investigate this double peak structure more closely, and attempt to describe the underlying mechanism to some degree.

4.3   Double peak structure

As we have seen in the previous section, the TOF profile appears to split in two under certain conditions, resulting in a double peak structure. We will now examine this phenomenon in more detail.

Figure 4.9: The TOF profiles for the same ablation energies and experimental conditions as figures 4.7 and 4.8. The lowest ablation energies result in rather small signals compared to medium and high ablation energies. The double peak structure becomes prominent after a fluence of about 24 J/cm^2.

A similar effect has been observed in the past [47], though this has not yet been reported for cryogenic sources. The experiment used pulsed nanosecond ablation of a Ba metal target, which is comparable to our source (10 ns laser pulses), and looked at the TOF profiles obtained using LIF detection. They argued that, after a certain threshold laser fluence, the dominant ablation process is that of phase explosion (also known as explosive boiling). Due to superheating in the irradiated area, its temperature nears the critical temperature, and the surface then breaks down into vapor and equilibrium (liquid) droplets on a short timescale [48]. The underlying mechanism which leads to this phenomenon is not yet fully understood, since it has been argued that subsurface heating might be a cause [49], while the very existence of subsurface heating in this context is still being debated [48]. The result of phase explosion is that the ablation products will be a mix of vapor and liquid droplets. This in turn leads to a fast, Maxwell-Boltzmann-like component and a slower component corresponding to the phase-exploded vapor. The crossing of this threshold fluence is characterized by a sudden increase of mass removal due to ablation [49], which manifests

49

in the form of an increased LIF signal. It should be noted that below this threshold, the droplets are also present, but in very small amounts. This phase explosion phenomenon seems to occur primarily in the case of nanosecond laser pulses [48, 49], and is considered the most efficient (in terms of yield) mechanism for ablation on this timescale or shorter.

When it comes to our cryogenic source, understanding the nature of this double peak structure can be very helpful. As we have seen in the previous section, where we looked at scans of various parameters, the double peak effect broadens the signal, leaving fewer molecules in the central peak. When the threshold fluence is reached, the broadened peaks separate somewhat and one can distinguish two peaks. In order to see whether or not this effect becomes a problem, we will have to look at it in a bit more detail.

4.3.1   Fluence and double peaks

Figures 4.9 and 4.10 show how the TOF profiles develop when the ablation energy is increased, and how the double peak structure changes. Most notably, after a fluence of about 24 J/cm^2 the broadening of the central peak becomes large enough to recognize two distinct peaks which seem to overlap. At first, the slow peak is higher in amplitude, but as the ablation energy increases, the fast peak not only becomes more prominent but also faster.
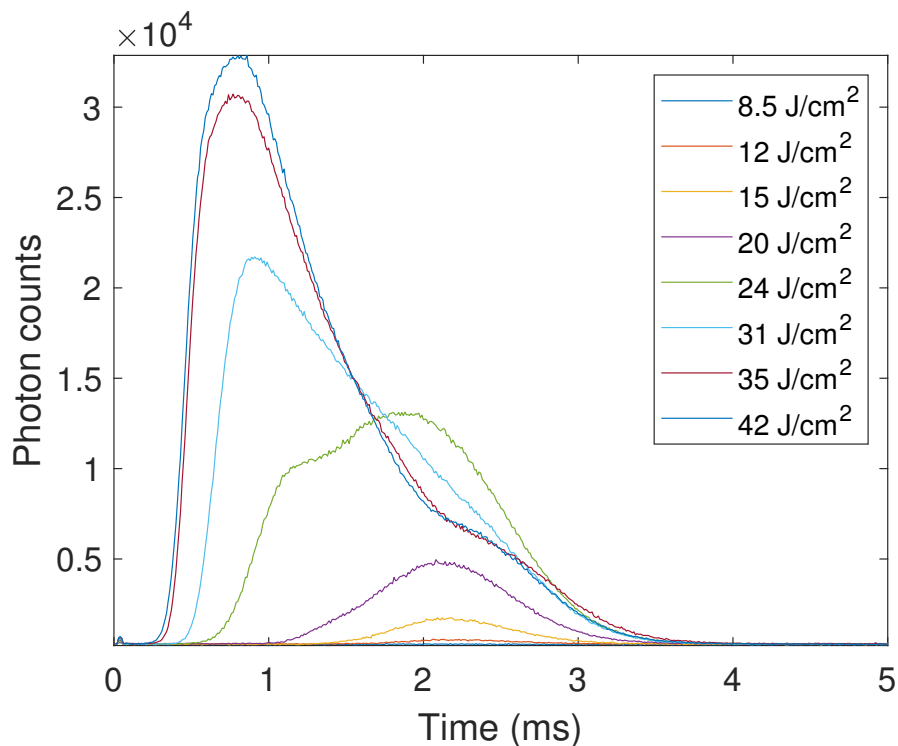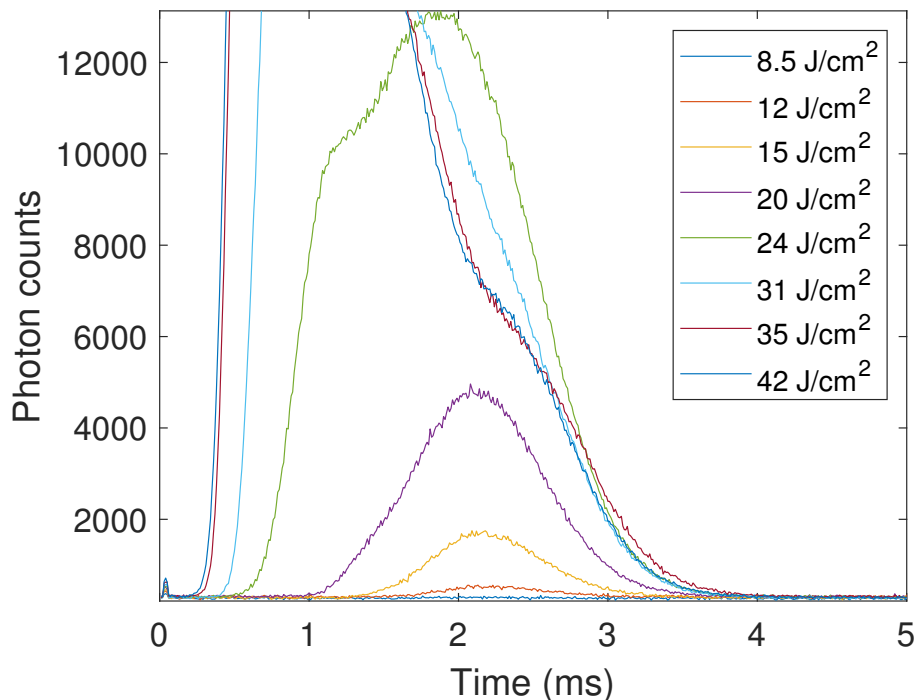

Figure 4.10: The TOF profiles for the same ablation energies and experimental conditions as figures 4.7 and 4.8, but with an adjusted scale to show the behavior at low ablation energies more clearly. The lowest ablation energies result in rather small signals compared to medium and high ablation energies. The double peak structure becomes prominent after a fluence of about 24 J/cm^2.

We can examine the behavior of the two peaks and their potential origin in phase explosion in two ways. First, from the TOF profiles of the various ablation powers, we can extract an estimate of this threshold fluence. By looking at the total (integrated) signal versus fluence, the threshold is the point at which a sharp increase in signal occurs. This threshold fluence is specific to the material of the target (SrF_2 salt in this case), and might also differ depending on the exact target production method. Our targets are scintered and pressed for some time (half an hour to about 2 hours), and depending on these factors one target may be more stable (meaning less shot to shot variation in SrF yield) than the other, or might require higher ablation energies to produce a significant amount of SrF. Figure 4.11 shows the total (integrated) signal, normalized to the number of shots, for the different fluences used to produce figures 4.7, 4.8, 4.9, and 4.10. From this figure, it is clear that a significant increase in signal occurs between a fluence of 20 and 24 J/cm^2. Thus we conclude that the SrF_2 target used in this series of measurements has a threshold fluence of 22 ± 2 J/cm^2. To reiterate, for different targets, this threshold fluence might be different. Since we have not performed this measurement for multiple targets we cannot conclude if this difference is significant or within a few percent yet, but future efforts might investigate this further if the process of phase explosion and the appearance of the double peaks proves to be relevant to the NL-eEDM project.
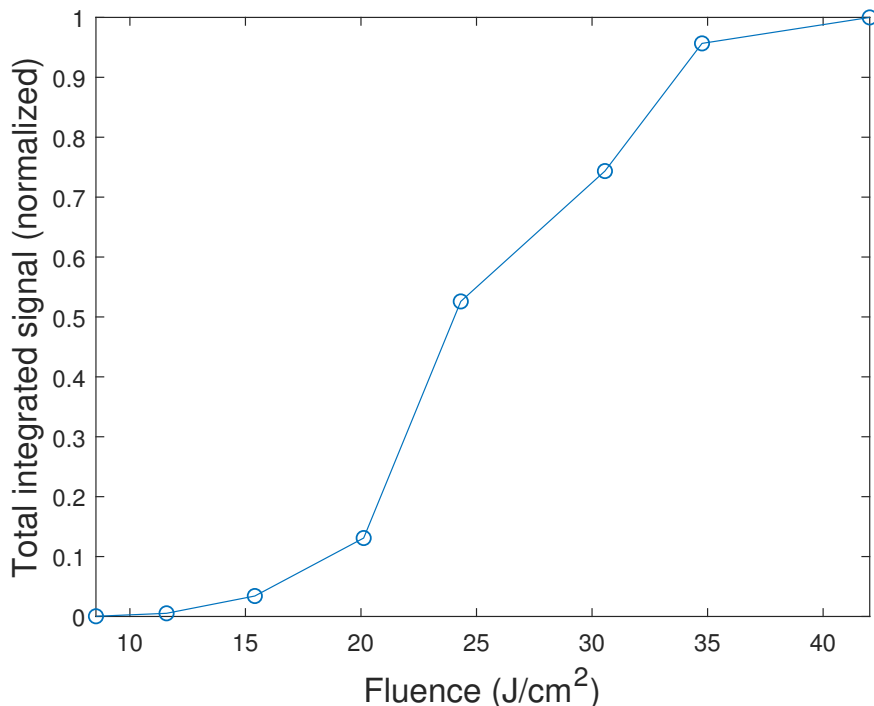
Figure 4.11: The total (integrated) signal per fluence, from the same experimental conditions as figures 4.7, 4.8, 4.9, and 4.10. From a fluence of 20 J/cm^2 to 24 J/cm^2, a significant increase in signal occurs. This corresponds to the threshold fluence, above which the process of phase explosion is the dominant ablation process.

We can examine the behavior of the emerging two peak structure in some more detail by fitting the LIF signal to a Maxwell-Boltzmann distribution, similar to the approach in reference [47]. In the case of this double peak structure, we simply fit the signal to two Maxwell-Boltzmann distributions, corresponding to the two peaks, both with their own characteristic velocity and temperature. In terms of arrival times, a Maxwell-Boltzmann distribution takes the following form:

$$f(t) = A\left(\frac{L}{t}\right)^2 \exp\left(-\frac{(L/t - v_0)^2}{2k_b T}\right) \tag{4.14}$$

Where $f(t)$ is the signal (counts), v_0 the mean velocity, T the (translational) temperature, and A the amplitude. A is simply a normalization factor, the shape of the distribution is governed entirely by v_0 and T.

Figure 4.12: Velocities of both components when fitting the LIF signal to two Maxwell-Boltzmann distributions for the different ablation energies (converted into fluence). At low ablation fluences these values approach one another and ultimately become indistinguishable.

Figures 4.12 and 4.13 show the fitted parameters for the different ablation energies (in terms of fluence), obtained by fitting the LIF signal to two Maxwell-Boltzmann distributions. The (Matlab) scripts used to compute these fits are listed in the appendix. They use nonlinear regression (nlinfit) and give an uncertainty for the fitted parameters based on the Jacobian or estimated variance-covariance matrix. Matlab documentation explains the use of the nlinfit command and these estimates in more detail. At high ablation energies, the signal can be described using two Maxwell-Boltzmann distributions, but after a fluence of

20 J/cm^2 the characteristic velocity and temperature of the two peaks start to overlap and it no longer makes sense to describe the signal in terms of two overlapping peaks. As stated before, at fluences below the threshold the process of phase explosion can still occur, but its effect is small, and as can be seen from both the LIF signals and the fit parameters this simply broadens the central peak without splitting it.
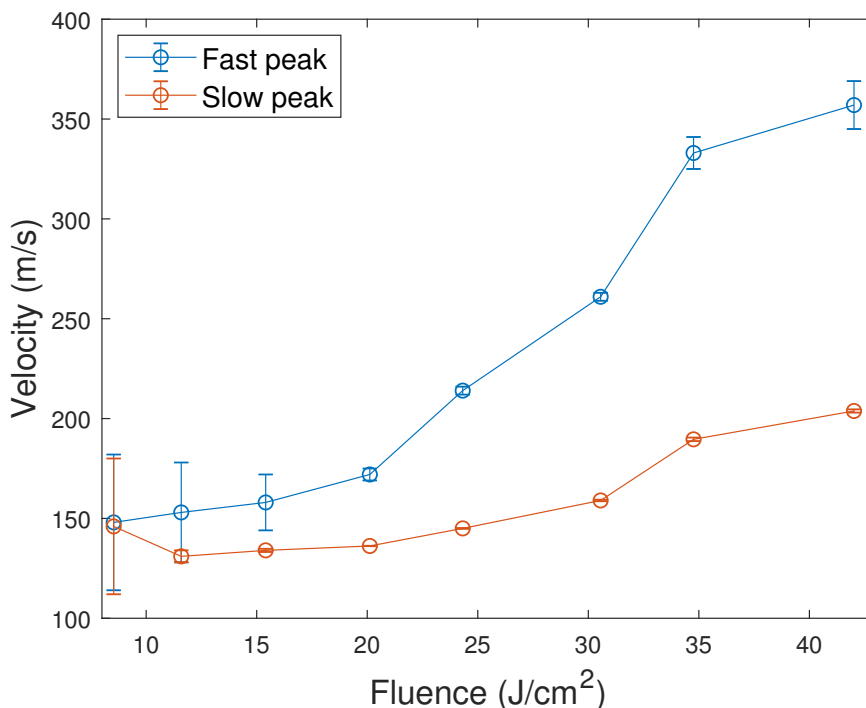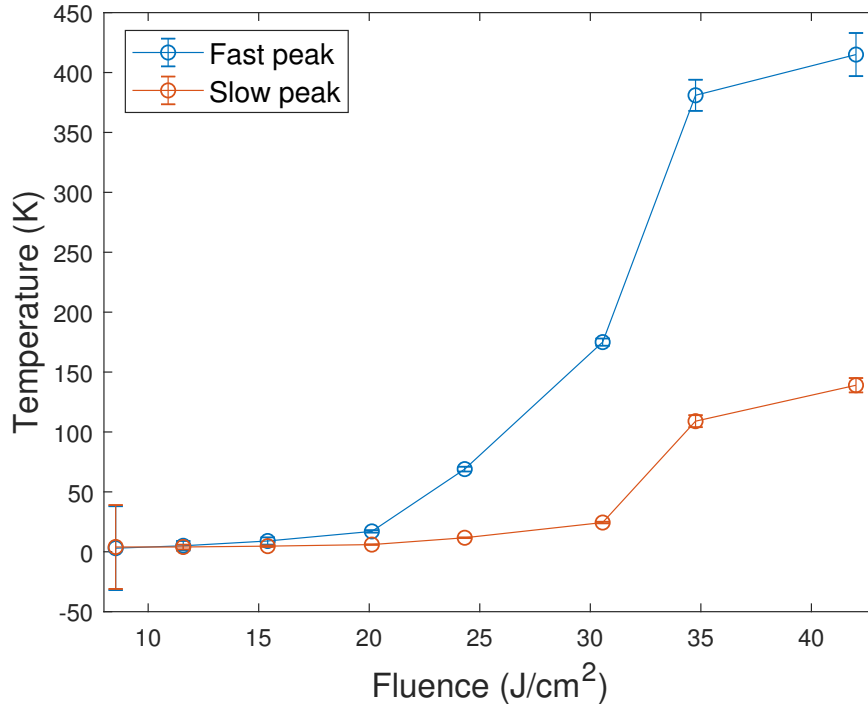

Figure 4.13: Temperatures of both components when fitting the LIF signal to two Maxwell-Boltzmann distributions for the different ablation energies (converted into fluence). At low ablation fluences these values approach one another and ultimately become indistinguishable.

While the fitted parameters describe a general trend as the ablation power is increased, the measured signal does not necessarily look like a Maxwell-Boltzmann distribution, especially at higher ablation powers. This is partly due to the fact that the beam has likely not properly thermalized to the buffer gas, as indicated by the temperatures extracted from the fit. We will look at the topic of thermalization in some more detail now, since this relates back to the scans of the other parameters of our source, namely of the neon flow rate and cell temperature. However, there is another reason why the measured LIF signal does not necessarily look like a Maxwell-Boltzmann distribution, but this is a topic we will discuss in a separate section (4.4).

4.3.2   Thermalization and double peaks

Phase explosion alone is not enough to fully understand the appearance of these double peak structures. As can be seen from the scans (figures 4.4, 4.5, and 4.6), these peaks not only show up for high ablation energies, but also when high neon flow rates and low cell temperatures are used, and they change as those parameters are increased or decreased while the ablation laser energy remains constant. This suggests that these parameters enhance the small effect of phase explosion that occur even below the threshold fluence, or otherwise result in the broadening and eventual splitting of the main peak. The most straightforward interpretation is that the neon flow rate and cell temperature are important factors in the process of thermalization, as expressed in equation 2.15. If this thermalization length is longer than the distance from the ablation spot to the cell exit, the SrF beam will have left the cell before enough collisions have taken place to thermalize to the neon gas. We can examine how the thermalization length changes when the various parameters are scanned and see this relates to the appearance of the double peak structure.
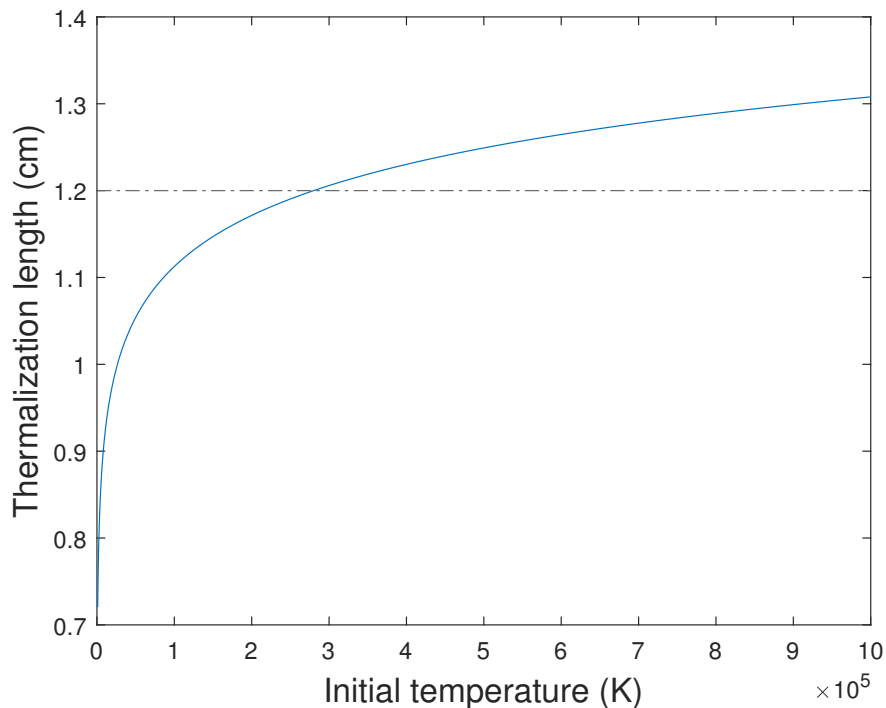
Figure 4.14: The thermalization length (in cm) versus the initial temperature of the molecules as given by equation 2.15, using a flow rate of 9 SCCM and cell temperature of 20 K. The dotted line is the distance available for thermalization (the distance from the target to the cell exit). After an initial temperature of 2.8×10^5 K, this distance is no longer sufficient and the molecular beam will not have thermalized to the buffer gas .

First, we will look at the ablation energy scan. For figures 4.7 and 4.8, the flow rate was 9 SCCM and the cell was kept at a temperature of 20 K. The one parameter that is not fixed, is the initial temperature $T(0)$. This should be related to the ablation energy (fluence) used in

this parameter scan. We can plot the thermalization length versus the initial temperature for these conditions and see when proper thermalization cannot take place before the molecular beam exits the cell. This is shown in figure 4.14, and the critical temperature is 2.8×10^5 K. This means that, above the threshold fluence, the initial temperature of the molecules likely exceeds 2.8×10^5 K, since figure 4.13 shows that the temperature exceeds 20 K (T_b) for fluences above this threshold. From the LIF signal (see appendix) it is also clear that, above this threshold, the signal splits in two, and at lower ablation energies the signal still consists of one peak.

We can now use the extracted temperatures (from the fitting as described in section 4.3.1) to find the initial temperature $T(0)$ of the species for the applied laser fluences. Recall equation 2.12, which describes the temperature after N collisions:

$$\frac{T(N)}{T_b} = 1 + \left(\frac{T(0)}{T_b} - 1 \right) e^{-N\kappa^{-1}} \tag{4.15}$$

Which can be solved for N:

$$N = \kappa \ln \left(\frac{T(0) - T_b}{T(N) - T_b} \right) \tag{4.16}$$

We can combine this with equation 2.15:

$$L = \lambda_s \times N_{\text{thermal}} = \kappa \ln \left(\frac{T(0) - T_b}{T(N) - T_b} \right) \frac{A_{\text{aperture}} \bar{v}_{0,b}}{4 f_{0,b} \sigma_{b-s} \sqrt{1 + m_s/m_b}} \tag{4.17}$$

This new expression now describes the length L needed for the species to cool down from a temperature $T(0)$ to $T(N)$. Using the (highest) temperatures found from the fits as an upper limit on $T(N)$ and the available distance from the target to the cell exit (12 mm) as L, one can now find an estimate (upper limit) for $T(0)$. For the laser fluence used in figures 4.4, 4.5, and 4.6, one finds $T(0) \approx 6.9 \times 10^7$ K.

Figures 4.15, 4.16, and 4.17 show the thermalization length required to thermalize to the buffer gas and how this length depends on the scanned parameters. In the cell temperature and neon flowrate scans the ablation laser energy used was equal, and we have used the aforementioned $T(0)$ as initial temperature in order to obtain these figures. The relation is equivalent to setting $T(N) - T_b = \alpha T_b$ in equation 4.17, where α is 0.01. This means that the length as found from this relation is the length required for the molecular beam to reach the same temperature as the buffer gas within 1%.

From figure 4.15, it is clear that for flow rates exceeding 13 SCCM, the available length of 1.2 cm should be adequate for proper thermalization. In other words, the width of the measured LIF signal should have reached a minimum and should no longer decrease as the flow rate increases. Figure 4.5 shows this to roughly be the case, at least for the fast peak which emerges after a flow rate of about 6 SCCM. The slow peak is not as strong (much lower photon counts), and as a result it is harder to see any changes in the width of this peak as the flow rate increases. The general trend of higher flow rates leading to lower temperatures (and narrower peaks) should be evident from figures 4.4 and 4.5. The difference between the two flow rate scans is that the minimum peak width is reached at higher flow rates when

Figure 4.15: The length required to thermalize the molecular beam to within 1% of the buffer gas temperature T_b, for flow rates ranging from 1 to 40 SCCM. The buffer gas temperature was set to the cell temperature used to acquire figure 4.5, namely 22 K. An estimated starting temperature of 6.9×10^7 K was used. After flow rates of about 13 SCCM the available length of 1.2 cm (dotted line) is adequate.

a higher cell temperature is used. This can be understood by examining equation 4.17 in some more detail.

The relation between the required thermalization length and the neon flow rate can be seen directly from this equation, namely $L_{\text{thermal}} = \propto 1/f_{0,b}$. This can also be seen directly from figure 4.15. Higher flow rates decrease the path length necessary for the SrF molecules to thermalize to the buffer gas. The point where the thermalization length is equal to the available distance of 1.2 cm however does not exactly coincide with the flow rates as seen in figure 4.4 and 4.5. In figure 4.5 this should be around 13 SCCM, while for figure 4.4 this should be around 15 SCCM.

Figure 4.4 shows clearly that the width of the peak, when the double peak structure is absent, still decreases until a flow rate of 40 SCCM. While equation 4.17 is not exact, it should be accurate to within an order of unity [27], so clearly one or more of the parameters used do not reflect reality within this accuracy. The flow rates, masses, and fundamental constants involved can all be assumed to be accurate to this level. The masses and constants are known to great accuracy and their values were used up to at least 4 significant digits in the calculations leading to figures 4.15 and 4.17. The flow rates are set and controlled using a flow controller (EL-FLOW prestige from Bronkhorst, with a specified accuracy of 0.5%), which can safely be assumed to be accurate in the flow regimes employed in this experiment.
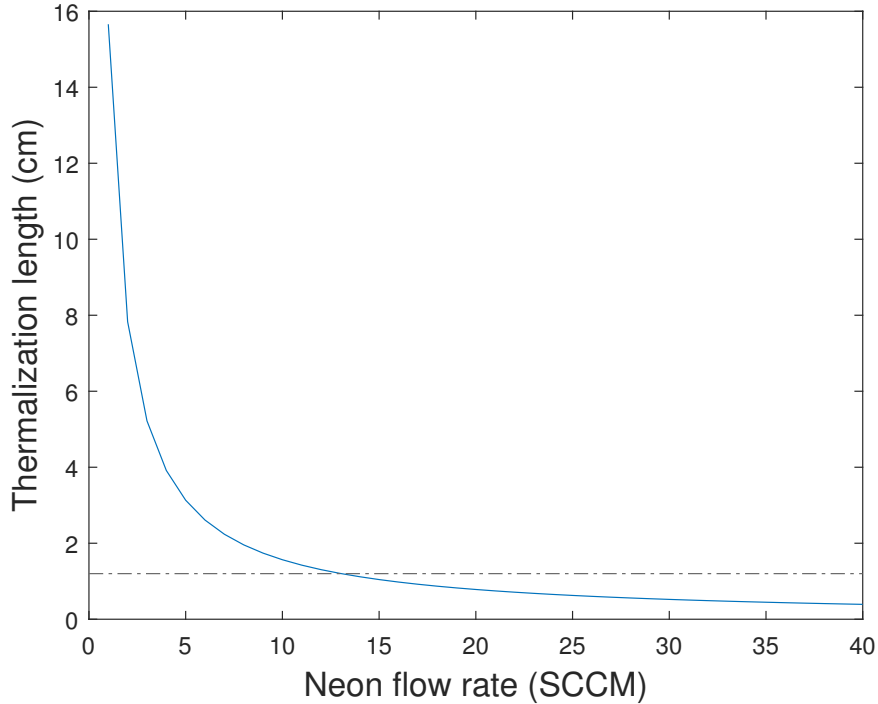
Figure 4.16: Similar to figure 4.16, the length required to thermalize the molecular beam to within 1% of the buffer gas temperature T_b is shown, for flow rates ranging from 1 to 40 SCCM. The buffer gas temperature was set to the cell temperature used to acquire figure 4.5, namely 28 K. An estimated starting temperature of 6.9×10^7 K was used. After flow rates of about 15 SCCM the available length of 1.2 cm (dotted line) is adequate.

A possible point of contention is σ_{b-s}, but since there is no data on its exact value this would have to be determined in a separate experiment. As mentioned in chapter 2 though, others have found this cross section to be rather similar using different buffer gas atoms and species molecules. What is less well-known, is the exact value of $T(0)$ and T_b (and by extension $\bar{v}_{0,b}$). We have derived an estimate using the final temperature of one of the double peaks as measured using the same ablation energy, which might not reflect the actual temperature. This initial temperature is the main factor in determining how many collision are needed, and as a result in finding the thermalization length. Throughout this discussion, we have also assumed that the buffer gas temperature was equal to the cell temperature, since the inlet is in direct thermal contact with the cell and a heating element is used to prevent the neon from freezing inside the supply line. It is possible though, that due to the high ablation energy and repetition rate of 10 Hz the buffer gas is heated and its temperature is in fact higher than the cell temperature. Both a higher initial temperature and a higher buffer gas temperature would lead to a higher flow rate at which the thermalization length reaches 1.2 cm.

The dependence of the thermalization length on the buffer gas temperature (cell temperature) is less evident. The temperature T_b is implicit in both the number of collisions needed N_{thermal} and the mean thermal velocity $\bar{v}_{0,b}$, which in turn influences the number
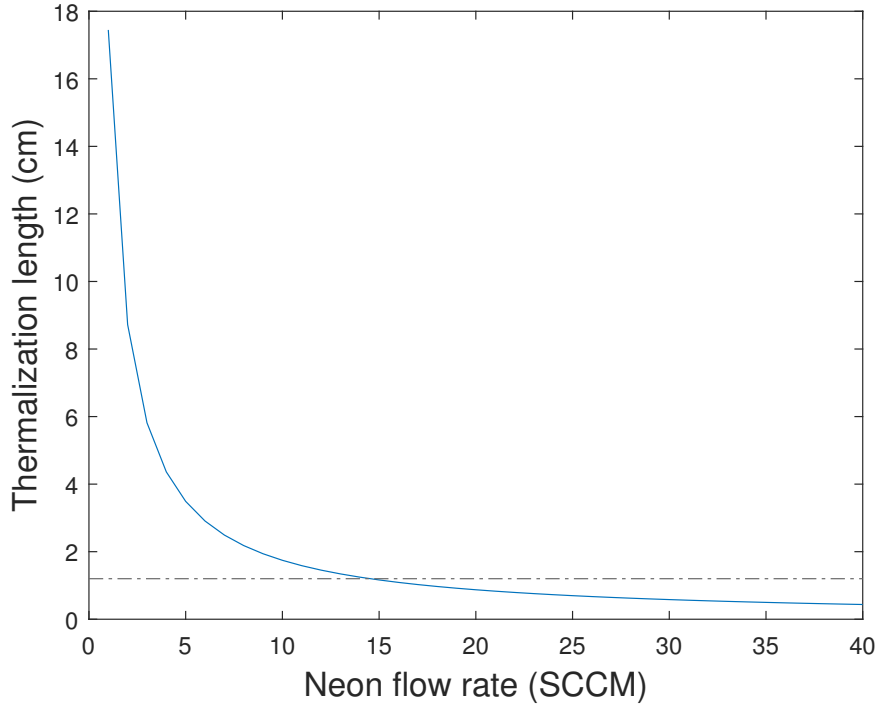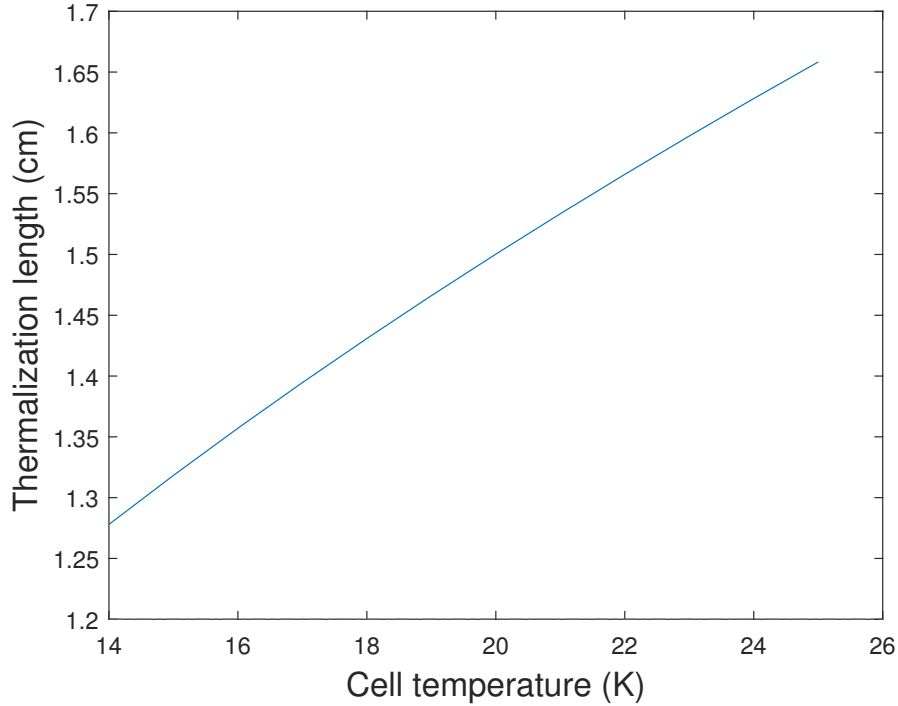
Figure 4.17: The length required to thermalize the molecular beam to within 1% of the buffer gas temperature T_b, for cell temperatures ranging from 14 to 25 SCCM. The neon flow rate was set to 10 SCCM, the same conditions used to acquire figure 4.6. An estimated starting temperature of 6.9×10^7 K was used. The available length of 1.2 cm is not reached in this temperature range.

density and mean free path inside the cell, as discussed in chapter 2. While $\bar{v}_{0,b} \propto \sqrt{T_b}$, N_{thermal} depends on the difference between the initial temperature and the final temperature of the SrF molecules, more specifically their (natural) logarithm. Since $T(0)$ is rather high compared to T_b, a change of a few degrees K in T_b will have only a small effect on N_{thermal}, and as a result the dominant factor in the expression for the thermalization length is $\bar{v}_{0,b}$, such that $L_{\text{thermal}} \propto \sqrt{T_b}$. As seen in figure 4.17, a higher cell temperature leads to a longer thermalization length. The scan of the cell temperature as seen in figure 4.6 also shows that both peaks keep getting narrower (thermalization improves) as the cell temperature drops, before no signal is seen after 15 K.

In the scans of the cell temperature, the double peak structure emerged as the cell temperature was lowered, and from the above discussion on the relation between this parameter and thermalization it is clear that this results in a shorter thermalization length. In other words, the temperature of the molecular beam is lowered as well, and the peaks in the LIF signal get more narrow. This can in fact be seen in figure 4.6, which starts out with a very wide distribution of arrival times at 25 K, and at lower temperatures the double peak structure appears. This suggests that, at the higher temperatures where only a single, albeit very broad peak can be seen, this single peak actually consists of two peaks. The high temperature broadens these peaks so much that they appear as one, but as thermalization

improves, the two components become more defined. The flow rate scans follow the same reasoning, the difference being that higher flow rates result in better thermalization, and as a result a more well-defined double peak structure. The flow rate scan at a cell temperature of 28 K is at such a high cell temperature though, that even at the highest flow rates this double peak structure does not appear.

4.3.3 Conclusions

To conclude this section on the double peak structure, we have hypothesized phase explosion to be the cause of this phenomenon. Consistent with this hypothesis is a significant increase in molecular signal after a threshold fluence (ablation energy per area, in J/cm^2) is crossed, which we have observed to take place at a fluence of about 22 ± 2 J/cm^2 when using a SrF_2 (salt) target to produce SrF molecules. Above this fluence, phase explosion seems to be the dominant ablation process and the molecular signal visibly splits into two peaks. We have extracted the associated velocity and temperatures of these peaks by assuming that their TOF profiles take on the form of bimodal Maxwell-Boltzmann distributions. This analysis has shown that, for lower fluences (below the threshold), these two peaks become indistinguishable from one another. Following a discussion about the process of thermalization, we have seen that conditions which lead to lower temperatures in the molecular beam (higher flow rate, lower cell temperature) reveal the double peak structure when it was otherwise obscured due to both peaks overlapping and forming a single peak.

While the exact behavior of the fast and slow peaks as the various parameters (flow rate, cell temperature, and ablation laser fluence)are scanned has not been quantified, it should be clear that this effect only becomes noticeable when the target is ablated using a fluence which exceeds the threshold value. Since this value depends on the target itself and how it was made, future studies will have to investigate this threshold value on a target-by-target basis. As we have seen in section 4.1 though, a relatively low laser fluence (8.5 J/cm^2) combined with a Sr metal target can yield the required number of SrF molecules, so a more detailed understanding of the double peak phenomenon might not be necessary.

One particular set of parameters (SrF_2 target, fluence of 24 J/cm^2, neon flow rate of 9 SCCM, and a cell temperature of 20 K) suggest that a significant fraction of the molecules is part of the slow peak, which could be exploited when the source is combined with the decelerator. Since a lower initial velocity would require a weaker deceleration strength (which would in turn mean less losses inside the decelerator), this could lead to a higher number of successfully decelerated SrF molecules. It might be worthwhile to explore this set of parameters once the source and the decelerator have been combined.

4.4 Interpretation of TOF profiles as velocity distributions

Until now, we have interpreted the LIF and absorption signals separately. The absorption signal has been used to evaluate the number of molecules, while the LIF signal has been used to characterize the beam as the various parameters were scanned. Since the absorption probe beam is so close to the cell exit (5 mm), the measured absorption signal can be interpreted as a spatial distribution of the beam, since there has not been enough distance for the velocity components to spread the beam out yet. After 30 cm though, where the LIF detection takes place, the different velocities present in the beam have shaped the beam primarily, and as a result the TOF profiles found here can be interpreted as velocity distributions.
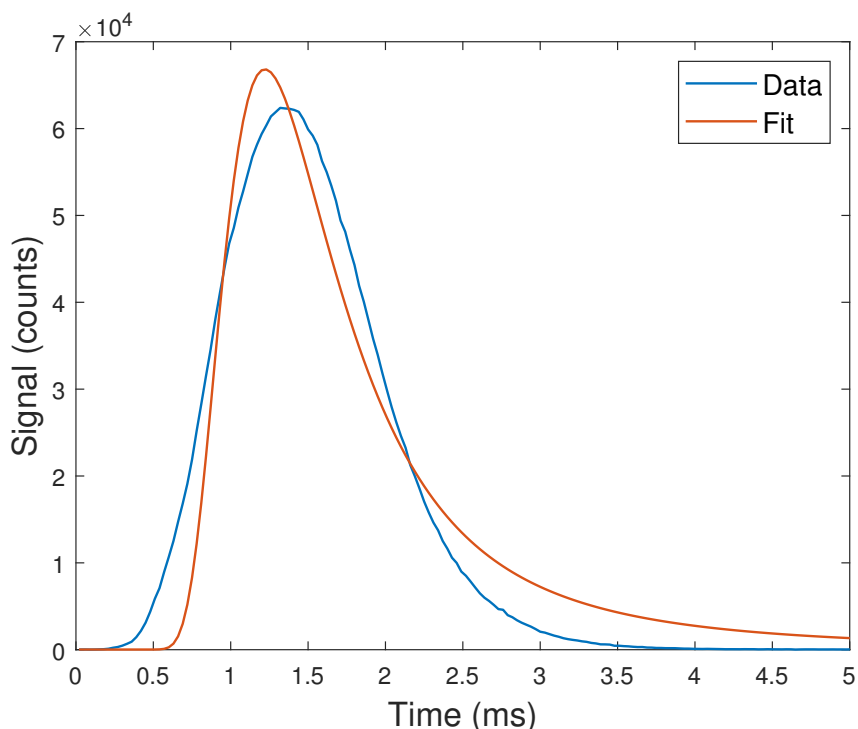
Figure 4.18: A fit of the LIF signal to a Maxwell-Boltzmann distribution. The fitting procedure found $v_0 = 200 \pm 2$ m/s and $T = 91 \pm 2$ K. Experimental conditions from figure 4.3 apply here as well.

The exact translation of these TOF profiles into a concrete velocity distribution (ideally a Maxwell-Boltzmann distribution) is unfortunately not as straightforward as converting the arrival times into velocities using the relation $v = L/t$, where L is the distance traveled by the molecules from the point of production to the LIF detection beam. This relation is reasonably accurate if the arrival times are far greater than the duration of the pulse [50]. In this source though, the arrival times fall roughly in the range between 0.5 and 3 ms, and the pulsewidth is about 0.5 ms. Reference [50] claims a shorter pulsewidth of 275 μs, which they ascribe to the small cell volume and low extraction time. Since our LIF detection is

relatively close (30 cm) to the exit compared to the aforementioned setup (130 cm), the resulting arrival times are much shorter, becoming comparable to the pulse width.

The linear relation of $v = L/t$ need not apply, since the molecules first have to exit the cell, and in this time their path towards the exit is not necessarily the shortest and due to collisions inside the cell their velocity changes drastically. The finite pulse width itself also complicates this. The molecules at the front of the pulse would reach the detection stage earlier than those in the back, if they all had the same forward velocity. However, this need not be the case. In fact, if proper thermalization has occurred inside the cell, the velocity distribution of the molecular beam can be described as a Maxwell-Boltzmann distribution. The resulting TOF profiles will thus differ from a pure Maxwell-Boltzmann distribution due to this finite pulse width and the extraction process. To illustrate this point, figure 4.18 shows a direct fit of a LIF signal to a Maxwell-Boltzmann distribution. The associated parameters of interest are $v_0 = 198 \pm 2$ m/s and $T = 90 \pm 2$ K. From this figure it is clear that a pure Maxwell-Boltzmann distribution does not accurately describe the measured LIF signal.

In the following discussion we will use the LIF and absorption signals from figures 4.2 and 4.3 (and as a result, a Sr metal target) to build up a general framework to examine this issue of interpreting both signals. It stands to reason that one can apply the same analysis in comparable contexts, as long as one has both an absorption signal (measured close to the exit) and a LIF signal (measured farther away from the exit).

4.4.1   An analytic approach

In supersonic beams, the pulses are created by opening and closing a valve. The measured TOF profile in this case has been described as a convolution of a Maxwell-Boltzmann distribution and the pulse shape [51]. The valve has a certain, finite opening time τ, and the pulse shape can be approximated as:

$$q(t) = \begin{cases} A & 0 \leq t \leq \tau \\ 0 & \text{otherwise.} \end{cases} \tag{4.18}$$

For some arbitrary amplitude A. The Maxwell-Boltzmann distribution in the time domain takes the form of:

$$p(t) \propto \left(\frac{L}{t}\right)^2 \exp\left(-\frac{(L/t - v_0)^2}{2k_b T}\right) \tag{4.19}$$

Where v_0 is the mean forward velocity of the beam and T its translational temperature. The convolution of both the pulse shape and this Maxwell-Boltzmann distribution is given by:

$$P(t) \propto \int_{-\infty}^{\infty} q(t')p(t - t')dt' \tag{4.20}$$

Which has been solved analytically [51] and takes the form of:

$$P(t) \propto erf(Z_1) - erf(Z_2) \tag{4.21}$$

Where erf is the error function, and its parameters Z_1 and Z_2 are given by:

$$Z_1 = \frac{L}{\alpha_s(t-\tau)} - \frac{v_0}{\alpha_s} \tag{4.22}$$

$$Z_1 = \frac{L}{\alpha_s t} - \frac{v_0}{\alpha_s} \tag{4.23}$$

Where in turn $\alpha_s = \sqrt{2k_b T/m}$.

Figure 4.19: The effect of τ on a TOF profile, assuming the true velocity distribution to be a Maxwell-Boltzmann distribution, given by equations 4.18, 4.19, and 4.21. In this example, $L = 0.75$ m, $v_0 = 558$ m/s, and $\alpha = 30$ m/s. For increasing values of τ, the TOF profile is deformed from the Maxwell-Boltzmann distribution (pure MB) and resembles the pulse shape as described by equation 4.18 more and more. Adapted from [51].

The general behavior of this expression is that for low values of τ, the ideal Maxwell-Boltzmann distribution is only slightly altered, while for increasing values of of τ, the TOF profile will be shaped more and more like the pulse shape function. Generally, the width of the resulting TOF profile will be similar to the characteristic valve operation time τ. The effect of τ is illustrated in figures 4.19 and 4.20, where figure 4.19 shows the general trend of an increasing τ while figure 4.20 shows the effect using parameter values more comparable to our setup, which is similar but not as extreme as in figure 4.19.

Our cryogenic source however does not use such a valve, and the resulting pulse depends more on the ablation and extraction process, which are much harder to control and describe in detail. As a result, equation 4.18 does not accurately describe the pulse in our case. To
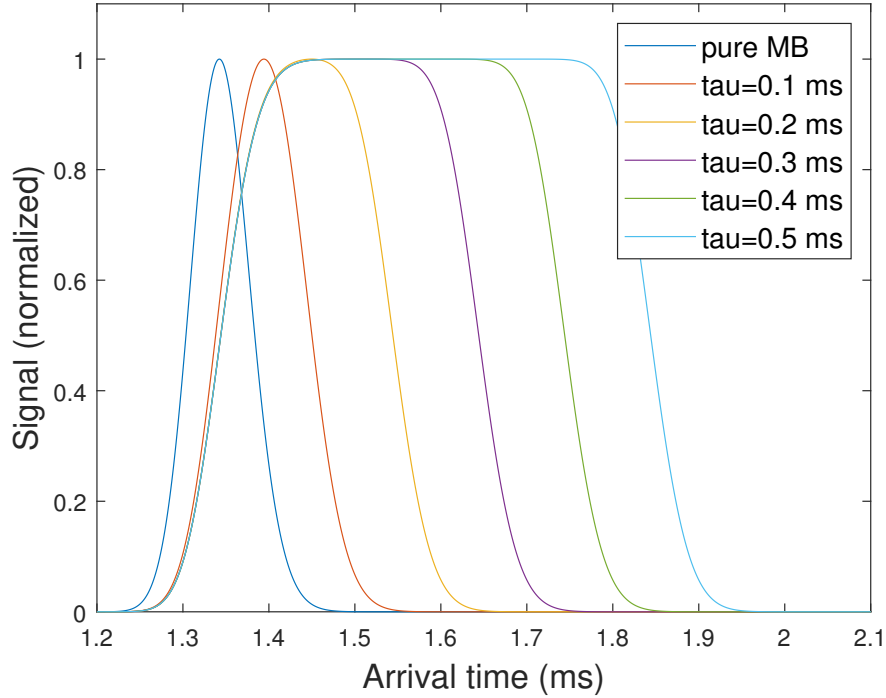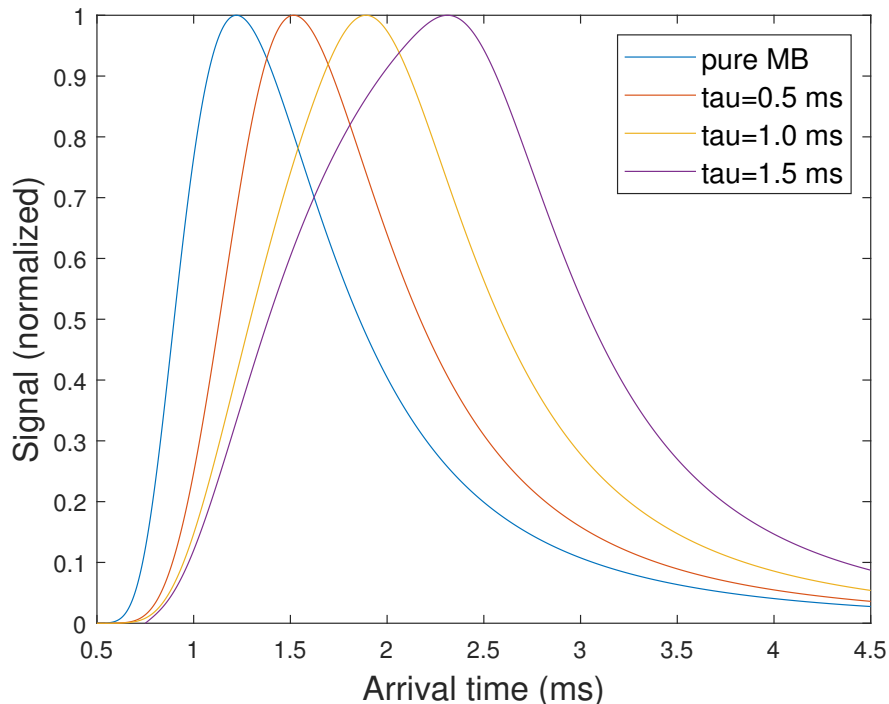
Figure 4.20: The effect of τ on a TOF profile, assuming the true velocity distribution to be a Maxwell-Boltzmann distribution (pure MB), given by equations 4.18, 4.19, and 4.21. In this example, the parameters are comparable to the situation in our cryogenic source, namely $L = 0.312$ m, and using the parameters found by fitting the LIF signal to a Maxwell-Boltzmann distribution ($v_0 = 200$ m/s, $T = 91$ K). Unlike in figure 4.19, the signal is spread out and its maximum shifted to later arrival times for increasing values of τ. The general effect is that, for a measured TOF profile, the true distribution peaks at a much earlier time, and thus v_0 is larger than L/t_{peak}.

illustrate this, figure 4.21 shows a fit to this analytic expression, and clearly the fit does not resemble the measured LIF signal. In addition, the found parameters $v_0 = 276 \pm 2$ m/s, $T = 202 \pm 5$ K, and $\tau = 0.719 \pm 0.007$ ms are not realistic in this case. While the pulse width of $\tau = 0.719 \pm 0.007$ is reasonable, considering the absorption signal in figure 4.2, the same can not be said of the temperature and velocity. In chapter 2, we have found an upper limit on the mean forward velocity of 240 m/s, under the condition that the beam has properly thermalized to the buffer gas. Given that, under these experimental conditions, the thermalization length is smaller than the available distance from the target to the cell exit (at most 1.1 cm if $T(0) = 2.8 \times 10^5$ K), this should certainly be the case, and as a result the temperature should also have approached 17 K. Thus we conclude that the approach outlined in [51] cannot be applied directly in the context of a cryogenic source and we will have to start from a more general framework.
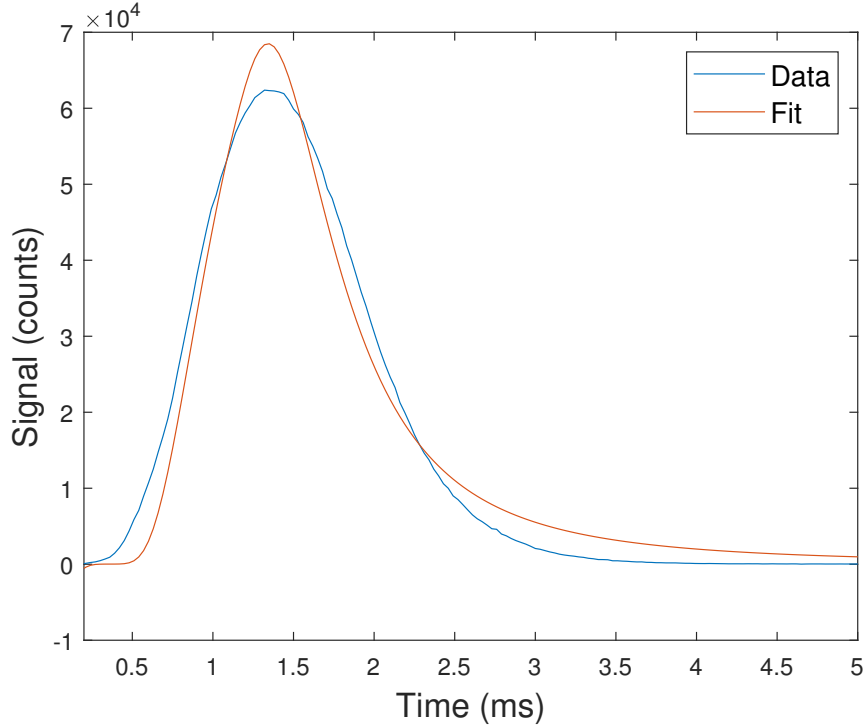
Figure 4.21: A fit of the analytic expression given by equation 4.21 to the measured LIF signal. The fit finds $v_0 = 276 \pm 2$ m/s, $T = 202 \pm 5$ K, and $\tau = 0.719 \pm 0.007$ ms.

4.4.2 General framework and analysis

In general, the measured TOF profile $g(t)$ can be expressed as [52]:

$$g(t) = \int_0^t h(t)f(t - \tau)d\tau = \int_0^t h(t - \tau)f(t)d\tau \tag{4.24}$$

Where $f(t)$ is the pure TOF profile and $h(t)$ the response function, which describes the overall dynamic response of the system. If the molecular beam has properly thermalized to the buffer gas, $f(t)$ is simply a Maxwell-Boltzmann distribution with a characteristic v_0 and T. Assuming that the pulse length is the dominant factor distorting this pure TOF profile, $h(t)$ describes the pulse shape, similar to equation 4.18.

Deconvolution is the process of inverting expression 4.24 to extract either $h(t)$ or $f(t)$ from a measured TOF profile $g(t)$, using an estimate of either $f(t)$ or $h(t)$ respectively. While in the time domain, inverting this equation seems highly nontrivial, this process is made considerably easier in the frequency domain due to the convolution theorem. If we define the Fourier transform $F(\omega)$ of some function $f(t)$ as:

$$F(\omega) = \int_{-\infty}^{\infty} f(t)e^{2\pi i\omega t}dt \tag{4.25}$$

And the inverse Fourier transform as:

$$f(t) = \int_{-\infty}^{\infty} F(\omega)e^{-2\pi i\omega t}d\omega \tag{4.26}$$

64

The convolution theorem states that [52]:

$$G(\omega) = H(\omega)F(\omega) \tag{4.27}$$

Thus one can extract for example $F(\omega)$ using:

$$F(\omega) = \frac{G(\omega)}{H(\omega)} \tag{4.28}$$

And from $F(\omega)$ extract $f(t)$ by taking its inverse Fourier transform. The generality of this description means that one can extract either $f(t)$ or $h(t)$ from $g(t)$, as long as a reasonable estimate can be made of the other function. Fast Fourier transform algorithms can provide a computational route to perform these operations and deconvolve a signal.
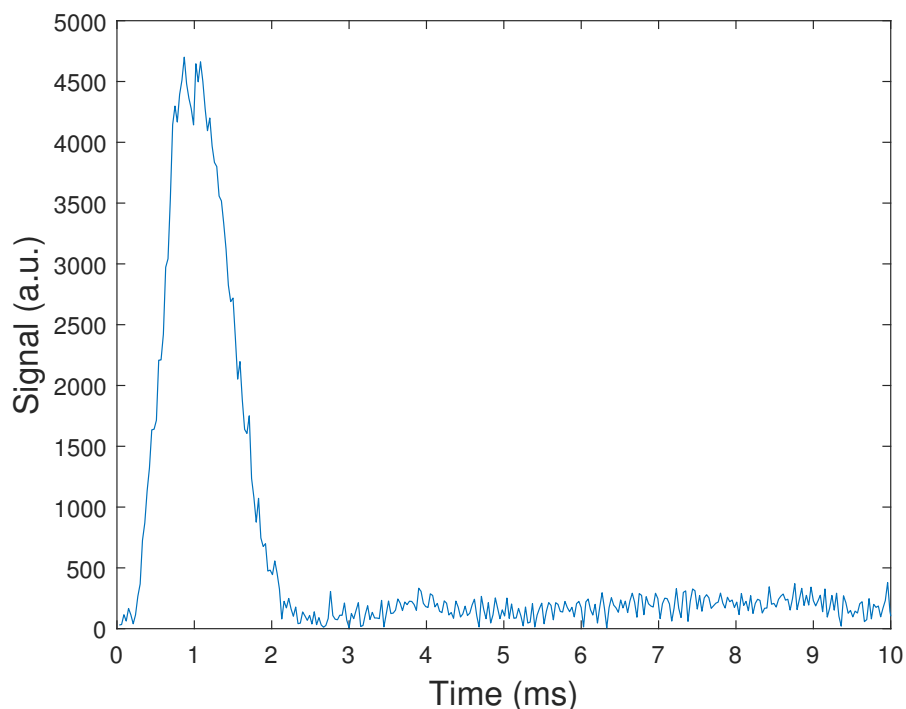
Figure 4.22: Deconvolved signal, achieved without Wiener filtering by applying (inverse) Fourier transforms and using equation 4.28. The resulting signal should resemble $f(t)$, the true TOF profile. The results of the procedure depend on the quality of the estimate of $h(t)$, in this case given by the absorption signal.

Since the procedure involves taking the Fourier transform of a signal twice (first from the time domain to the frequency domain and then the inverse to finally obtain the desired deconvolved signal), noise is greatly amplified and the presence of zeros in $H(\omega)$ can result in a poorly deconvolved signal. The use of filters can suppress these effects, mostly by filtering out high-frequency noise, but they often introduce their own problems in the form of ringing [52]. The appearance of zeros in $H(\omega)$ can be be circumvented by implementing Wiener filtering as described in [52], where 4.28 takes the form of:

$$F(\omega) \approx G(\omega)\hat{W}(\omega) \tag{4.29}$$

Where, for an estimated $\hat{h}(t)$ and its resulting Fourier transform $\hat{H}(t)$:

$$\hat{W}(\omega) = \frac{\hat{H}^*(\omega)}{|\hat{H}(\omega)|^2 + \phi} \tag{4.30}$$

Here $\hat{H}^*(\omega)$ is the complex conjugate of $\hat{H}(\omega)$ and $|\hat{H}(\omega)|$ its modulus. The parameter ϕ is roughly equal to the noise-to-signal ratio, but an ideal value can be found through trail and error [52]. If ϕ is too large, its effect will dominate $\hat{W}(\omega)$ and the deconvolution will be of poor quality, but when it is too small, $\hat{W}(\omega)$ will diverge for small values of $|\hat{H}(\omega)|$. A typical starting guess for ϕ is a fraction 10^{-6} of the maximum measured signal, after which one would investigate the effect of lowering and increasing its value until the deconvolved signal is as clean as possible. By combining fast Fourier transform algorithms, Wiener filtering, and the measured TOF profiles, we can now use the procedure developed in this section to extract either $g(t)$ or $h(t)$.
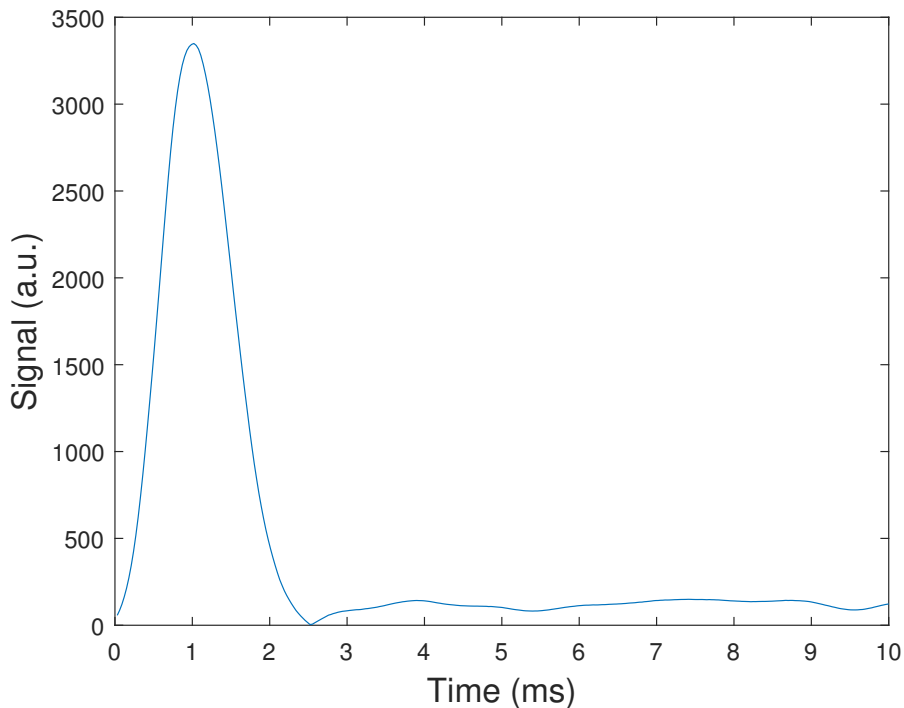
Figure 4.23: Deconvolved signal, achieved using Wiener filtering as described by equations 4.29 and 4.30. The absorption signal was used as an estimate of the response function $h(t)$. Through trial and error, it was found that taking ϕ to be 10^{-3} of the maximum measured LIF signal resulted in the cleanest signal.

We can extract $f(t)$ by using the absorption signal as an estimate for the response function $h(t)$, since it contains information on the spatial spread of the molecular beam pulse. The deconvolved signal should then resemble a Maxwell-Boltzmann distribution (assuming proper thermalization). This signal can then be compared to a fit of the TOF profile, which could indicate how accurate such a fit is and if the extracted velocity and temperature are reliable.

If this shows that the TOF profile is only minimally distorted due to the finite molecular pulse length, the TOF profile could be sufficiently analyzed and characterized by directly fitting the measured LIF signal to a Maxwell-Boltzmann distribution and the extracted v_0 and T would accurately describe the molecular beam as a result.

First we turn the absorption signal as seen in figure 4.2 into an estimate for the pulse shape function, similar to equation 4.18. This is done by flipping the signal and then normalizing it, such that the maximum is 1, while the background has a mean value of zero. Since the signal is rather noisy, this will inevitably lead to more noise as we use the devonvolution procedure we have just developed. The Wiener filtering will clear the signal up somewhat though, as we will see.

If we try to extract $f(t)$ from the measured LIF signal $g(t)$ using the estimated response function we have just described as $h(t)$, Fourier transforms, and equation 4.28, the deconvolved signal can be seen in figure 4.22. Here we have not used Wiener filtering. Using Wiener filtering, as described by equations 4.29 and 4.30, the rather noisy deconvolved signal of figure 4.22 turns into the signal depicted in figure 4.23. Through trial and error it was found that taking ϕ to be 10^{-3} of the maximum measured LIF signal resulted in the cleanest signal. Figure 4.24 shows both this (Wiener filtered) deconvolved signal and the measured LIF signal, which are both similar in shape. The main difference seems to be that one signal is shifted in time with respect to the other, with the difference in time being about 0.4 ms.
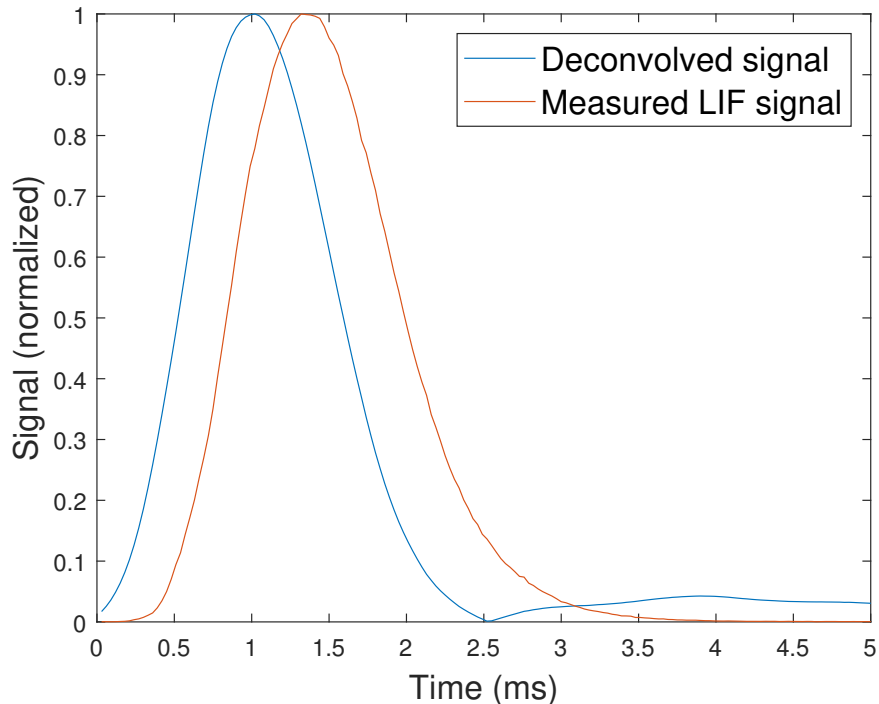
Figure 4.24: The deconvolved signal (using Wiener filtering) and the measured LIF signal on the same timescale. Both signals resemble one another, but one appears to be shifted with respect to the other.

We can understand this shift by considering more carefully what we have used as input in the deconvolution process. Most importantly, the use of the absorption signal as an estimate for the response function $h(t)$, which originates from an absorption measurement at a distance of 5 mm from the cell exit. In our discussion on the analytic case (using a supersonic source [51]), the pulse shape function described the molecular pulse from the moment of ablation. However, our absorption signal tells us what the pulse looks like after extraction from the cell. Assuming the shape of the pulse does not change significantly from the time of production to the absorption measurement, the absorption signal is still a useful estimate of the response function $h(t)$ if we correct for the time it takes for the pulse to reach the absorption probe laser beam. Part of this correction is the extraction time, or pumpout time, as defined in chapter 2 by equation 2.20:

$$\tau_{\text{pump}} = \frac{4V_{\text{cell}}}{A_{\text{aperture}}\bar{v}_{0,b}} \tag{4.31}$$

Using a flow rate of 9 SCCM and a cell temperature of 17 K, this pumpout time is $\tau_{\text{pump}} = 0.68$ ms. The result of correcting for this pumpout time (and the time to travel the 5 mm from the cell exit to absorption) and fitting this time-shifted deconvolved signal to a Maxwell-Boltzmann distribution can be seen in figure 4.25. The fit found $v_0 = 150.4 \pm 0.4$ m/s and $T = 15.7 \pm 0.3$ K.
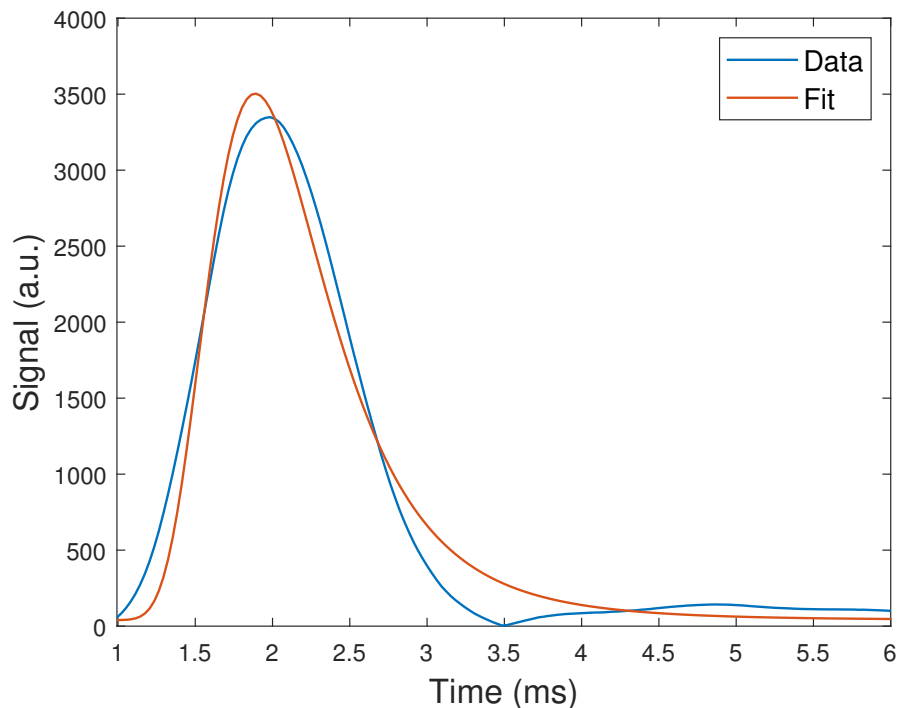
Figure 4.25: Fit of the deconvolved and time-shifted signal to a Maxwell-Boltzmann distribution. The fit found $v_0 = 150.4 \pm 0.4$ m/s and $T = 15.7 \pm 0.3$ K.

Comparing figure 4.18 and 4.25, we can conclude that both the temperature and velocity as extracted from the raw LIF signal is much larger than what is more likely the actual value of these parameters of the beam. While the fit in figure 4.25 seems more accurate than figure 4.18, it is far from perfect. Both the extracted temperature and velocity seem too low. The temperature of $T = 15.7 \pm 0.3$ K is actually lower than the temperature of the cell (17 K), which is not realistic if we assume that the buffer gas also has a temperature of 17 K, since it would mean that the beam has been cooled beyond the temperature of the buffer gas. As for the velocity, these experimental conditions translate into a Reynolds number of 97, and an expected forward velocity of 177 m/s.

One explanation for this discrepancy would be that the temperature of the buffer gas is actually much lower than the 17 K of the cell. This is possible, given that the cold stage of the cryocooler is kept at 4 K, but difficult to check. While the neon line is fed into the cell through this cold stage, it is also heated as it enters the cell. There is also the issue that at lower temperatures, the neon will simply freeze to the walls of the cell or block the neon line completely, which would stop the source from producing a beam, and this is clearly not the case here.

A more likely explanation is that the beam has actually properly thermalized to the buffer gas, but the extracted true TOF profile is inaccurate, since it clearly does not follow the shape of a Maxwell-Boltzmann distribution. A few factors come into play here:

- The correction in time to account for the fact that the absorption measurement takes place 5 mm after the cell exit. Its value has a significant effect on the fit parameters, ranging from $v_0 \approx 242$ m/s and $T \approx 283$ for no shift to the aforementioned $v_0 = 150.4 \pm 0.4$ m/s and $T = 15.7 \pm 0.3$ K for a (total) shift of 0.96 ms. In the preceding analysis, this shift was arrived at by extrapolating the pumpout time, assuming the mean velocity of the beam in its travel from the target to the cell exit to be the same as from the cell exit to the absorption detection region. This need not be the case, and in fact the pumpout time itself is only a rough estimate, so this exact timeshift is hard to define rigorously.

- The absorption signal itself. This signal is quite noisy (fluctuations of about 10% of the maximum signal) and has a feature at the start where the signal first dips into positive values before the absorption signal starts to appear. This is likely caused by the triggering and the electronics but will have to be investigated further, together with improving the signal-to-noise ratio. Since the absorption takes place 5 mm after the cell exit, the signal is rather short compared to the entire repetition time of 0.1 s, and as a result the absorption peak might be undersampled. By increasing the resolution in timestamps this peak might be better resolved.

- The validity of using the absorption signal as an estimate of the response function. The absorption signal might not be a good estimate for the spatial distribution of the beam. Additionally, perhaps the pulse shape is not the dominant factor in the response function. In principle, this function includes not only the effect of the pulse shape, but also the electronics and many other things specific to the experimental setup and conditions used, which most of the time are either unknown or lack a(n) (analytic) mathematical description [52]. A more complete description will have to somehow take

into account the many possible paths which the molecules can take inside the cell before their extraction. It is beyond the scope of this thesis to develop such a description, but this would likely require the simulation of the flow and trajectories inside the cell instead of the more general description given in chapter 2 and the equations found there.

4.4.3 Conclusions

To conclude this analysis of the effect of the finite pulse width of a pulsed molecular beam from a cryogenic source on the TOF profile as measured using LIF, there are still open questions and the process is not entirely understood for now. While directly translating the arrival times into velocities using $v = L/t$ is not exact due to the many possible paths the molecules might take to reach the detection area and this finite pulse width, it can be used to qualitatively describe the velocity and temperature of the beam as has been done in section 4.2.

The deconvolution of the LIF signal using the absorption signal and the preceding (conceptual) discussion has shown that the pulse width has a significant effect on the TOF profile, mostly by broadening the signal. While this effect has not been quantified yet, the framework has been developed in this section. The main challenge at this point is in finding an accurate estimate of the response function of the system and its experimental conditions, since the analysis presented here has shown that the absorption signal is probably not a sufficient estimate.

Once the source has been coupled to the decelerator, different guiding velocities can be examined in order to find the mean velocity of the molecular beam using certain experimental parameters; the guiding velocity which results in the largest amount of signal at the end of the decelerator would be the mean velocity of the beam using those conditions. If this velocity agrees with the velocity as obtained from the direct fitting of the LIF signal to a Maxwell-Boltzmann distribution (figure 4.18), then clearly this fitting procedure leads to a reliable estimate of the forward velocity of the beam. Due to the broadening effect of the pulse width, the temperature as found from the same fit should be treated as an upper limit though, and depending on the quality of the thermalization process the actual temperature will be lower, approaching T_b as thermalization improves.

Chapter 5

Summary and outlook

5.1 Summary

The Standard Model (SM) of particle physics, despite being proven right time and time again over the past decades, still has some inherent problems. Various extensions to the SM address these shortcomings, but they often introduce new, extremely heavy particles which tend to be just out of reach to be detected by particle accelerators like the LHC. Complementary to these high energy experiments, the field of precision measurements offers a different approach to find answers to the same questions. Of particular interest is the value of the electric dipole moment of the electron (eEDM), which is predicted by the SM to be extremely small while some of these extensions predict its value to be a few orders of magnitude away from the currently achieved experimental precision. For this reason, the NL-eEDM collaboration aims to measure the eEDM with a previously unachieved precision, using a molecular beam of BaF. The project consists of many (sub)components, and in this thesis the production method has been the main topic. A cryogenic buffer gas beam source, or simply "cryogenic source", provides the molecular beam needed in the experiment. Such a source is an essential component to ensure that, from the production of the beam, the final statistical uncertainty in the eEDM measurement can be as low as possible. The context and motivation behind the use of a cryogenic source have been discussed in the introduction (chapter 1) to this thesis.

In order to understand the working principles of such a source and get an idea of what to expect in an experimental setting, the relevant theoretical background has been discussed in chapter 2. Topics like the flow through the cell, the process of thermalization, and extraction from the cell have been described and some parameters which characterize these processes have been defined, along with estimates of these parameters from experimental variables such as the cell geometry, cell temperature, flow rate, and the masses of both the buffer gas atoms and the molecular species of interest. From these descriptions, some properties of the resulting molecular beam have emerged, mostly pertaining to the distribution of the molecules in phase-space. To conclude the theoretical discussion, various methods of phase-space matching have been described, as well as their relevance to the NL-eEDM project. In particular, an electrostatic guide is currently being designed in order to focus the molecular beam into the acceptance of the decelerator. Additionally, there is the possibility of using a

71

de Laval nozzle to achieve a similar effect, but this option is not actively being pursued at this time.

Chapter 3 went into some detail on the design of the source built at the VSI in Groningen, which has been the topic of this thesis. The detection methods used to characterize the molecular beam were addressed, as well as the laser system which stabilizes the detection laser. The method of stabilization has been described, and shown to stabilize the detection laser to 1.5 MHz.

Chapter 4 attempted to describe the molecular beam produced by the cryogenic source in a general sense. First, the number of SrF molecules was estimated using both laser-induced fluorescence (LIF) and absorption detection methods. From the absorption signal, an estimate of 5.5×10^9 molecules per shot was made, which is comparable to the required number as mentioned in the proposal for the NL-eEDM project. An argument was put forth to claim that a switch from producing SrF to BaF molecules would lead to at least a comparable or even higher number of extracted molecules under similar conditions. From the LIF signal, an estimate of 2.3×10^8 molecules per shot was made. The reduced number of molecules (factor of 24) as detected by LIF detection is mostly due to the fact that this measurement took place 30 cm after the cell exit, compared to 5 mm in the case of absorption. Since the probe beam diameter was equal to the diameter of the rings of the decelerator and this measurement took place at a distance comparable to where the decelerator is planned to start, this difference provides an estimate of the losses one could expect if no phase-space matching takes place.

Next, the effect of the neon flow rate, cell temperature, and ablation laser energy on the LIF time-of-flight (TOF) profiles was shown. In order to qualitatively describe the behavior, the TOF profiles were interpreted as being roughly related to the velocity distribution of the beam using $v = L/t$, where L is the distance from the ablation spot to the detection region, which was 312 mm. The general trend observed was that; high flow rates resulted in faster beams, higher signals, and narrower peaks (lower temperatures); higher cell temperatures resulted in slower beams, higher signals, and higher temperatures; higher ablation energies resulted in faster beams with higher temperatures and more molecular signal. These general trends were expected and explained using the theory discussed in chapter 2.

The scans of the flow rate, cell temperature, and ablation energy revealed an effect which had not been reported before within the context of a cryogenic source. Under certain conditions, the central peak in the TOF profile broadened to the point of splitting in two. This double peak structure has been examined in more detail and a possible cause has been proposed. Due to the use of nanosecond laser pulses, the dominant ablation process above a certain threshold laser fluence (J/cm^2) is that of phase explosion. The result is that the ablation products are a mix of vapor and liquid droplets, with both phases having their own characteristic velocity and temperature as given by a Maxwell-Boltzmann distribution. Together with the process of thermalization inside the cell, this phenomenon of phase explosion was found to be an adequate explanation of the emerging double peak structure. While the effect is avoidable, certain combinations of experimental parameters (SrF$_2$ target, fluence of 24 J/cm^2, neon flow rate of 9 SCCM, and a cell temperature of 20 K) can result in a slow peak which contains a significant fraction of the total number of SrF molecules in the beam. These conditions could possibly be exploited in the deceleration process, since a lower starting velocity would require less deceleration strength, which in turn minimizes

the losses in the decelerator and increases the number of successfully decelerated molecules. Alternatively, the use of a different target (Sr metal) requires lower ablation energies, so the double peak phenomenon can be avoided by using such a target and not operating the ablation laser near the threshold value.

The final topic of chapter 4 has been the interpretation of the LIF signals, more specifically by combining the information from both the absorption and LIF signals from the same measurement in order to extract the true velocity distribution of the beam. The analysis assumed that the absorption signal, being close to the cell exit, mostly contains information about the spatial distribution of the beam, while the TOF profile as measured by LIF detection is significantly affected by both the velocity spread of the beam and the length of the molecular pulse. By deconvolving the measured LIF signal using the absorption signal, an attempt was made to extract the "true" TOF profile. In comparing the deconvolved signal with the measured TOF profile, it was found that the predominant effect of the pulse width is the broadening of the measured LIF signal. While the analysis provided in this work could not find a reliable and robust method of extracting the true transverse temperature and mean forward velocity of the beam, a general framework has been developed. The application of this framework remains an open question, since the measured absorption signal was found to not be an accurate estimate of the response function. In reality, this response function contains information about the electronic response of the system and other factors specific to the experimental setup and conditions, like the many possible paths of the molecules inside the cell, but both its exact shape and the contributions of these factors are at this moment not understood.

5.2 Outlook

The focus of this thesis has mostly been the characterization of the source. We will now conclude by looking at the next steps, both for the cryogenic source and the NL-eEDM collaboration. Suggestions for additional measurements or potentially interesting avenues of research are listed as well.

5.2.1 Short term: recent and upcoming milestones relating to the source

Towards the end of this project, this characterization phase came to its conclusion when the lab was reorganized. This included moving the source towards the start of a newly aligned Stark decelerator. When all the equipment was back in place and signal was found again, the source was connected to the decelerator. At the time of writing, the first SrF signal at the other end of the decelerator has been measured. This cryogenic SrF beam is being decelerated down to increasingly lower velocities, with the ultimate goal of stopping the molecules altogether. Right now it is the first and only experiment where a cryogenic source and a Stark decelerator have been combined. The characterization of this deceleration is currently taking place.

5.2.2 Intermediate term: possible additional measurements and angles to explore

This does not necessarily mean that the source is completely understood or that there are no improvements to be made. For example, the stability of the source on a timescale of 24 hours, which is the timescale required for the planned eEDM measurement, has not been investigated in detail yet. The design of our source is based on the work of an Imperial College group, who have reported on some issues they ran into when operating the source for a prolonged amount of time [50]. They noted that after about 24 hours of continuous operation, the cryopumps would start to saturate. By heating the pumps to 20 K the helium (the buffer gas used in their experiment) would desorb and be pumped away by the vacuum pumps. They also observed a reduction in molecular flux on a similar timescale, which they were able to recover by heating the system up and cooling it back down overnight. In a period of about 12 hours, they heated the source to 240 K and then back down to their operating temperature of 4 K. The suspected reason for the decrease in molecular flux was that after operating the source for so long, enough SF_6 has frozen to the cell walls to obstruct either the exit of the cell or the entry point for SF_6. Presumably our source will show similar behavior if operated for a long enough time. After a certain number of shots, the target will also simply no longer yield a sufficient amount of molecules. We have yet to establish the lifetime of the various targets used in our setup in concrete terms. This depends highly on the ablation laser fluence used, the target itself (metal or salt, scintered or unscintered and for how long), and how efficiently its surface is covered due to its rotation and translation inside the cell.

A suggestion that was explored earlier in this thesis, namely the use of a de Laval nozzle, is still an option that can be examined in some more detail. When discussions took place
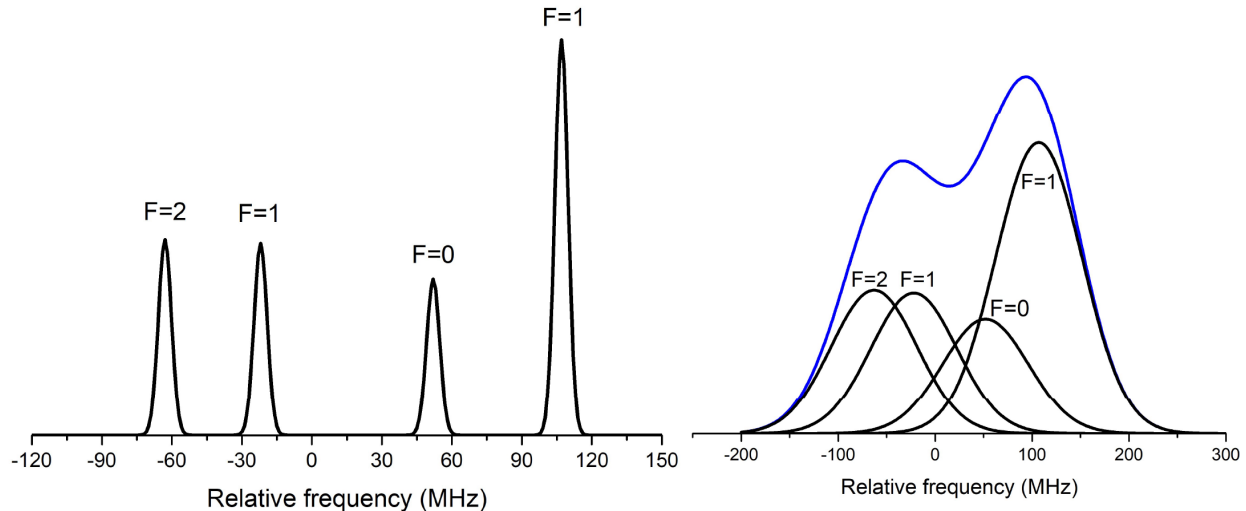
Figure 5.1: The Doppler free absorption spectrum (left) of the $A^2\Pi_{1/2}$ ($v' = 0$, $J = 1/2$) $\leftarrow X^2\Sigma^+$ ($v = 0$, $N = 1$) transition. On the right, the broadened spectrum is shown for a transverse velocity spread of ± 35 m/s. Figure adapted from [53].

on its possible use, the KVI workshop was consulted and they stated that in principle they could craft the required nozzle. Due to time constraints, an ongoing discussion on whether or not such a nozzle would actually help in increasing the amount of molecules within the decelerator's acceptance, and the fact that we have no explicit measurements on the transverse velocity of our beam, we have not yet explored this option. Since the use of such a nozzle has been shown to greatly reduce the transverse velocity spread of a molecular beam originating from a cryogenic buffer gas beam source, while not affecting the forward velocity or its spread significantly, it might still be worth investigating in more detail.

Related to the de Laval nozzle, is the possibility of measuring the transverse velocity spread using Doppler broadened absorption spectroscopy. Calculations show that the broadening of the spectrum of SrF should be observable for the expected transverse velocities. The Doppler shift of a molecule with velocity v and transition frequency ω_0 (wavelength λ_0) will be given by [20]:

$$\delta_f = \frac{kv}{2\pi} = \frac{v}{\lambda_0} \approx 1.5\text{MHz per m/s} \tag{5.1}$$

For a transverse velocity of 35 m/s, this would result in a broadening of 105 MHz. The lifetime of the $A^2\Pi_{1/2}$ state ($\tau \approx 24$ ns [23]) corresponds to a natural linewidth ($\Gamma = 1/\tau$) of 6.6 MHz, so such a broadening should be observable. This effect is illustrated in figure 5.1, which shows a clearly broadened spectrum.

Another possible point of investigation is the repetition rate of the experiment. Other cryogenic sources tend to operate at much lower rates (generally 2 Hz) and mention that, when using higher repetition rates, the number of molecules per shot was greatly reduced and they observed more extreme fluctuations from shot to shot. The Imperial College group [50] reported that at 10 Hz their signal dropped to about 2% of its starting value after 500 shots. We have not observed this behavior at 10 Hz but have also not yet investigated the

effect a different repetition rate would have on our source operating with our particular setup and conditions. At higher repetition rates, the target (and by extension its immediate surroundings) might not have enough time in between ablation laser pulses to recover and get rid of the heat that keeps being introduced. This may lead to heating of the buffer gas or improper thermalization, both of which are undesirable, so it might be worthwhile to examine different repetition rates.

To conclude this section on additional measurements, a recent paper has shown an enhanced yield from a cryogenic source by exciting the atomic precursor [54]. This source produces YbOH from a target made of both Yb and Yb$(OH)_3$. They found that by driving the $^1S_0 \rightarrow {}^3P_1$ transition of Yb inside the cell, the YbOH signal could be increased by as much as a factor of 10. The excitation greatly increased the chemical cross-section for collisions between Yb and other ablation products to form YbOH. The excitation laser was pulsed, from about 4 ms before the ablation pulse until 8 ms after. The enhancement depends linearly on the power of the excitation laser, until it saturates at a factor of about 10 for a laser power of 100 mW. Perhaps a similar effect can be achieved in our source by driving a similar transition in Sr and Ba (to create a SrF or BaF beam respectively). The wavelengths associated with the $^1S_0 \rightarrow {}^3P_1$ transition in both cases are within the visible spectrum and are commercially available (689 nm for Sr [55] and 791 nm for Ba [56]). The difficulty in this case would be to find a clear path for the excitation laser beam into the cell, which might require new holes to be drilled in the shields or moving the ablation laser. It is a promising option though, since it might be able to compensate for the estimated loss (of the number of molecules) of a factor of 15 between the source and the decelerator due to the distance between the two components (assuming no guide or other phase-space matching is employed).

5.2.3   Long term: towards the eEDM measurement

Finally, a number of changes and additions will have to be made in the future. An electrostatic guide, as discussed in chapter 2 (section 2.3.3) is still being designed and then has to be made and inserted into the setup, between the source and the decelerator. This guide needs to be compact in order to fit in this coupling section, so various mechanical and geometric considerations complicate this design process.

After the successful deceleration of SrF, a switch will be made to BaF. In principle, this is as simple as replacing the ablation target with the appropriate precursor and changing the detection laser frequency and deceleration voltages accordingly. Of course things rarely go as planned in experimental research, so this switch will surely come with its own challenges that will have to be overcome in due time. Related to this switch is an upgrade of the high-voltage electronics of the decelerator. The new amplifiers will be able to deliver maximal voltage amplitudes of 10 kV, compared to the 5 kV previously achieved. These amplifiers have been designed and prototyped, but some additional changes still have to be made before the final versions can be ordered.

In the meantime, the parts required for the interaction zone have been ordered, and should be delivered by the end of 2019. The construction of the interaction zone can then commence. Once this has been completed, the interaction zone will first be combined with the supersonic source previously used in the Stark decelerator experiments at the VSI to do a "fast beam eEDM measurement". This can be seen as a proof of concept, to show that the interaction zone functions as desired and the appropriate data acquisition system required to extract an eEDM value from such a setup is in place.

Once the parallel work on both the fast beam eEDM measurement and the deceleration of first SrF and then BaF has wrapped up, and all the components and processes involved are well-understood, these separate components can be connected, together with the addition of laser cooling in between. The completed setup will then finally start measuring the eEDM around 2021, hopefully either setting a new limit on its value or uncovering new physics beyond the Standard Model.

5.3 Acknowledgements

During my time in the NL-eEDM group, I was far from alone. Whether it be fellow master students, crushed by the existential dread that comes with being at the end of one's studies, bachelor students who only barely got a taste of actual research, PhD's and postdocs who seemed to live inside the lab, or professors who always seemed to be both too busy for their own good and like they had too much free time on their hands at the once, there was never a dull moment. I would like to thank the following people for contributing to that:

First and foremost, my first examiner and supervisor Steven Hoekstra. Many thanks for giving me the opportunity and allowing me to return to the VSI. After I finished my bachelor project in the same group, the NL-eEDM experiment remained in my subconscious as I worked my way towards my master project. I could never have guessed that this particular project became available right as I started looking for something to keep me busy for a year. Your help has been invaluable whenever I needed it, and I will continue to admire your ability to manage such a huge project, along with all the other obligations that come with being a professor (and a human being), without going insane. The future of any scientific endeavour is as uncertain as whether an electron has spin up or spin down, but I have great faith in the team you have assembled over the years and your ability to guide them.

Many thanks also to Manuela Vecchi, my second supervisor. Though we have not interacted a whole lot, I am very grateful that you took the time and effort to read this work and assess it. We both come from rather different fields, but I hope that you have stumbled upon some interesting nuggets of knowledge, or that at the very least the process of reading my thesis wasn't a complete bore. I have yet to hear your final words on my thesis, but am sure that they will be fair and provide plenty of constructive criticisms.

An extraordinary amount of thanks to both Kevin Esajas and Yanning Yin, who were my main partners in crime down in the lab. Their combined experience with and knowledge of the source made sure that none of my questions, however silly or time consuming, were left unanswered. Thank you for keeping up with the inexperienced, ignorant master student. Kevin, you have in a way been my mentor through both my bachelor and master projects, and were always kind and understanding in helping me, even when you honestly had better things to do. Yanning, you showed such total devotion to a project you were new to, and interest in whatever minor things I figured out on my own, that I envy those who will have the pleasure of working with you on the source in the future. Without the two of you, this project would never have taken the shape that it has, and whatever that might be, it is undoubtedly many times better than if I would've had to do this without you.

Leo Huisman and Oliver Böll, thank you for the continued technical support, not just surrounding the cryogenic source, but the entire FIS group at the VSI. Though your names may not appear in the papers, it is clear to anyone who has ever worked in a lab that they would have never been written if it wasn't for you guys.

Thanks to my fellow master students as well, who have come and gone, and those of you who have yet to finish their projects:

Mark Buisman and Kees Steinebach, we all ended our bachelor here at the VSI, and now we meet again to finish our masters. You both still have a while to go so keep my spirit alive while you can. Hidde Makaske, the same is true for you. I will never forget all the outlandish stories you've told over the past year, and the way in which you presented them.

Never a wasted moment with you. I have no idea where you will end up in life but your future colleagues are gonna have one hell of a time. I hope it involves aligning in one way or another.

Sander Vermeulen, we've laughed quite a bit both in and outside of office hours, sometimes at ourselves, sometimes at others, but almost always at the state of the world. These final few months the office have been considerably more quiet and empty without you, but maybe that's been a good thing for my thesis...

Let's not forget the PhD students, who still have many years to spend in labs, behind computers, and at conferences:

Ginny Marshall, you were always the life of the proverbial party. Whether it be nerdy comic-book shenanigans or whatever the UK happened to be up to that day or just the general struggles of experiencing and adapting to the Dutch lifestyle, rarely was there an unwanted silence. The heart and sincerity with which you continue to travel through life, together with your genuine care for everyone's well-being, has attenuated my own cynicism. Maybe in 3 years the UK won't take you back, and we'll be better off for it. Yes, I did just end on Brexit. Sorry not sorry.

Thomas Meijknecht, thanks for the entertainment in the office. The random outbursts of screaming and/or laughing never failed to amuse me from behind the comically small monitor between us. Keep posting those wisdoms of yours like clockwork, maybe somewhere down the line someone will recognize the valuable life lessons to be extracted from your paradoxical ramblings.

Parul Aggarwal, Mina Morshed Behbahani, Anno Touwen, Artem Zapara, Elwin Dijck, Maarten Mooij, and all the theorists from across campus, thank you for all the good times, both scientific and less so.

Finally, a thank you to all the professors who were not directly involved with my project but have been in my general vicinity for a good while over the past year, including but not limited to: Anastasia Borschevsky, Gerco Onderwater, Lorenz Willmann, Klaus Jungmann, and Rick Bethlem. To everybody involved in the NL-eEDM project not covered by the previous categories: thank you, I had a wonderful time, no doubt thanks to you.

Appendix A

Matlab scripts used

All Matlab scripts used to analyze and interpret data are listed here. Some optional functionality is commented, and the many variables and files referred to should be adjusted accordingly when any of the code is used. Some additional figures in this work were made using Matlab to illustrate theoretical behavior or idealized situations, but their reconstruction is trivial since the necessary equations are all either mentioned explicitly or can be found in the references. For this reason, those scripts are not listed in this appendix.

A.1 Script to convert raw data to LIF TOF and absorption signal

The raw data from the source consists of timestamps, a trigger signal, the number of counts for those timestamps, and the voltage from the absorption photodiode. The trigger signal is equal to "1" every time the ablation laser is fired, which happens at a rate of 10 Hz. In order to construct the signals as seen throughout this work, the many measurement cycles have to be combined. This script accumulates all the photon counts with the same timestamps and averages the voltage from the photodiode over the total number of repetitions. Input is the raw file where the first column is the trigger signal, the second column the counts from the PMT, the third column the photodiode voltage, and the fourth column the timestamps. Output is a file containing all unique timestamps in the first column, the associated photon counts in the second, and the averaged voltage in the third.

```
% Rutger Hof 2019
% script to construct LIF TOF and absorption from raw source data (timestamps, counts, voltage)

% clear memory and start timer
tic
clear all
% import data
data=readmatrix('20_June_2019_205735.txt');
% set columns as variables
timestamps=data(2:length(data),4);
absorb=data(2:length(data),3);
counts=data(2:length(data),2);
trigger=data(2:length(data),1);
% find the starts of new cyles
start=find(trigger==1);

% set time
test=unique(timestamps);
% for loop over cycles
total=1:length(test);
absorbtion=1:length(test);
for i=1:length(test)
```

```
        total(i)=sum(counts(find(timestamps==test(i))));
        absorbtion(i)=sum(absorb(find(timestamps==test(i))))/length(find(timestamps==test(i)));
end

% combine time, LIF, and absorption into 1 file
mat=[test(:),total(:),absorbtion(:)];

% plot result
plot(mat(:,1),mat(:,2))
xlabel('Time (s)')
ylabel('Signal (counts)')
xlim([0 5e−3])

% optional: save file
%dlmwrite('histogram_09_September_2019_092057_ALT.txt', mat,'\t')
toc
```

A.2   Script to estimate the number of molecules using both LIF and absorption signals

Input is a file like the output of the previous script to convert the raw data into TOF profiles, along with several experimental parameters. Most notably the distance "dlif" from the ablation to the LIF detection region, the absorption probe beam diameter "probebeam", aperture diameter "aperture", detection wavelength "wl", and the correction factors as discussed in chapter 4. Output is the number of molecules per shot from absorption "number" and LIF "lifcounts".

```
% Rutger Hof 2019
% This script will analyse the absorption and LIF signal from a cryogenic source, and give you a molecule
% number, as well as how long it took to calculate.

% start timer and clear memory
clear all
tic
% read data (contains both LIF and absorption)
absorption = readmatrix('histogram_09_September_2019_092348.txt');
% set # of shots
shots=2744;

% use the different columns, name them appropriately
t=absorption(:,1);
lif=absorption(:,2);
abso=absorption(:,3);

% set lif bg region and calculate absorption background
bstart=0.00999;
bend=max(t);
bg=mean(abso(find(t==bstart):find(t==bend)));

% make histogram of signal in background interval (optional)
figure(3)
histogram(abso(find(t==bstart):find(t==bend)));

% normalize absorption signal
signal=abso/bg;

% calculate the quantity to integrate
ln=−log(signal);
% now we integrate, using trapezoid method
int=trapz(t,ln);
% find mean forward v from lif signal
    tmaxlif=t(find(lif==max(lif)));        % times at which maximum lif appears
                                           % if more than 1 is found, find the mean to use for calculation
    if max(size(tmaxlif))>1
        tmaxlif=sum(t(find(lif==max(lif))))/max(size(tmaxlif));
    else
        tmaxlif=t(find(lif==max(lif)));
    end

dlif=0.312;                            % distance from source for LIF
meanv=dlif/tmaxlif;                    % find mean v from v=d/t

% set some constants
length=4.5e−3;                         % absorption path length
aperture=4.5e−3;                       % diameter of exit aperture
probebeam=4e−3;                        % diameter of probe beam

% calculate area: square part + 2 slices along circle
```

```
% assumes that SrF beam has same diameter as the apperture, since the
% probing laser is very close to the exit form the cell
area=pi*(aperture/2)^2;
overlap=probebeam/2*sqrt(aperture^2-probebeam^2)+aperture^2/2*asin(probebeam/aperture);

% absorption cross section, simplified, from Barry (2013)
wl=663.3e-9;
cross=3*wl^2/(2*pi);

% correction factor due to Doppler effect, assuming gaussian distribution
% of transverse velocity
gausmean=0;
gausstd=30;
linewidth=1e6;
shift=663e-9*linewidth;
lim=[-shift shift];
cp=normcdf(lim,gausmean,gausstd);
P=cp(2)-cp(1);
dopplercorrection=1/P;

% from Barry thesis (2013), find number of molecules from absorption
number=(area/overlap)*(overlap*meanv)/(cross*length)*int*dopplercorrection

% now to find the number of molecules according to lif:
lifamp=1000;                            % amplification factor for lif (in case of ND filter)
lifbg=mean(lif(find(t==bstart):find(t==bend)));
% set correction factors
solidangle=1.1;
scatter=10;
pmt=0.33;
optics=0.8;
% find number of detected molecules using LIF signal
lifcounts=sum(lif-lifbg)*lifamp/shots*dopplercorrection*4*pi/(solidangle*scatter*pmt*optics)

% lets scale time into ms instead of s before plotting
t=1000*t;

% optional: plot absorption signal
figure(1)
plot(t,signal)
xlim([0 5])
xlabel('Time (ms)', 'FontSize', 14)
ylabel('Signal (normalized)', 'FontSize', 14)

% optional: plot LIF signal
figure(2)
plot(t,lif)
xlim([0 5])
xlabel('Time (ms)', 'FontSize', 14)
ylabel('Signal (counts)', 'FontSize', 14)

toc
```

A.3   Script to fit LIF signal to bimodal Maxwell-Boltzmann distribution

Input is a file containing the LIF signal and timestamps. Parameters to be set are constants like the mass of the detected molecule and the Boltzmann constant, and experimental parameters like the distance from ablation to detection. Crucial parameters are the background region and initial guesses for the fit parameters. Output consists of multiple figures and the final fit parameters.

```
% Rutger Hof 2019
% script to fit data to 2 peak structure using nonlin fitting
clear all
tic                                      % start timer
% read data
data = readmatrix('histogram_09_September_2019_092057.txt');

% use the different columns, name them appropriately
t=data(:,1);
lif=data(:,2);

% optional: plot signal to find initial guess values
%plot(t,lif)

% set bg region
bstart=1e-02;
bend=max(t);
```

```matlab
% set background by looking at bg region
bg=mean(lif(find(t==bstart):find(t==bend)));

% optional: histogram of bg
figure(1)
histogram(lif(find(t==bstart):find(t==bend)))
title('Histogram of background region')
xlabel('Number of counts', 'FontSize', 14)
ylabel('Occurrence', 'FontSize', 14)

% set constants
k=1.3807*10^(-23);
m=(87.62+18.99840)*1.660539*10^(-27);
l=0.312;

% function to fit using given starting guess
% p=parameters=[c1 v1 T1 c2 v2 T2]
fun = @(p,t) (bg+p(1)*(l./t).^2.*exp(-m/(2*k*p(3))*(l./t-p(2)).^2)+p(4)*(l./t).^2.*exp(-m/(2*k*p(6))*(l./t
    -p(5)).^2));

% set starting guess. required input: guess for temperatures (index 3 and 6)and
% location+height of peaks
firstpeak=t(find(lif==max(lif)));
secpeak=firstpeak+3e-5;
peak=lif(t==firstpeak);
rel=lif(t==secpeak);
T1=3;
T2=3;

% from the guesses above, find guess values for the parameters
pguess = [1,1,T1,1,1,T2];
pguess(5)=l/firstpeak;
pguess(4)=peak/pguess(5)^2;
pguess(2)=l/secpeak;
pguess(1)=0.6*rel/pguess(2)^2;

% optimise using nlinfit
[p,resid,J,cov,mse] = nlinfit(t,lif,fun,pguess);
% Give CI because why not
ci=nlparci(p,resid,'Jacobian',J);
% Alternate way to compute CI
cicov=nlparci(p,resid,'covar',cov);

% from CI get error
errorv1=(ci(2,2)-ci(2,1))/2;
errorv2=(ci(5,2)-ci(5,1))/2;
errort1=(ci(3,2)-ci(3,1))/2;
errort2=(ci(6,2)-ci(6,1))/2;
errora1=(ci(1,2)-ci(1,1))/2;
errora2=(ci(4,2)-ci(4,1))/2;
% list values and errors, first v, then T, then A
error=[errorv1 errorv2 errort1 errort2 errora1 errora2]
values=[p(2) p(5) p(3) p(6) p(1) p(4)]

% actually calculate the fit
fit=bg+ p(1)*(l./t).^2.*exp(-m/(2*k*p(3))*(l./t-p(2)).^2)+p(4)*(l./t).^2.*exp(-m/(2*k*p(6))*(l./t-p(5))
    .^2);

% lets scale time into ms instead of s before plotting
t=1000*t;

% optional: plot LIF signal
figure(2)
plot(t,lif)
xlim([0 5])
title('LIF signal over time')
xlabel('Time (ms)', 'FontSize', 14)
ylabel('Signal (counts)', 'FontSize', 14)

% plot the fit
figure(3)
plot(t,fit)
xlim([0 5])
title('Fitted signal')
xlabel('Time (ms)', 'FontSize', 14)
ylabel('Signal (counts)', 'FontSize', 14)

% plot the residue
figure(4)
plot(t,resid)
xlim([0 5])
title('Residue')
xlabel('Time (ms)', 'FontSize', 14)
ylabel('Difference', 'FontSize', 14)

% optional: histogram of residue
figure(5)
histogram(resid)
title('Histogram of the residue')
xlabel('Residue', 'FontSize', 14)
ylabel('Occurrence', 'FontSize', 14)
```

```
% plot fit and data in same graph
figure(6)
plot(t,lif)
hold on
plot(t,fit)
hold on
xlim([0 5])
title('Fitted signal and data for ablation power of 930V')
xlabel('Time (ms)', 'FontSize', 14)
ylabel('Signal (counts)', 'FontSize', 14)
legend('Data','Fit', 'FontSize', 12)

toc
```

A.4 Script to fit LIF signal to a single Maxwell-Boltzmann distribution

Input is a file containing the LIF signal and timestamps. Parameters to be set are constants like the mass of the detected molecule and the Boltzmann constant, and experimental parameters like the distance from ablation to detection. Crucial parameters are the background region and initial guesses for the fit parameters. Output consists of multiple figures and the final fit parameters.

```
% Rutger Hof 2019
% script to fit data to single MB using nonlin fitting
clear all
tic                                    % start timer
% read data
data = readmatrix('histogram_09_September_2019_092057.txt');

% use the different columns, name them appropriately
t=data(:,1);
lif=data(:,2);

% optional: plot signal to find initial guess values
%plot(t,lif)

% set bg region
bstart=0.00999;
bend=max(t);

% find background value
bg=mean(lif(find(t==bstart):find(t==bend)));

% optional: histogram of background
figure(1)
histogram(lif(find(t==bstart):find(t==bend)))
title('Histogram of background region')
xlabel('Number of counts', 'FontSize', 14)
ylabel('Occurrence', 'FontSize', 14)

% set constants
k=1.3807*10^(-23);
m=(87.62+18.99840)*1.660539*10^(-27);
l=0.312;

% function to fit using given starting guess
% p=parameters=[c v T]
fun = @(p,t) (bg+p(1)*(l./t).^2.*exp(-m/(2*k*p(3))*(l./t-p(2)).^2));

% set starting guess. required input: guess for temperature (index 3) and
% location+height of peak
peak=max(lif);
firstpeak=t(lif==peak);
T1=12;

% from the guesses above, find guess values for the parameters
pguess = [1,1,T1];
pguess(2)=l/firstpeak;
pguess(1)=peak/pguess(2)^2;

% optimise using least squares
[p,resid,J,cov,mse] = nlinfit(t,lif,fun,pguess);
% Give CI
ci=nlparci(p,resid,'Jacobian',J);
% Alternate way to compute CI
cicov=nlparci(p,resid,'covar',cov);
```

```matlab
% from CI get error
errorv1=(ci(2,2)-ci(2,1))/2;
errort1=(ci(3,2)-ci(3,1))/2;
% list values and errors, first v, then T, then A
error=[errorv1 errort1]
values=[p(2) p(3)]

% actually calculate the fit
fit=bg+ p(1)*(l./t).^2.*exp(-m/(2*k*p(3))*(l./t-p(2)).^2);

% lets scale time into ms instead of s before plotting
t=1000*t;

% optional: plot LIF signal
figure(2)
plot(t,lif)
xlim([0 5])
title('LIF signal over time')
xlabel('Time (ms)', 'FontSize', 14)
ylabel('Signal (counts)', 'FontSize', 14)

% plot the fit
figure(3)
plot(t,fit)
xlim([0 5])
title('Fitted signal')
xlabel('Time (ms)', 'FontSize', 14)
ylabel('Signal (counts)', 'FontSize', 14)

% plot the residue
figure(4)
plot(t,resid)
xlim([0 5])
title('Residue')
xlabel('Time (ms)', 'FontSize', 14)
ylabel('Difference', 'FontSize', 14)

% optional: histogram of residue
figure(5)
histogram(resid)
title('Histogram of the residue')
xlabel('Residue', 'FontSize', 14)
ylabel('Occurrence', 'FontSize', 14)

% plot fit and data in same graph
figure(6)
plot(t,lif)
hold on
plot(t,fit)
hold on
xlim([0 5])
title('Fitted signal and data')
xlabel('Time (ms)', 'FontSize', 14)
ylabel('Signal (counts)', 'FontSize', 14)
legend('Data','Fit', 'FontSize', 12)

toc
```

A.5   Script to deconvolve LIF signal

Input is a file containing the LIF signal, absorption signal, and timestamps. Parameters to be set are constants like the mass of the detected molecule and the Boltzmann constant, and experimental parameters like the distance from ablation to detection. Optional functionality is to provide the parameters for a Maxwell-Boltzmann function or the analytic expression from chapter 4 to compare with the LIF signal and/or deconvolved signal. Ideal value of "ns" (ϕ in chapter 4) has to be found through trial and error. Output shows the deconvolved signal both with and without the use of Wiener filtering, in combination with the LIF signal (and optionally the aforementioned Maxwell-Boltzmann and analytic functions). The option to save the devoncolved signal as .txt file is included.

```matlab
% Rutger Hof 2019
% script to deconvolve LIF

clear all
tic
% read the appropriate file and name variables
data=readmatrix('histogram_09_September_2019_092348.txt');
```

```
t=data(2:length(data),1);
lif=data(2:length(data),2);
abso=data(2:length(data),3);

% set lif background region
bstart=0.00999;
bend=max(t);
bg=mean(lif(find(t==bstart):find(t==bend)));
% set absorption background region
bg_abs=mean(abso(find(t==bstart):find(t==bend)));
% find fractional absorption
abso=abso./bg_abs;

% set constants
k=1.3807*10^(-23);
m=(87.62+18.99840)*1.660539*10^(-27);
l=0.312;

% Maxwell-Bolztmann distribution according to best fit (parametersmust be set manually)
A=1;
v_mean=177;
T=17;
mb=bg+ A*(l./t).^2.*exp(-m/(2*k*T)*(l./t-v_mean).^2);

% normalize absorption signal and flip to make estimate of response function
abso=(1-abso)./max(1-abso);

% optional: analytic expression assuming valve opening time tau
alpha=sqrt((2*k*T/m));
tau=1e-3;
z_1=(l./(alpha*abs(t-tau)))-v_mean/alpha;
z_2=(l./(alpha*t))-v_mean/alpha;
signal=erf(z_1)-erf(z_2);
signal=signal./max(signal);

% deconvolution using fft
f_mb=fft(abso);
f_lif=fft(lif);
% wiener filter
ns=10^(-3)*max(lif);
wien_f_mb=conj(f_mb)./(abs(f_mb).^2+ns);

% deconvolution using wiener filter
wien_f_conv=f_lif.*wien_f_mb;
wien_conv=abs(ifft(wien_f_conv));

% regular deconvolution
f_conv=f_lif./f_mb;
conv=abs(ifft(f_conv));

% optional: save deconvolved signal
%mat=[t,abs(wien_conv)];
%dlmwrite('conv_09_September_2019_092348.txt', mat,'\t')

% scale time to ms
t=1000*t;

figure(1)
plot(t,abs(wien_conv))
%title('Deconvolved signal using Wiener filtering', 'FontSize', 14)
xlabel('Time (ms)', 'FontSize', 14)
ylabel('Signal (a.u.)', 'FontSize', 14)
xlim([0 10])

figure(2)
plot(t,abs(conv))
%title('Deconvolved signal without filtering', 'FontSize', 14)
xlabel('Time (ms)', 'FontSize', 14)
ylabel('Signal (a.u.)', 'FontSize', 14)
xlim([0 10])

% normalize signals
wien_conv=wien_conv./max(wien_conv);
mb=mb./max(mb);

figure(4)
plot(t,abs(wien_conv))
hold on
lif=lif./max(lif);
plot(t,lif)
%title('Deconvolved signal and LIF signal', 'FontSize', 14)
xlabel('Time (ms)', 'FontSize', 14)
ylabel('Signal (normalized)', 'FontSize', 14)
legend('Deconvolved signal','Measured LIF signal', 'FontSize', 14)
xlim([0 5])

toc
```

Appendix B

Fits of LIF signal to bimodal Maxwell-Boltzmann distributions

The fits as found using two Maxwell-Boltzmann distributions in section 4.3.1 for 8 different ablation laser energies (converted into fluence) are listed here. Both the fitted and raw LIF signal are plotted, and the velocities and temperatures of the two peaks are given.
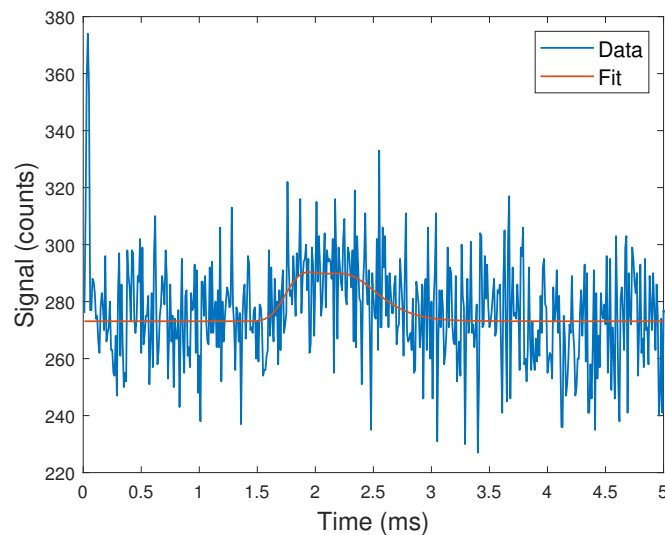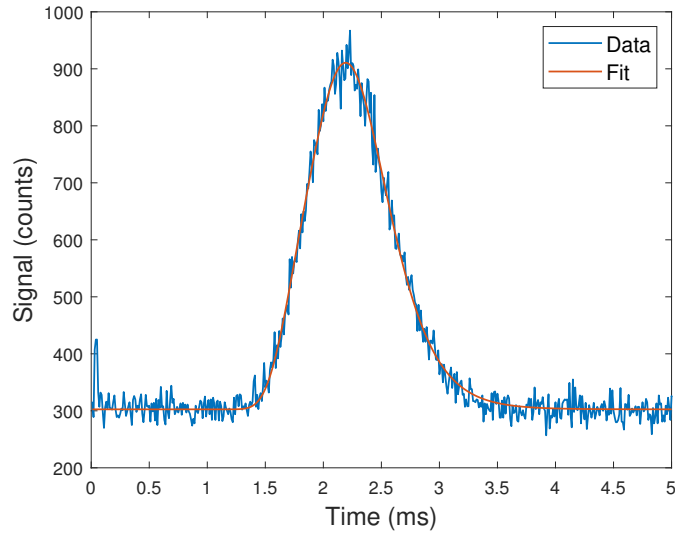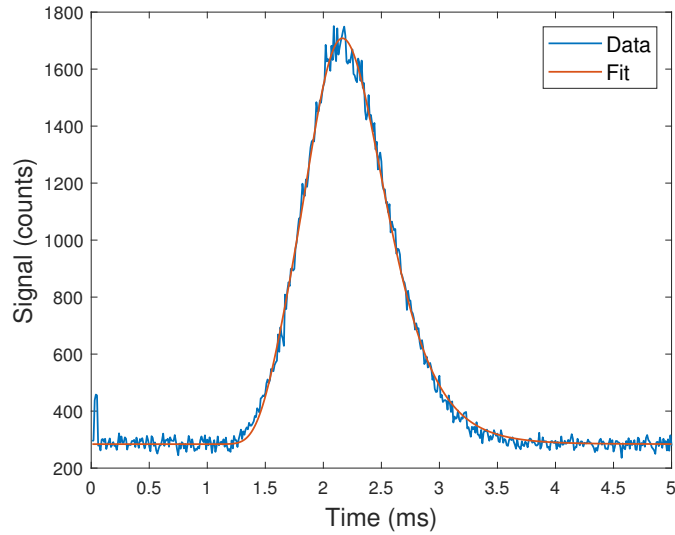
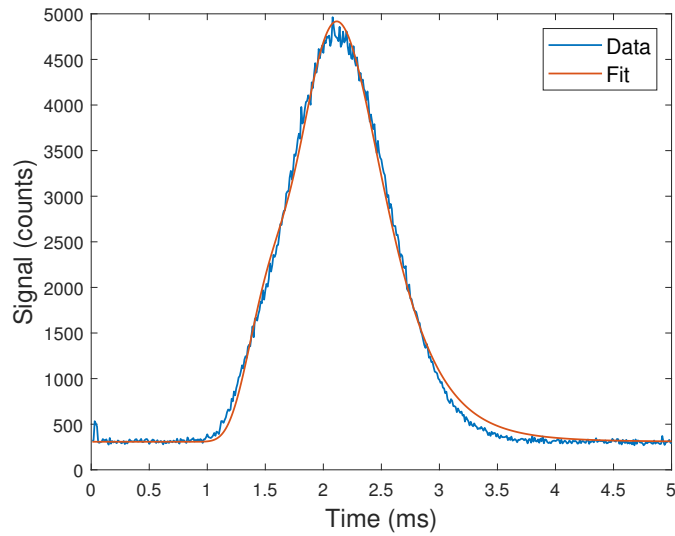

Figure B.1: LIF signal and fit for a fluence of 8.5 J/cm^2, a neon flow rate of 9 SCCM, and cell temperature of 20 K. The fit parameters are $v_1 = 148 \pm 34$ m/s, $v_2 = 146 \pm 34$ m/s, $T_1 = 3 \pm 35$ K, and $T_2 = 4 \pm 35$ K
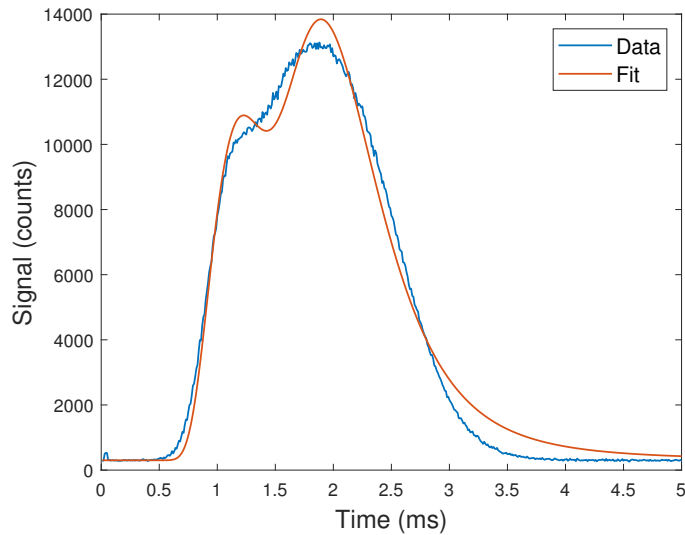
Figure B.2: LIF signal and fit for a fluence of 12 J/cm^2, a neon flow rate of 9 SCCM, and cell temperature of 20 K. The fit parameters are $v_1 = 153 \pm 25$ m/s, $v_2 = 131 \pm 3$ m/s, $T_1 = 5 \pm 4$ K, and $T_2 = 4 \pm 2$ K

Figure B.3: LIF signal and fit for a fluence of 15 J/cm^2, a neon flow rate of 9 SCCM, and cell temperature of 20 K. The fit parameters are $v_1 = 158 \pm 14$ m/s, $v_2 = 134 \pm 0.8$ m/s, $T_1 = 9 \pm 3$ K, and $T_2 = 4.7 \pm 0.6$ K

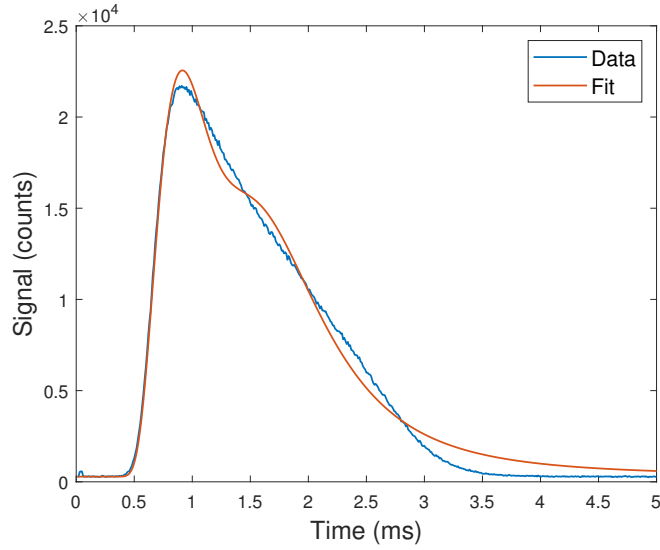Figure B.4: LIF signal and fit for a fluence of 20 J/cm^2, a neon flow rate of 9 SCCM, and cell temperature of 20 K. The fit parameters are $v_1 = 172 \pm 3$ m/s, $v_2 = 136.2 \pm 0.1$ m/s, $T_1 = 17 \pm 1$ K, and $T_2 = 6 \pm 0.2$ K

Figure B.5: LIF signal and fit for a fluence of 24 J/cm^2, a neon flow rate of 9 SCCM, and cell temperature of 20 K. The fit parameters are $v_1 = 214 \pm 2$ m/s, $v_2 = 145 \pm 0.2$ m/s, $T_1 = 69 \pm 2$ K, and $T_2 = 11.7 \pm 0.3$ K
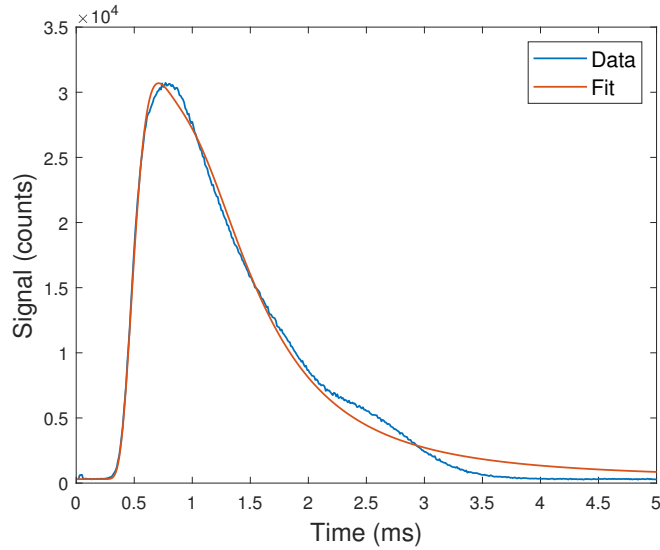
Figure B.6: LIF signal and fit for a fluence of 31 J/cm^2, a neon flow rate of 9 SCCM, and cell temperature of 20 K. The fit parameters are $v_1 = 261 \pm 2$ m/s, $v_2 = 159 \pm 0.4$ m/s, $T_1 = 175 \pm 3$ K, and $T_2 = 24.4 \pm 0.7$ K

Figure B.7: LIF signal and fit for a fluence of 35 J/cm^2, a neon flow rate of 9 SCCM, and cell temperature of 20 K. The fit parameters are $v_1 = 333 \pm 8$ m/s, $v_2 = 189.6 \pm 0.9$ m/s, $T_1 = 381 \pm 13$ K, and $T_2 = 109 \pm 5$ K
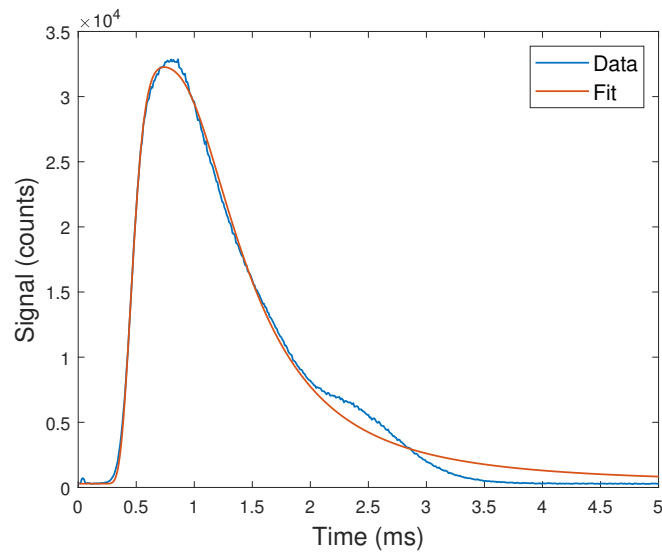
Figure B.8: LIF signal and fit for a fluence of 42 J/cm^2, a neon flow rate of 9 SCCM, and cell temperature of 20 K. The fit parameters are $v_1 = 357 \pm 12$ m/s, $v_2 = 203.8 \pm 0.8$ m/s, $T_1 = 415 \pm 18$ K, and $T_2 = 139 \pm 6$ K

Appendix C

Cell temperature scans using different neon flow rates

The figures below show the emergence of the double peak structure during scans of the cell temperature for different buffer gas flow rates (3, 10, and 20 SCCM). The behavior is similar in all three cases, but the splitting takes place at higher cell temperatures as the flow rate increases. While the fast peak is similar in all scans, the slow peak seems to reach later arrival times as the flow rate increases, although the signal also decreases.
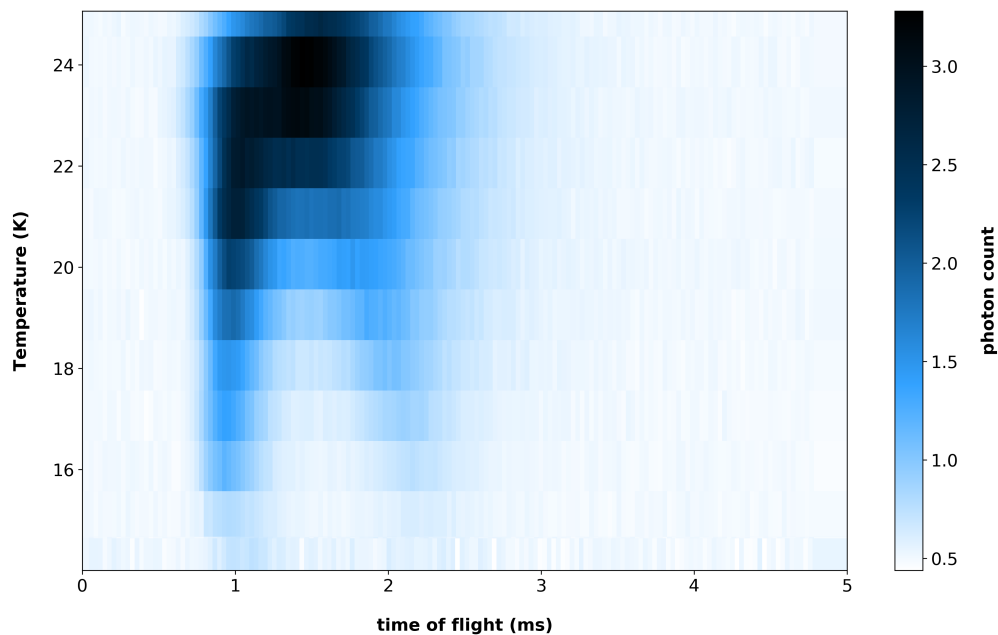

Figure C.1: A scan of the cell temperature from 14 to 25 K, using a neon flow rate of 3 SCCM and an ablation energy of 191 mJ per shot. The horizontal axis represents arrival time (ms) while the vertical axis shows the flow rate (SCCM). The color shows the amount of signal (photon counts) for a given timestamp and cell temperature.

Figure C.2: A scan of the cell temperature from 14 to 25 K, using a neon flow rate of 10 SCCM and an ablation energy of 191 mJ per shot. The horizontal axis represents arrival time (ms) while the vertical axis shows the flow rate (SCCM). The color shows the amount of signal (photon counts) for a given timestamp and cell temperature.
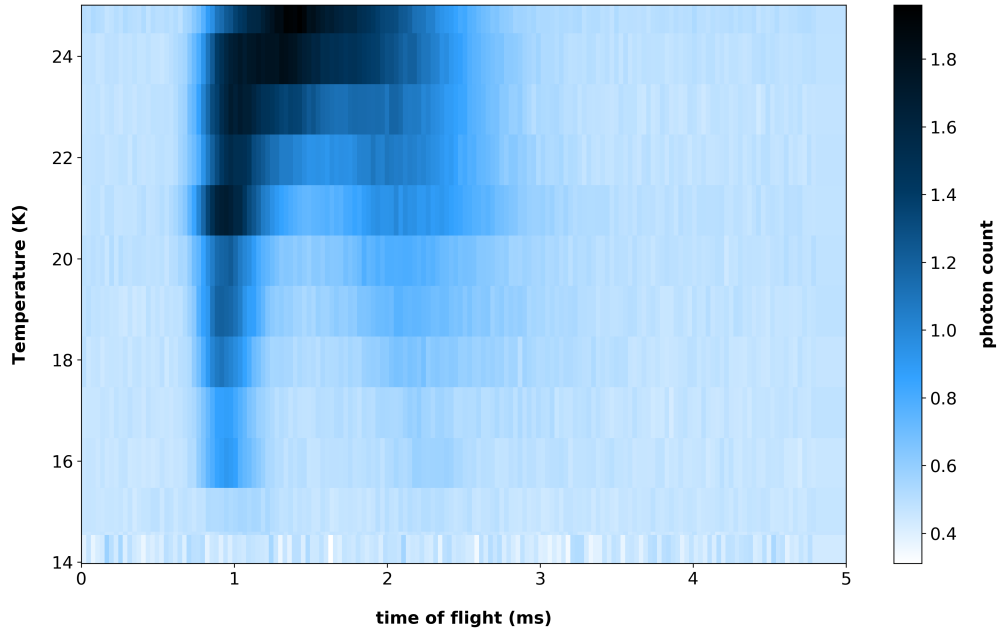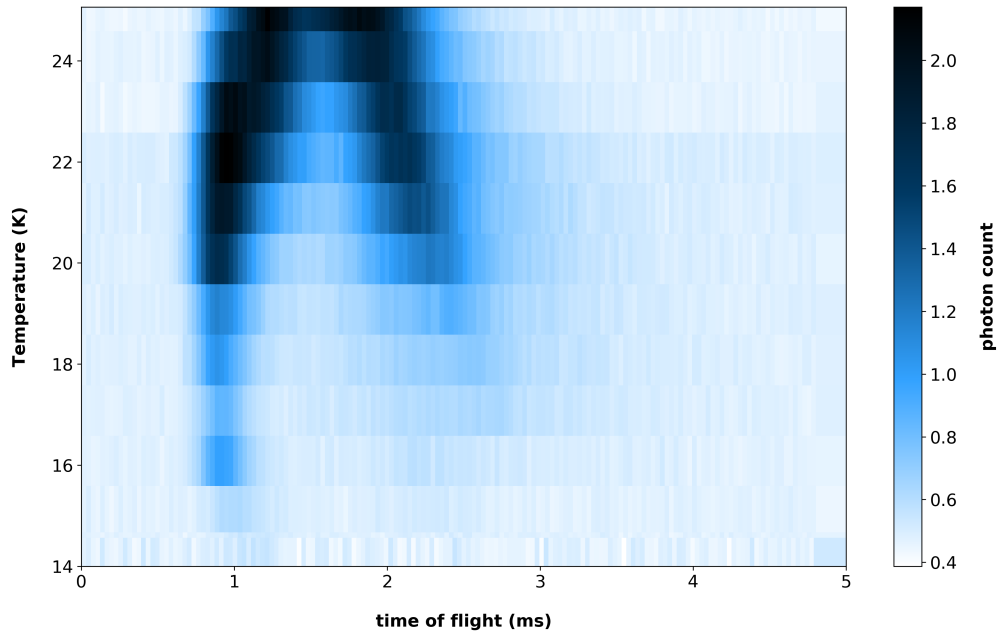

Figure C.3: A scan of the cell temperature from 14 to 25 K, using a neon flow rate of 20 SCCM and an ablation energy of 191 mJ per shot. The horizontal axis represents arrival time (ms) while the vertical axis shows the flow rate (SCCM). The color shows the amount of signal (photon counts) for a given timestamp and cell temperature.

Bibliography

[1] S. Abachi, B. Abbott, M. Abolins, B.S. Acharya, I. Adam, D.L. Adams, M. Adams, S. Ahn, H. Aihara, G. Alvarez, et al. Search for high mass top quark production in p p collisions at s= 1.8 tev. *Physical Review Letters*, 74(13):2422, 1995.

[2] F. Abe, H. Akimoto, A. Akopian, M.G. Albrow, S.R. Amendolia, D. Amidei, J. Antos, C. Anway-Wiese, S. Aota, G. Apollinari, et al. Observation of top quark production in p p collisions with the collider detector at fermilab. *Physical review letters*, 74(14):2626, 1995.

[3] K. Kodama, N. Ushida, C. Andreopoulos, N. Saoulidou, G. Tzanakos, P. Yager, B. Baller, D. Boehnlein, W. Freeman, B. Lundberg, et al. Observation of tau neutrino interactions. *Physics Letters B*, 504(3):218–224, 2001.

[4] S. Chatrchyan, V. Khachatryan, A.M. Sirunyan, A. Tumasyan, W. Adam, E. Aguilo, T. Bergauer, M. Dragicevic, J. Erö, C. Fabjan, et al. Observation of a new boson at a mass of 125 gev with the cms experiment at the lhc. *Physics Letters B*, 716(1):30–61, 2012.

[5] G. Aad, T. Abajyan, B. Abbott, J. Abdallah, S.A. Khalek, A.A. Abdelalim, O. Abdinov, R. Aben, B. Abi, M. Abolins, et al. Observation of a new particle in the search for the standard model higgs boson with the atlas detector at the lhc. *Physics Letters B*, 716(1):1–29, 2012.

[6] M. Benedikt and F. Zimmermann. Towards future circular colliders. *Journal of the Korean Physical Society*, 69(6):893–902, 2016.

[7] K. Oide, M. Aiba, S. Aumon, M. Benedikt, A. Blondel, A. Bogomyagkov, M. Boscolo, H. Burkhardt, Y. Cai, A. Doblhammer, et al. Design of beam optics for the future circular collider e+ e- collider rings. *Physical Review Accelerators and Beams*, 19(11):111005, 2016.

[8] M.K. Gaillard, P.D. Grannis, and F.J. Sciulli. The standard model of particle physics. *Reviews of Modern Physics*, 71(2):S96, 1999.

[9] S.P. Martin. A supersymmetry primer. In *Perspectives on supersymmetry II*, pages 1–153. World Scientific, 2010.

[10] V. Cirigliano and M.J. Ramsey-Musolf. Low energy probes of physics beyond the standard model. *Progress in Particle and Nuclear Physics*, 71:2–20, 2013.

[11] A. Czarnecki and W.J. Marciano. Muon anomalous magnetic moment: A harbinger for new physics. *Physical Review D*, 64(1):013014, 2001.

[12] K. Jungmann. Searching for electric dipole moments. *Annalen der Physik*, 525(8-9):550–564, 2013.

[13] V.A. Dzuba and V.V. Flambaum. Parity violation and electric dipole moments in atoms and molecules. *International Journal of Modern Physics E*, 21(11):1230010, 2012.

[14] W. Pauli. Exclusion principle, lorentz group and reflection of space-time and charge. In *Wolfgang Pauli*, pages 459–479. Springer, 1988.

[15] G. Luders. On the equivalence of invariance under time reversal and under particle-antiparticle conjugation for relativistic field theories. *Kong. Dan. Vid. Sel. Mat. Fys. Med.*, 28:1–17, 1954.

[16] M. Pospelov and A. Ritz. Electric dipole moments as probes of new physics. *Annals of physics*, 318(1):119–169, 2005.

[17] A. Czarnecki and W.J. Marciano. Electromagnetic dipole moments and new physics. *Adv. Ser. Direct. High Energy Phys.*, 20:11–67, 2010.

[18] ACME Collaboration. Improved limit on the electric dipole moment of the electron. *Nature*, 562:355–360, 2018.

[19] NL-eEDM collaboration: P. Aggarwal, H.L. Bethlem, A. Borschevsky, M. Denis, K. Esajas, P.A.B. Haase, Y. Hao, S. Hoekstra, K. Jungmann, T.B. Meijknecht, M.C. Mooij, R.G.E. Timmermans, W. Ubachs, L. Wilman, and A. Zapara. Measuring the electric dipole moment of the electron in baf. *The European Physical Journal D*, 72(11):197, 2018.

[20] C.J. Foot et al. *Atomic physics*, volume 7. Oxford University Press, 2005.

[21] D. DeMille. Diatomic molecules, a window onto fundamental physics. *Physics Today*, 68(12):34–40, 2015.

[22] J.J. Hudson, D.M. Kara, I.J. Smallman, B.E. Sauer, M.R. Tarbutt, and E.A. Hinds. Improved measurement of the shape of the electron. *Nature*, 473(7348):493, 2011.

[23] Y. Hao, L.F. Pašteka, L. Visscher, P. Aggarwal, H.L. Bethlem, A. Boeschoten, A. Borschevsky, M. Denis, K. Esajas, S. Hoekstra, et al. High accuracy theoretical investigations of caf, srf, and baf and implications for laser-cooling. *The Journal of chemical physics*, 151(3):034302, 2019.

[24] M.F. Tu, J.J. Ho, C.C. Hsieh, and Y.C. Chen. Intense srf radical beam for molecular cooling experiments. *Review of Scientific Instruments*, 80(11):113111, 2009.

[25] P. Aggarwal, V.R. Marshall, H.L. Bethlem, A. Boeschoten, A. Borschevsky, M. Denis, K. Esajas, Y. Hao, S. Hoekstra, K. Jungmann, et al. Lifetime measurements of the $a^2\pi_{1/2}$ and $a^2\pi_{3/2}$ states in baf. *arXiv preprint arXiv:1907.06879*, 2019.

[26] J.E. van den Berg. *Traveling-wave Stark deceleration of SrF molecules.* PhD thesis, Rijksuniversiteit Groningen, 2015.

[27] N.R Hutzler, Hsin-I Lu, and J.M. Doyle. The buffer gas beam: an intense, cold, and slow source for atoms and molecules. *Chemical reviews*, 112(9):4803–4827, 2012.

[28] S.C. Mathavan, A. Zapara, Q. Esajas, and S. Hoekstra. Deceleration of a supersonic beam of srf molecules to 120 m/s. *ChemPhysChem*, 17(22):3709–3713, 2016.

[29] A. Zapara. *Dynamics of molecular beams in a traveling-wave Stark decelerator.* PhD thesis, Rijksuniversiteit Groningen, 2019.

[30] E.S. Shuman, J.F. Barry, and D. DeMille. Laser cooling of a diatomic molecule. *Nature*, 467(7317):820, 2010.

[31] E. Paperno, H. Koide, and I. Sasada. A new estimation of the axial shielding factors for multishell cylindrical shields. *Journal of Applied Physics*, 87(9):5959–5961, 2000.

[32] N.E. Bulleid, S.M. Skoff, R.J. Hendricks, B.E. Sauer, E.A. Hinds, and M.R. Tarbutt. Characterization of a cryogenic beam source for atoms and molecules. *Physical Chemistry Chemical Physics*, 15(29):12299–12307, 2013.

[33] J.F. Barry, E.S. Shuman, and D. DeMille. A bright, slow cryogenic molecular beam source for free radicals. *Physical Chemistry Chemical Physics*, 13(42):18936–18947, 2011.

[34] J.F. Barry. *Laser cooling and slowing of a diatomic molecule.* PhD thesis, Yale University, 2013.

[35] G.M. Davis, M.C. Gower, C. Fotakis, T. Efthimiopoulos, and P. Argyrakis. Spectroscopic studies of arf laser photoablation of pmma. *Applied Physics A*, 36(1):27–30, 1985.

[36] N.R. Hutzler, M.F. Parsons, Y.V. Gurevich, P.W. Hess, E. Petrik, B. Spaun, A.C. Vutha, D. DeMille, G. Gabrielse, and J.M. Doyle. A cryogenic beam of refractory, chemically reactive molecules with expansion cooling. *Physical chemistry chemical physics*, 13(42):18976–18985, 2011.

[37] H. Makaske. personal communication.

[38] S.Y.T. van de Meerakker, H.L. Bethlem, N. Vanhaecke, and G. Meijer. Manipulation and control of molecular beams. *Chemical reviews*, 112(9):4828–4878, 2012.

[39] G.P. Sutton and O. Biblarz. *Rocket propulsion elements.* John Wiley & Sons, 2016.

[40] M. Fournier, S.D. Le Picard, and I.R. Sims. Low-temperature chemistry in uniform supersonic flows. In *Cold Chemistry*, pages 1–45. The Royal Society of Chemistry, 2017.

[41] A. Canosa, A.J. Ocaña, M. Antinolo, B. Ballesteros, E. Jiménez, and J. Albaladejo. Design and testing of temperature tunable de laval nozzles for applications in gas-phase reaction kinetics. *Experiments in Fluids*, 57(9):152, 2016.

[42] D. Xiao, D.M. Lancaster, C.H. Allen, M.J. Taylor, T.A. Lancaster, G. Shaw, N.R. Hutzler, and J.D. Weinstein. Shaped nozzles for cryogenic buffer-gas beam sources. *Physical Review A*, 99(1):013603, 2019.

[43] K. Esajas. *forthcoming*. PhD thesis, Rijksuniversiteit Groningen, 2019.

[44] J.R. Meinema. *Obtaining Ultracold Molecules Through Stark Deceleration and Laser Cooling*. PhD thesis, Rijksuniversiteit Groningen, 2016.

[45] J. Nauta. *The use of optical cavities in cold molecule trapping, laser cooling and acetylene spectroscopy*. Rijksuniversiteit Groningen & University of Helsinki, 2014.

[46] V. Zhelyazkova. *Laser cooling of CaF molecules*. PhD thesis, Imperial College London, 2014.

[47] M. Rossa, C.A. Rinaldi, and J.C. Ferrero. Velocity distributions of ba and ba+ produced by 1064 nm pulsed laser ablation of barium in vacuum. *Journal of applied physics*, 100(6):063305, 2006.

[48] A. Miotello and R. Kelly. Laser-induced phase explosion: new physical problems when a condensed phase approaches the thermodynamic critical temperature. *Applied Physics A*, 69(1):S67–S73, 1999.

[49] N.M. Bulgakova and A.V. Bulgakov. Pulsed laser ablation of solids: transition from normal vaporization to phase explosion. *Applied Physics A*, 73(2):199–208, 2001.

[50] S. Truppe, M. Hambach, S.M. Skoff, N.E. Bulleid, J.S. Bumby, R.J. Hendricks, E.A. Hinds, B.E. Sauer, and M.R. Tarbutt. A buffer gas beam source for short, intense and slow molecular pulses. *Journal of Modern Optics*, 65(5-6):648–656, 2018.

[51] K.M. Chen, T.S. Chien, and C.C. Pei. Convolution of velocity distributions in a pulsed molecular beam. *Journal of the Chinese Chemical Society*, 36(2):131–134, 1989.

[52] B.R. Cameron and P.W. Harland. Deconvolution of unchopped time-of-flight waveforms. *Review of scientific instruments*, 65(1):108–115, 1994.

[53] Y. Yin. personal communication.

[54] A. Jadbabaie, N.H. Pilgram, J. Klos, S. Kotochigova, and N.R. Hutzler. Enhanced yield from a cryogenic buffer gas beam source via excited state chemistry. *arXiv preprint arXiv:1910.11331*, 2019.

[55] T. Ido, T.H. Loftus, M.M. Boyd, A.D. Ludlow, K.W. Holman, and J. Ye. Precision spectroscopy and density-dependent frequency shifts in ultracold sr. *Physical review letters*, 94(15):153001, 2005.

[56] U. Dammalapati. *Metastable D-state spectroscopy and laser cooling of barium.* PhD thesis, Rijksuniversiteit Groningen, 2006.